Quantum size effect in topological heterojunctions

Yuya ASAKA

University of Electro-Communications
Department of Engineering Science

A Dissertation submitted for
Doctor of Philosophy in Science

March 2023

Quantum size effect in topological heterojunctions

Advisor: Associate Professor Yuki Fuseya

Secondary Advisor: Professor Naruo Sasaki

Supervisory committee:

Associate Professor Yuki Fuseya

Professor Naruo Sasaki

Professor Jun Nakamura

Associate Professor Kazuyuki Matsubayashi

Associate Professor Nobuhito Kokubo

概要

ヘテロ接合はバンド構造を制御する有効な方法の一つである．例えば，太陽電池，レーザー，トランジスタはヘテロ接合によるバンドエンジニアリングの成功例である． 2 つの異種半導体のバンド端を繋ぐことで表現されるバンド接続は非常に有名で，ヘテロ接合を扱う多くの教科書で言及されている．1980 年代半ばには，$Pb_{1-x}Sn_xTe$ や $Hg_{1-x}Cd_xTe$ などの互いにバンド反転した半導体のヘテロ接合のギャップ中に，界面状態が存在する可能性が提唱された．近年，この界面状態はトポロジーの観点から再検討されている．トポロジカル絶縁体はバンド反転していることから，結晶内部が絶縁体であり，表面は金属的な伝導状態を持つという特徴がある．トポロジカル絶縁体と自明な絶縁体の接合においては，界面で同じ対称性を持つバンドを接続するため，界面にギャップレス伝導状態が存在すると考えられている．

本研究における研究対象は V 族物質のビスマス (Bi)，およびビスマスアンチモン (BiSb) のヘテロ接合系である．半金属である Bi は非常に多彩な性質を持ち，精力的に研究が行われている物質である．Bi が持つ特徴の一つは巨大なスピン軌道相互作用を持つことである．巨大なスピン軌道相互作用は，バンド反転を生じる原因であり，BiSb 系の特徴的な表面状態を作っている．Bi は Liu-Allen 模型を用いた計算に基づけば，自明なトポロジーを持っている．Fu と Kane は 2007 年に BiSb が三次元トポロジカル絶縁体であると提案した．Liu-Allen 模型では，$Bi_{1-x}Sb_x$ のトポロジーは Sb 含有量 (x) の増加に伴って，$x = 0.02$ を境に自明から非自明に切り替わる．しかし，純 Bi($x = 0.00$) がトポロジカル絶縁体であると示唆する報告もある．純 Bi のトポロジーに対するこの対立は，Fu らによって提案された BiSb のトポロジーの決定方法に起因している．表面フェルミ面を数えることによってトポロジーを決定する Fu ら方法は簡便である．しかし，BiSb 系のバンドギャップは極めて小さく，測定は困難である．加えて，量子サイズ効果が表面の電子に大きな大きな影響を与えることは広く知られている．有限厚さのトポロジカル絶縁体薄膜では，量子サイズ効果によって，トポロジカルに保護された表面状態にギャップが開く．この表面状態の質的な変化も，BiSb 系のトポロジーの決定を困難にしている．このような量子サイズ効果は物質のフェルミ波長が長ければ顕著に現れる．しかし，トポロジーの異なる二つの物質からなる“トポロジカル”ヘテロ接合において，量子サイズ効果がバンド接続にどのような影響を及ぼすかはあまり調査されていない．BiSb のフェルミ波長は非常に長く，100nm 程度の膜厚があっても表裏の両表面が互いに干渉する．Bi_2Se_3 などのトポロジカル物質の表面波動関数の浸透長は数 nm のオーダーであることを踏まえると，BiSb における長距離波長が稀であることがわかる．BiSb 系は波動関数の浸透長が長く，量子サイズ効果を確認できる領域が大きい．従って，Bi/BiSb ヘテロ接合系は，トポロジカルヘテロ接合における量子サイズ効果の影響の調査に適している．

本研究では，Liu-Allen 模型に基づいて，有限膜厚における Bi(111)/BiSb(111) ヘテロ接合の計算を行なった．計算の結果，Bi/BiSb ヘテロ接合のバンド接続は，これまで知られていたどのバンド接続にも属さない新しいタイプであることを発見した．さらに，Bi 表面で得られる二つの表面状態のスペクトルのうち一つは、Bi 本来の表面状態ではないことを理論的に明らかにした．これは，厚さ 80nm ほどの膜厚を持つヘテロ接合でも起こり，波動関数が貼り合わせた材料を通して互いに浸透し合うことを示している．Bi/BiSb ヘテロ接合系の強い量子サイズ効果に起因したこの偽物の表面状態は，接合物質 (BiSb) のバルク波動関数が Bi 表面まで浸透して，表面状態として振る舞っている．

University of Electro-Communications

Doctoral Thesis

Quantum size effect in topological heterojunctions

Yuya Asaka

A thesis submitted in fulfillment of the requirements
for the degree of Doctor of Philosophy

in the

Theoretical Condensed Matter Physics Laboratry
Department of Engineering Science

UNIVERSITY OF ELECTRO-COMMUNICATIONS

Abstract

Faculty Name
Department of Engineering Science

Doctor of Philosophy

Quantum size effect in topological heterojunctions

by Yuya Asaka

Heterojunctions are an effective way to control band structure. For example, solar cells, lasers, and transistors are successful examples of band engineering by heterojunction. Band alignment, represented by connecting the band of two dissimilar semiconductors, is mentioned in many textbooks dealing with heterojunctions. In the mid-1980s, the possibility of interface state in heterojunctions with inverted bands was proposed. Recently, this interface state has been reexamined from the viewpoint of topology. In order to connect bands of the same symmetry at the junction interface between a topological insulator and an ordinary insulator, a gapless conduction state must exist at the interface.

Quantum size effects are prominent when the Fermi wavelength of the material is long. The penetration length of the surface wavefunction of topological materials, e.g. Bi2Se3, is a few nm. In the Bi_2Se_3 system, it is difficult to study the effect of quantum size effects on topological heterojunctions because the region in which quantum size effects can be observed is extremely small. On the other hand, in the BiSb system, the Fermi wavelength is so long that the top and bottom surfaces interfere with each other even with a film thickness of about 100 nm. Therefore, the region where the quantum size effect can be observed is large. The Bi/BiSb heterojunction system is suitable for investigating the effects of quantum size effects on topological heterojunctions.

In this work, we investigated the Bi/BiSb topological heterojunction, where a strong quantum size effect is expected because of the very long penetration length of the surface state. As a result, we found a band alignment that is neither expected for ordinary heterojunctions nor topological heterojunctions. In addition, numerical results surprisingly confirmed the appearance of a “superficial surface state” on the Bi surface due to the influence of the substrate (BiSb).

Contents

List of Figures

List of Tables

Chapter 1

introduction

Heterojunctions, junctions of two different materials, have a wide range of applications because of the effective control of carriers. Some well-known applications are solar cells, lasers, and HEMTs. Today, many textbooks[1–3] featured the concept of heterojunctions. The band alignment of heterojunctions (Fig. 1.1 (a)) is familiar to anyone with a background in engineering. In this band alignment, the conduction bands or valence bands smoothly connect at the junction interface of the two bulk semiconductors. This band alignment was inferred from bulk picture. In a topological heterojunction system, a gapless state at the interface is often recognized in Fig. 1.1 (b), but it is not a strict picture because the interface is a finite system concept.

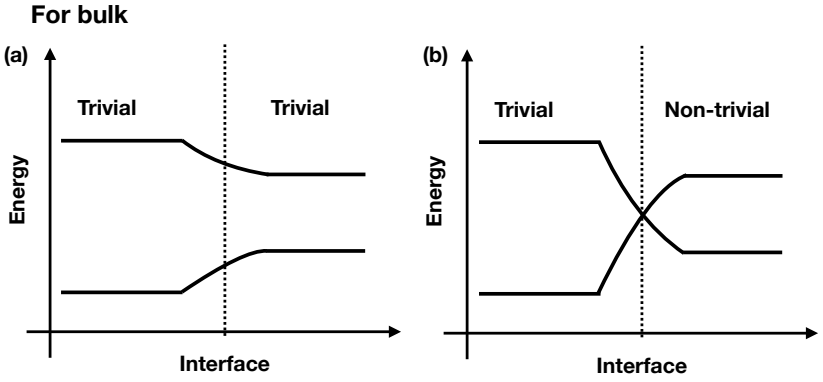

FIGURE 1.1
Band alignment of heterojunction systems inferred from the bulk picture. (a) trivial heterojunction. (b) topological heterojunction.

The history of topological heterojunction began around 1980, before the discovery of Z_2 topological insulators and topological crystalline insulators. For example, $Pb_{1-x}Sn_xTe$[4, 5] and $Hg_{1-x}Cd_xTe$[6–9] systems, these heterojunction systems have unique properties. From a modern viewpoint, they can be considered topological heterojunctions.

A "topological heterojunction" is a junction between a topologically non-trivial material and trivial material. In the calculation of this junction system, we must consider finite systems. There are the interface state between two materials and the surface state of each material in a heterojunction system. Several papers have shown that the topologically protected surface states are affected by quantum size effects and that the surface and interface states have energy gap[10–12]. The study of quantum size effects in topological heterojunction systems has been intensifying in recent years. A topological proximity effect is a typical example of topological heterojunction[13, 14]. An interesting result is the appearance of a topological surface state in a Bi ultra-thin-film under the influence of the substrate[14]. However, the effect of quantum

size effects in topological heterojunction systems is still unknown. The number of eigenvalues in a finite-size system increases with the number of layers. Therefore, many states connecting different materials' eigenvalues are expected to exist at the heterojunction interface (Fig. 1.2 (a)). We can expect many gapless states at the interface of topological heterojunctions, which is a prediction in Fig. 1.2 (b). The surface state is the interface between a topological insulator and the vacuum. By analogy with the surface state, the gapless state at the interface of a trivial/non-trivial heterojunction has a gap and the band alignment in Fig. 1.2 (c) is also expected. However, our results reject the expected picture of a topological interface state(Fig. 1.2 (b,c)). This rejection is a surprising result because the expected picture is so widely accepted as a topological interface that many textbooks mentioned it. We will discuss this interface state in chapter .

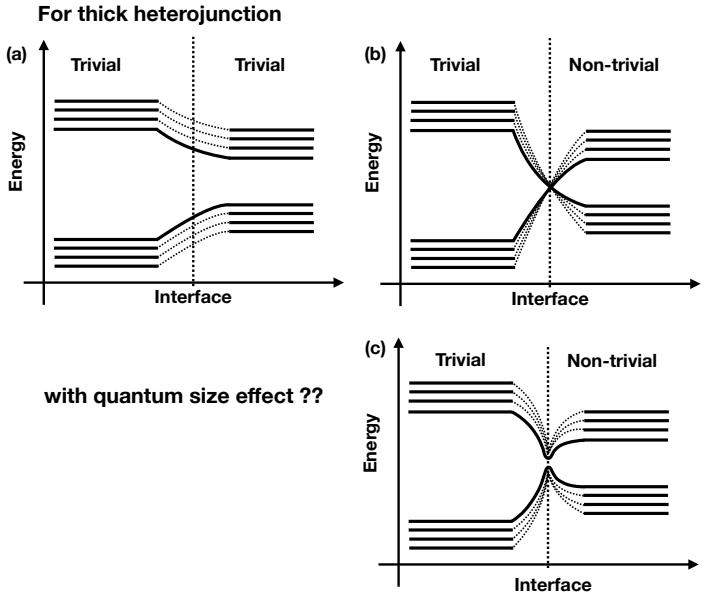

FIGURE 1.2
Band alignment of heterojunctions in finite thickness systems: (a) for the trivial heterojunction, (b) for the expected picture of a topological heterojunction, and (c) for the expected picture of a topological heterojunction with the quantum size effect.

In addition, there is an idea of band engineering using topological trivial/non-trivial hetero-multilayer structures. For example, Burkov et al. theoretically predicted that an intermediate phase between an ordinary insulator and a three-dimensional quantum anomalous Hall insulator could be realized by alternating layers of a magnetized topological insulator and an ordinary insulator[15, 16]. This prediction suggests that heterojunction changes the Chern number, one of the topological invariants. What about the Z_2 topological invariant? Heterojunctions do not affect the Z_2 topological invariants defined from the bulk of the material. However, we can define a bulk by taking topologically trivial/non-trivial heterojunction as a unit cell with boundary conditions as in the method of Burkov et al. Thus, investigating the "Z_2 topology of heterojunction systems" made from both junction materials is an exciting topic.

As a topological heterojunction system, a material of particular interest is BiSb, which was first introduced as a three-dimensional topological insulator by Fu and Kane[17, 18]. BiSb is known to have three-dimensional Dirac electrons in its bulk[19], and not only is its band dispersion highly linear, but also its effective mass is extremely

small compared to free electrons. Therefore, BiSb has a wave function with a very long penetration length. Moreover, the long-range penetration of the wave function intensifies the quantum size effect; in the BiSb system, the surface-to-surface interference effect is observed even at film thicknesses of 100 nm or more[12]. $Bi_{1-x}Sb_x$ is topologically trivial for $x < 0.02$ and a topologically non-trivial insulator for $x > 0.02$, according to numerical calculations using the Liu-Allen model[20]. This junction system can switch from topologically trivial to non-trivial at a single value of Sb content x. Therefore, the $Bi/Bi_{1-x}Sb_x$ junction system is a good research topic that can be viewed continuously from a trivial/trivial junction system to a trivial/non-trivial junction system.

In this work, we calculated the Bi (111)/BiSb(111) heterojunction system with a finite thickness based on the tight-binding model by Liu and Allen[20, 21]. As a result, we found a band alignment that is neither expected for ordinary heterojunctions nor topological heterojunctions. In addition, numerical results surprisingly confirmed the appearance of a "superficial surface state" on the Bi surface due to the influence of the substrate (BiSb).

Chapter 2

Topological heterojunction

2.1 Heterojunction

A heterojunction is a system of two different materials joined together[1–3]. A heterojunction is two different materials joined together. Generally, an ideal junction is possible if the conditions for the formation of the junction between the materials match. To achieve this[1], both materials must have the same crystal structure and lattice constants.

Shockley, the inventor of the transistor, first proposed the idea of heterojunction. Shockley published his p-n junction theory and junction transistor and proposed the hetero-bipolar transistor in the 1940s and 1950s[22, 23]. The technology to make a junction of two semiconductors was not available then. In 1959, when epitaxial vapor deposition technology was developed at IBM in the United States, it became possible actually to form a heterojunction. Anderson, who was at IBM then, formed the first GaAs-Ge heterojunction and analyzed the heterojunction's energy band structure and current transport mechanism using the same treatment as Shockley's p-n junction theory[24]. Subsequently, devices utilizing heterojunctions, such as solar cells[25], were proposed.

Band engineering using heterojunctions has a wide variety of applications. One of the most famous is the tunnel diode[26]. The engineering significance of joining two materials with different band gaps is the control of electrons and holes. Heterojunctions allow us to control electrons and holes by forming unique band alignments. Such band engineering has contributed to engineering developments. Layered structures are components for the design of complicated devices.

Compound crystals are commonly used in heterojunctions (we used $Bi_{1-x}Sb_x$, PbTe, and SnTe in this doctoral thesis). Parameters such as lattice constants are obtained by linear extrapolation of the values of the two atoms. This approximation follows Vegard's law[27, 28]. For example, in the case of lattice constants, $a_{\mathrm{BiSb}} = a_{\mathrm{Bi}}(1-x) + a_{\mathrm{Sb}}x$. Changes in the lattice constants of compound crystals are tiny, and Bi/BiSb heterojunctions are not expected to cause significant distortions even in multilayer structures. The situation is similar for III-V and IV-VI group semiconductors.

[1] When forming a non-ideal heterojunction, such as a junction with a substrate material, it is not necessary to meet this condition.

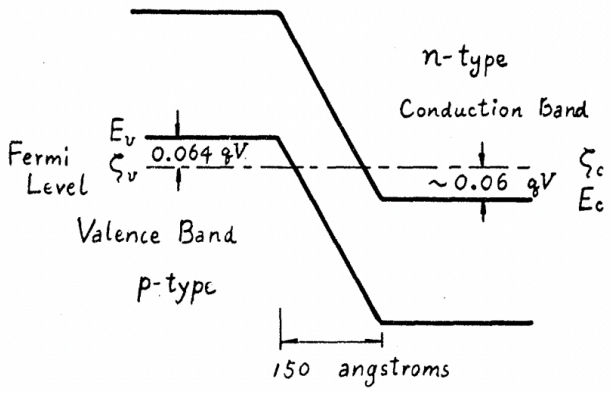

FIGURE 2.1
Energy diagram of the *p*-*n* junction. [Taken from Ref.[26] L. Esaki, Phys. Rev (1957).]

2.1.1 Tunnel barrier and quantum well

The tunneling barrier is a fundamental topic in quantum mechanics textbooks. In classical theory, if an electron does not have enough energy to pass over a potential barrier, it cannot pass the barrier. In quantum mechanics, however, low-energy electrons also tunnel through the barrier[26, 29]. In the GaAs/AlGaAs/GaAs heterojunction system, the tunneling barrier is realized[30, 31]. The tunneling barriers have a wide range of applications, such as selectively controlling the injection of electrons. Heterojunctions enable not only the formation of energy barriers but also quantum wells. Specifically, superlattice structures can be constructed by stacking GaAs/AlGaAs systems[32].

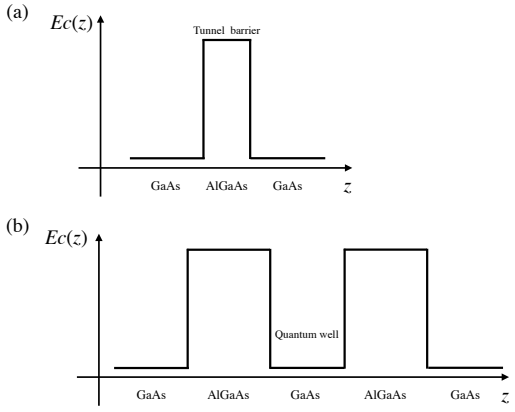

FIGURE 2.2
Energy diagram of E_c in GaAs/AlGaAs systems. (a),Tunnel barrier and (b), Quantum well

2.2 Quantum size effect

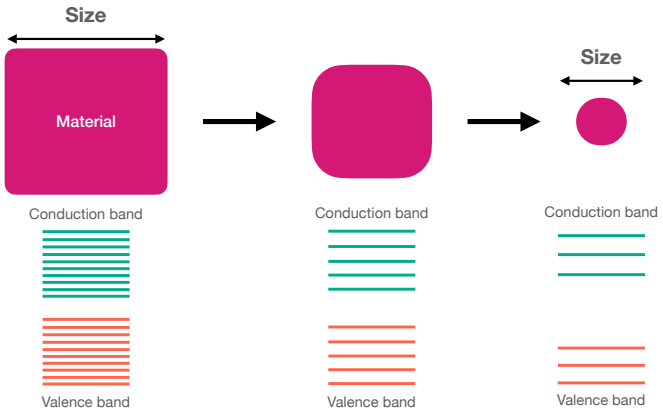

FIGURE 2.3
Conceptual diagram of the quantum size effect.

This section is not directly related to topological heterojunctions. However, it is an essential component when considering finite systems. Therefore, we briefly introduce quantum size effects.

Electrons in metals or semiconductors are usually considered to be continuously distributed in bulk. However, when a material is reduced to a size equivalent to the de Broglie wavelength of an atom (a few nm), the electrons are confined, and the electron density of states becomes discrete. The effect of the electrons having discrete energy levels leads to properties not seen in bulk semiconductors. This effect is called the quantum size effect.

2.3 Topological insulator

Materials are classified into two categories: metals and insulators. Topological insulators, on the other hand, are materials whose bulk is an insulator and whose edges are metal (In a three-dimensional system, the edges are surfaces)[17, 33–37]. Topological insulators are defined by the Z_2-topological invariant ν in solids. In trivial insulators, $\nu = 0$, and in topological (non-trivial) insulators, $\nu = 1$. Thus, insulators are classified by the Z_2 index, which is a topological invariant. In order to realize a topological insulator, band inversion due to strong spin-orbit interaction is necessary. In other words, the parity of the wavefunction in the valence band is flipped positive or negative. It is generally accepted that a connection between a trivial insulator and a non-trivial insulator must once pass through a metallic state at the interface[4, 38].

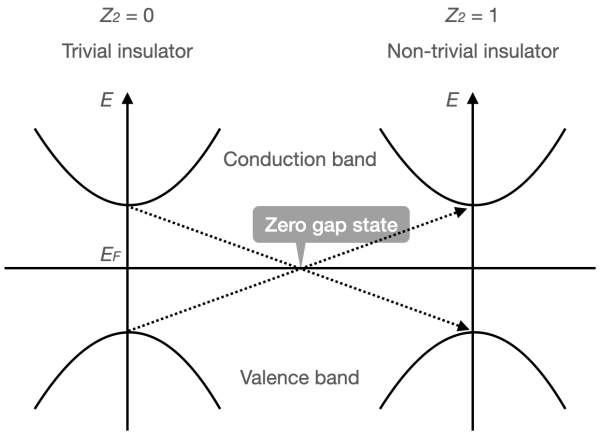

FIGURE 2.4
Situation in which a trivial insulator and a non-trivial insulator are connected.

The metallic state at the interface realizes a zero-gap state where the valence band and the conduction band cross at a single point (Fig. 2.4). The vacuum is a trivial insulator with an infinite band gap. We can understand why a metallic state is realized at the surface or edge of a topological insulator connected to the vacuum. The realization of this metallic state depends only on the topological properties of the bulk. Therefore, it is called bulk-edge correspondence[39, 40].

2.3.1 Time-reversal symmetry

Time-reversal symmetry plays an important role in topological insulators. The time-reversal operation reverses time t to $-t$. Under the system spin 1/2, the relational equations for the wavefunction are

$$\Theta\psi = i\sigma_y\psi^* \tag{2.1}$$

and

$$\Theta\psi_\uparrow = \psi^*_\downarrow, \tag{2.2}$$

$$\Theta\psi_\downarrow = -\psi^*_\uparrow, \tag{2.3}$$

where Θ is the time reversal operator and the wavefunction is $\psi = [\psi_\uparrow; \psi_\downarrow]$. When the Hamiltonian is invariant in time reversal, $[\hat{H}, \Theta] = 0$, so $\Theta\hat{H}\Theta^{-1}$. Therefore,

$$\Theta\hat{H}_{\boldsymbol{k}}\Theta^{-1} = H_{-\boldsymbol{k}}. \tag{2.4}$$

We consider how the eigenstates correspond in such a system with time-reversal symmetry. From the Bloch wavefunction $u_{n\boldsymbol{k}}$ and the Hamiltonian in equation 2.4, the

eigen equation is described by

$$H_{\boldsymbol{k}} u_{n\boldsymbol{k}} = E_{n\boldsymbol{k}} u_{n\boldsymbol{k}}. \tag{2.5}$$

Using equation 2.5, we obtain

$$\Theta H_{\boldsymbol{k}} \Theta^{-1} \Theta u_{n\boldsymbol{k}} = E_{n\boldsymbol{k}} \Theta u_{n\boldsymbol{k}}, \tag{2.6}$$

and

$$H_{-\boldsymbol{k}}(\Theta u_{n\boldsymbol{k}}) = E_{n\boldsymbol{k}}(\Theta u_{n\boldsymbol{k}}). \tag{2.7}$$

Thus, the energy bands are invariant to the operation $\boldsymbol{k} \leftrightarrow -\boldsymbol{k}$. We now turn our attention to special wavenumbers invariant to time reversal. It is the Time Reversal Invariant Momenta (TRIM). TRIM is defined in $\boldsymbol{k} \equiv -\boldsymbol{k}$. The difference between $\boldsymbol{k}$ and $-\boldsymbol{k}$ equals the reciprocal lattice vector. There are eight TRIMs inside the Brillouin zone for a three-dimensional topological insulator. The wavenumber of TRIM is $\boldsymbol{k} = n_1\boldsymbol{b}_1 + n_2\boldsymbol{b}_2 + n_3\boldsymbol{b}_3$. $(\boldsymbol{b}_1, \boldsymbol{b}_2, \boldsymbol{b}_3)$ is a reciprocal lattice vector, and $n_{1,2,3} = 0$ or 1.

2.3.2 Space inversion symmetry

We consider the case when the system has space inversion symmetry. P is the space inversion operator. The wavenumber $\boldsymbol{k}$ flipped to $-\boldsymbol{k}$ for the space inversion. Therefore, $PH_{\boldsymbol{k}}P^{-1} = H_{-\boldsymbol{k}}$. Both time and space inversion invert the sign of the wavenumber $\boldsymbol{k}$. If the time-reversal and space-reversal operations are performed consecutively, the wavenumber returns to the original value as

$$(P\Theta)\hat{H}_{\boldsymbol{k}}(P\Theta)^{-1} = H_{\boldsymbol{k}}. \tag{2.8}$$

Thus, the Eigen equation leads to

$$H_{\boldsymbol{k}}(P\theta u_{n\boldsymbol{k}}) = E_{n\boldsymbol{k}}(P\theta u_{n\boldsymbol{k}}). \tag{2.9}$$

The wavenumber $\boldsymbol{k}$ is arbitrary. Space inversion keeps the spin invariant. On the other hand, time reversal flips the spin. Therefore, $P\theta u_{n\boldsymbol{k}}$ and $u_{n\boldsymbol{k}}$ are orthogonal. In the system having time-reversal and space-reversal symmetries, the state is degenerate at arbitrarily Bloch wavenumbers.

2.3.3 Z_2 topological number

The trivial insulators and the non-trivial insulators (topological insulators) are classified by Z_2 topological number. The topological number can be calculated from the bulk electronic structure. For two-dimensional topological insulators, the classification is simply $\nu = 0$ or 1. The band structures of the non-trivial and trivial insulators are indistinguishable because they both have a band gap. Thus, from the information in the wavefunction of a material, its topological properties are determined.

In this section, we first discuss topological numbers for two-dimensional systems. We consider $2N$ bands with energies below the Fermi energy (N is an integer). The Bloch wavefunctions of these bands are defined as $|u_{n,\boldsymbol{k}}\rangle$ and the $2N \times 2N$ matrix $\omega_{mn}(\boldsymbol{k})$ is defined as

$$\omega_{mn}(\boldsymbol{k}) = \langle u_{m,-\boldsymbol{k}}|\Theta|u_{n,\boldsymbol{k}}\rangle, \tag{2.10}$$

where $m, n = 1, ..., 2N$. Using $\omega(\boldsymbol{k})$ and the topological number ν, the exponent is expressed as

$$(-1)^{\nu} = \prod_{i}^{4} \frac{\mathrm{Pf}(\omega(\boldsymbol{\Gamma}_i))}{\sqrt{\det(\omega(\boldsymbol{\Gamma}_i))}}, \tag{2.11}$$

where the wavenumber $\boldsymbol{k} = \boldsymbol{\Gamma}_i$ in TRIM. Equation 2.11 does not consider space inversion symmetry. If space inversion symmetry is considered, a simpler notation is possible. In the case of space inversion symmetry, each TRIM is invariant to space inversion operations. The wave function in a TRIM satisfies

$$Pu_{\boldsymbol{k}}(\boldsymbol{r}) = u_{\boldsymbol{k}}(-\boldsymbol{r}) = \pm u_{\boldsymbol{k}}(\boldsymbol{r}). \tag{2.12}$$

The space inversion operator P can be simultaneously diagonalization with the Hamiltonian. From $P^2 = 1$, the parity eigenvalues are $+1$ or -1. The bands from the lowest energy band to the Fermi energy are numbered in order as $m = 1, 2, 3, ..., 2n$. The parity eigenvalue in TRIM of the mth band is denoted as $\xi_m(\boldsymbol{\Gamma}_i)$. The $(2m-1)$th and $(2m)$th bands are Kramers degenerate and have the same parity. Only the $(2m)$th band should be counted to avoid duplication of Kramers pairs. Here, the product of parity eigenvalues from all Kramers pairs below the Fermi energy is obtained in one TRIM as

$$\delta_i = \prod_{m=1}^{N} \xi_{2m}(\boldsymbol{\Gamma}_i). \tag{2.13}$$

From the product of parities in the equation 2.13 obtained for all TRIMs, the topological number ν is expressed as

$$(-1)^{\nu} = \prod_{i}^{4} \delta_i. \tag{2.14}$$

This equation takes the value ± 1. Therefore, $\nu = 0$ or 1. For example, we assume a system in which the parity of the valence band is $+1$ in all TRIMs. When band inversion occurs in a TRIM with a conduction band parity of -1 by changing an external parameter, the valence band parity in that TRIM is inverted. Thus, the parity of the bands below the Fermi energy is inverted, and the Z_2 topological number changes.

2.3.4 Three-dimensional topological insulator

A three-dimensional topological insulator [17, 36] has eight TRIMs. The exponents at each TRIM are expressed as

$$\delta_i = \prod_{m=1}^{N} \xi_{2m}(\mathbf{\Gamma}_i) \tag{2.15}$$

In the three-dimensional topological insulator, four Z_2 topological numbers are defined as $\nu_0, \nu_1, \nu_2, \nu_3$. Each topological number takes the value 0 or 1 and is defined as

$$(-1)^{\nu_0} = \prod_{i=1}^{8} \delta_i, \tag{2.16}$$

and

$$(-1)^{\nu_j} = \prod_{i=(n_1 n_2 n_3), n_j=1} \delta_i. \tag{2.17}$$

The ν_0 is defined from the product of all TRIM parities. The $\nu_j (j = 1, 2, 3)$ is defined from the product of the parities of the four TRIMs on the surface $\boldsymbol{k} = \frac{1}{2}(n_1\boldsymbol{G}_1 + n_2\boldsymbol{G}_2 + n_3\boldsymbol{G}_3)$ in the reciprocal lattice space. These are collectively denoted as $\nu_0; (\nu_1\nu_2\nu_3)$. The four topological numbers define 16 different phases.

The information on the Z_2 topological number allows us to determine the number of Fermi surfaces on the two-dimensional projected Brillouin zone. The eight TRIMs in the bulk Brillouin zone are projected as the four surface TRIMs. In the surface TRIMs, we take the product of two δ_i exponents of the projected bulk TRIMs. The exponent δ_i of the surface TRIMs is ± 1. If δ_i is the same (different) between the surface TRIMs, we have an even (odd) number of Fermi surfaces.

From the above, when $\nu_0 = 1$, a surface state exists on the surface in all directions. On the other hand, when $\nu_0 = 0$, there is no Fermi surface in a particular direction, and the surface state has a band gap. The system with $\nu_0 = 1$ ($\nu_0 = 0$) is called a strong (weak) topological insulator. The system with $\nu_0 = \nu_{1,2,3} = 0$ is a normal insulator. Weak topological insulators are understood as stacked two-dimensional topological insulators. On the other hand, strong topological insulators have an important three-dimensionality.

2.4 Surface state of topological insulator

The surface of a topological insulator has a metallic conduction state. The vacuum is a topologically trivial insulator with an infinite band gap. Thus, a gapless state is realized at the topological insulator and vacuum interface. This surface state is responsible for conducting a pure spin current in which the different spins up and down move in opposite directions. The topological insulator introduced in the previous section is an ordinary insulator with no spin-orbit interaction. In other words, topological insulators have strong spin-orbit interaction. Because space inversion symmetry breaks at the material's surface, the surface state is spin-split due to spin-orbit interaction. The typical band dispersion that appears on the surface of a topological insulator is a cone-like band dispersion called a Dirac cone. In this Dirac cone dispersion, the electron spins and velocities are perpendicular to each other. For example, when

spins with a fixed orientation are injected, the injected spins run in a fixed direction, and a voltage is generated in a specific direction[41–44].

2.4.1 Dirac equation

The Dirac equation describes the surface state of a three-dimensional topological insulator. Furthermore, it is an equation based on relativistic quantum mechanics describing elementary particles with spin-1/2, written by P.A.M Dirac in 1928[45]. The Hamiltonian is described by

$$H = c\boldsymbol{p}^2 \cdot \boldsymbol{\alpha} + mc^2\boldsymbol{\beta}. \tag{2.18}$$

where c is the speed of light and m is the rest mass. The Dirac matrices α_i and β satisfy the relations $\alpha_i^2 = \beta^2 = 1$, $\alpha_i\alpha_j = -\alpha_j\alpha_i$ and $\alpha_i\beta = -\beta\alpha_i$. In three-dimensions, the Dirac matrix[2] is written using the Pauli matrix σ_i as

$$\alpha_x = \sigma_x \otimes \sigma_i, \beta = \sigma_z \otimes \sigma_0. \tag{2.21}$$

The Dirac equation is written as

$$\left[c\boldsymbol{p}^2 \cdot \alpha + mc^2\beta\right]\psi = E\psi. \tag{2.22}$$

Based on this equation, the relativistic energy-momentum relation is the solution of the following equation

$$E^2 = m^2c^4 + p^2c^2. \tag{2.23}$$

In order to describe topological insulators using the Dirac equation [10], we use the second-order correction $-Bp^2$ of the momentum p to the band gap or rest mass term. The Dirac Hamiltonian is described as

$$H = v\boldsymbol{p} \cdot \boldsymbol{\alpha} + \left(mv^2 - B\boldsymbol{p}^2\right)\boldsymbol{\beta}, \tag{2.24}$$

where v is velocity and m is mass. Also, mv^2 is the bandgap.

2.4.2 Surface state

We consider the $x-y$ plane at $z = 0$ in the three-dimensions. From Equation 2.21, the surface Hamiltonian is described by

$$\Delta H_{3D} = v\left(p_x\boldsymbol{\alpha}_x + p_y\boldsymbol{\alpha}_y\right) - B\left(p_x^2 + p_y^2\right)\boldsymbol{\beta}. \tag{2.25}$$

[2]For one-dimension, the Dirac matrix is described by

$$\boldsymbol{\alpha}_x = \sigma_x, \boldsymbol{\beta} = \sigma_z. \tag{2.19}$$

For two-dimensions,

$$\boldsymbol{\alpha}_x = \sigma_x, \boldsymbol{\alpha}_y = \sigma_y, \boldsymbol{\beta} = \sigma_z. \tag{2.20}$$

The two solutions described below are the basis.

$$\Psi_1 = \frac{C}{\sqrt{2}} \begin{pmatrix} \mathrm{sgn}(B) \\ 0 \\ 0 \\ i \end{pmatrix} \left(e^{-z/\xi_+} - e^{-z/\xi_-} \right) e^{\frac{i}{\hbar}(p_x x + p_y y)} \tag{2.26}$$

and

$$\Psi_2 = \frac{C}{\sqrt{2}} \begin{pmatrix} 0 \\ \mathrm{sgn}(B) \\ i \\ 0 \end{pmatrix} \left(e^{-z/\xi_+} - e^{-z/\xi_-} \right) e^{\frac{i}{\hbar}(p_x x + p_y y)}, \tag{2.27}$$

where C is the normalization constant and $\xi_\pm$ is the penetration length. Using Equations 2.26 and 2.27, the effective Hamiltonian is written as

$$H_{eff} = \left(\langle \Psi_1 |, \langle \Psi_2 | \right) \Delta H_{3D} \begin{pmatrix} |\Psi_1\rangle \\ |\Psi_2\rangle \end{pmatrix}. \tag{2.28}$$

With a unitary transformation[3] to the equation, the effective Hamiltonian can be rewritten as

$$H_{eff} = \left(\langle \Phi_1 |, \langle \Phi_2 | \right) \Delta H_{3D} \begin{pmatrix} |\Phi_1\rangle \\ |\Phi_2\rangle \end{pmatrix} = v\mathrm{sgn}(B) \left(p_x \sigma_x + p_y \sigma_y \right). \tag{2.31}$$

Thus, the band dispersion becomes $E = v\sqrt{p_x^2 + p_y^2}$. For three-dimensions, using $\Psi_\pm^0$[4], the exact solution of the surface state with boundary is described by

$$\Psi_\pm = C\Psi_\pm^0 \left(e^{-z/\xi_+} - e^{-z/\xi_-} \right) e^{\frac{i}{\hbar}(p_x x + p_y y)}, \tag{2.34}$$

where the penetration length dependent on p is

$$\xi_\pm = \frac{2|B|\hbar}{v} \left(1 \pm \sqrt{1 - 4mB + 4B^2 p^2/\hbar^2} \right)^{-1}. \tag{2.35}$$

[3] A unitary transformation,

$$\Phi_1 = \frac{1}{\sqrt{2}} \left(\Psi_1 - i\Psi_2 \right) \tag{2.29}$$

$$\Phi_2 = \frac{1}{\sqrt{2}} \left(\Psi_1 + i\Psi_2 \right) \tag{2.30}$$

[4] $\Psi_\pm^0$ is described by

$$\Psi_+^0 = \begin{pmatrix} \cos(\theta/2)\mathrm{sgn}(B) \\ -i\sin(\theta/2)\mathrm{sgn}(B) \\ \sin(\theta/2) \\ i\cos(\theta/2) \end{pmatrix}, \tag{2.32}$$

$$\Psi_-^0 = \begin{pmatrix} \sin(\theta/2)\mathrm{sgn}(B) \\ i\cos(\theta/2)\mathrm{sgn}(B) \\ -\cos(\theta/2) \\ i\sin(\theta/2) \end{pmatrix}, \tag{2.33}$$

where $\tan\theta = p_x/p_y$.

The band dispersion is $E = v\sqrt{p_x^2 + p_y^2}\mathrm{sgn}(B)$.

2.4.3 Topological surface state

Using the Dirac equation introduced in the previous section, Shan et al.[46] derived the effective Hamiltonian for the surface state of a three-dimensional topological insulator as follows

$$H_{eff} = \epsilon_0(p) + v_{eff}\left(p \times \sigma\right)_z, \tag{2.36}$$

where $\epsilon_0(p) = E_0 + D_{\|}\left(p_x^2 + p_y^2\right)$ and $v_{eff} = \mathrm{sgn}(B_\perp)\sqrt{1 - D_\perp^2/B_\perp^2}\,v_\perp$.

For finite film thicknesses, this topological surface state is known to have a gap due to the quantum size effect [11]. Topological surface states have a finite penetration length, which decreases exponentially into the crystal. When the film is thinner than the penetration length of the wavefunction, the top and bottom surface states interfere with each other.In this case, a gap opens due to the mutual interference between the surface states. The strength of the interference between the surface states affects the gap opening. In other words, as shown in Fig. 2.5 (a), the thinner film thickness, the more significant the gap. This gap opening has been verified both theoretically and experimentally[12, 47–49].

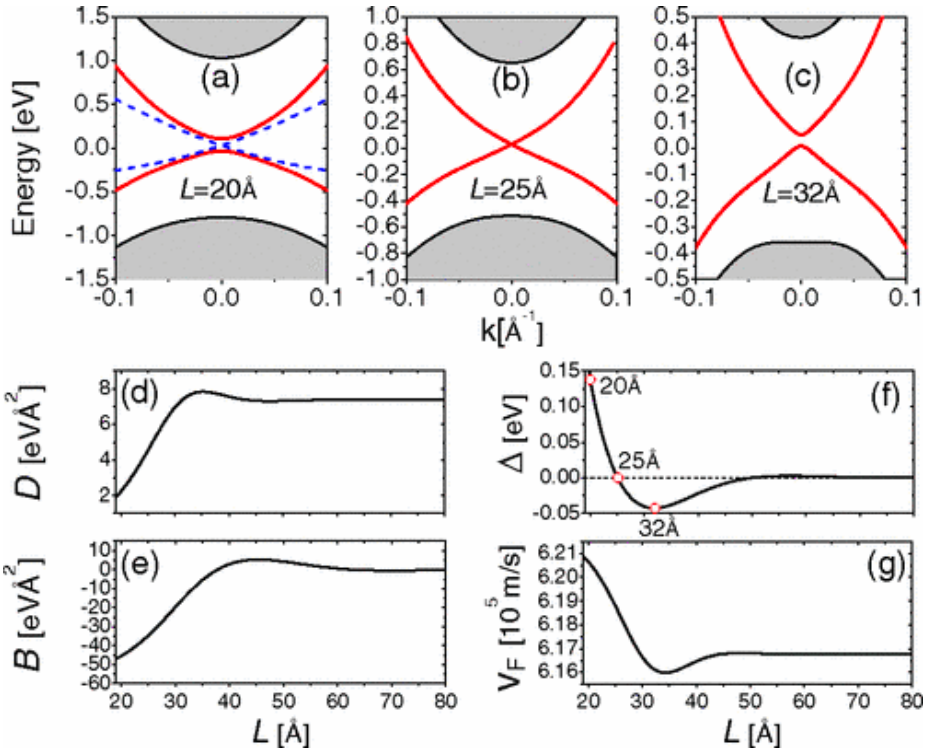

FIGURE 2.5
(a-c) Energy spectra of surface states for thicknesses $L = 20, 25, 32$Å(solid lines), respectively, and $L = \infty$ (dash lines). (d–g) The calculated parameters for the new effective model H_{eff} as a function of thickness L. [Taken from Ref. [48] H-Z Lu, W-Y Shan, W Yao, et al., Phys. Rev. B(2010).]

2.5 Topological heterojunctions

In the mid-1980s, it was proposed that an interface state exists in the gap at heterojunctions between semiconductors with band inversion, e.g., $Pb_{1-x}Sn_xTe$[4, 5] and $Hg_{1-x}Cd_xTe$[6–9]. Recently, this interface state has been reexamined from the viewpoint of topology. In the case of a topologically non-trivial insulator in contact with a trivial insulator, a gapless conduction state must exist at the interface to connect energy bands with the same symmetry[50]. Heterojunction systems of topological insulators are the target of various research in progress[51, 52], such as carrier control.

2.5.1 $Hg_{1-x}Cd_xTe$ systems

CdTe/HgTe/CdTe quantum wells have been the most actively studied experimentally as topological insulators. CdTe is a cubic crystal structure semiconductor and a trivial insulator. On the other hand, in HgTe, the strong spin-orbit interaction inverted the symmetry of the bulk valence band and conduction band. However, due to the cubic symmetry of HgTe crystal, the gap is closed at $\boldsymbol{k} = 0$. In order to make it a topological insulator, it must be made a bulk insulator via cubic symmetry breaking. One method of breaking the cubic symmetry is to make CdTe/HgTe/CdTe quantum wells.

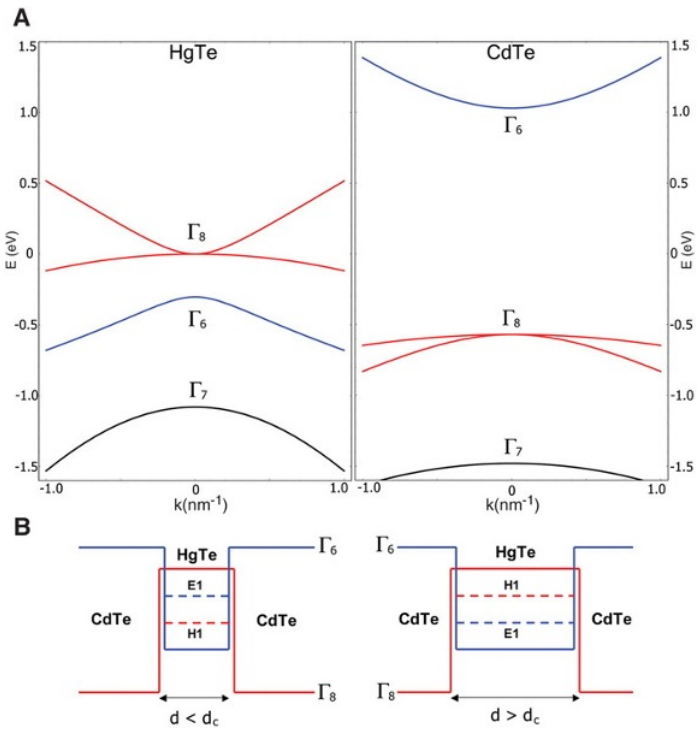

FIGURE 2.6
(A) Bulk energy bands of HgTe and CdTe near the Γ point. (B) The CdTe-HgTe-CdTe quantum well in the normal regime E1 > H1 with $d < d_c$, and in the inverted regime H1 > E1 with $d > d_c$. In this and other figures, Γ8/H1 symmetry is indicated in red, and Γ6/E1 symmetry is indicated in blue.[Taken from Ref.[52] B. A. Bernevig, T. A. HugHes and SC. Zhang, Science(2006).]

Figure 2.6 is a theoretical prediction of the CdTe/HgTe/CdTe quantum well by Bernevig et al. [52]. There are two states, E1 and H1, near the Fermi energy. The parities of states E1 and H1 at the Γ-point are different from each other. The energy

of these two states changes depending on the thickness d of the HgTe layer. The value of $d_c = 60$. If $d < d_c$, it becomes an ordinary insulator; if $d > d_c$, it becomes a topological insulator. Thus, quantum size effects in topological heterojunctions are an exciting subject of investigation.

2.5.2 $Bi_{1-x}Sb_x$ systems

Crystal and electronic structure of Bismuth

The crystal structure of the group-V material Bi is rhombohedral. The Bi rhombohedral crystal structure is a slightly modified NaCl-type (Fig.2.7). The Brillouin zone is similar to that of the face-centered cubic.

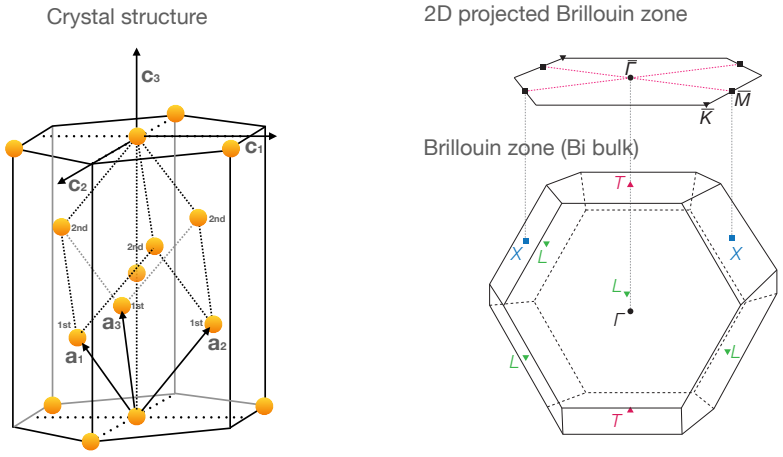

FIGURE 2.7
Crystal structure and Brillouin zone of Bismuth

If Bi crystal structure is the fcc, the T-point has the same symmetry as the L-point. On the other hand, in Bi rhombohedral crystals, the T-point is not equivalent to the L-point due to a slight crystal distortion from fcc. There are two atoms in the Bi unit cell. The Bi atom has five valence electrons, $6s^2 6p^3$, and the p orbitals near the Fermi level contribute to the physical properties. In addition, the electronic state of Bi is a semimetal. In a diatomic fcc crystal structure formed by covalent bonding, electrons clog the bonding bands of the p orbitals, and the crystal exists as a semiconductor. However, since Bi is a single-atom crystal, it is more stable to distort the crystal structure from fcc to gain energy for metallic bonding. Therefore, the T-point of Bi has a hole Fermi surface, and the L-point has an electron Fermi surface.(Fig.2.9). Slightly different conditions, such as lattice distortion, can change the electronic state. For example, Black phosphorus, a group-V material like Bi, is orthorhombic. Such slight differences can change the topology of a material. Therefore, the electronic state of Bi has been the focus of much attention.

The semimetallic electronic structure of Bi makes its physical properties unique. A characteristic feature of semimetals is an electron-hole symmetry condition. As long as the electron-hole symmetry condition is satisfied, there is no limit to the number of carriers. The effective masses of the carriers of L-point electrons and T-point holes

are very different [20]. The band structure at the L point is strongly linear, and there is an electron Fermi surface with an enormous Fermi velocity (Fig 2.9(b,c)). The band structure at the T point shows a hole Fermi surface with weak linearity. The existence of Dirac electrons has also been recognized from the effective Hamiltonian near the L point [19, 53]. Therefore, Bi is well known for its exceptionally long wavelength (∼90 nm) [20] that induces a strong quantum size effect [12, 54]. The Bi/BiSb heterojunction provides an ideal foundation for investigating the quantum size effect in topological heterojunctions.

When Bi is cleaved, we consider the surface Brillouin zone projected from three-dimensions to two-dimensions. The fig 2.7 shows a two-dimensional projected Brillouin zone cleaved in the (111) direction. The $\bar{\text{M}}$-point ($\bar{\Gamma}$-point) in the two-dimensional projected Brillouin zone have information on the three-dimensional bulk X- and L-points (Γ- and T-points). Therefore, we need to investigate the $\bar{M}$ point to confirm the quantum size effect.

Virtual crystal approximation(VCA)

Calculating the electronic structure of diatomic material $A_{0.99}B_{0.01}$ is tough. To perform such a calculation, the size of the compound system's unit cell must be 100 times larger than the unit cell of single crystal A. In addition, the localization of atom B must be taken into account. We want to avoid calculations that would require an enormous amount of computation. Therefore, based on Vegard's law [27, 28], we assume a single virtual atom with the properties of an alloy($A_{1-x}B_x$) by linear extrapolation of the parameters of materials A and B [55]. This approximation is called the virtual crystal approximation [56].

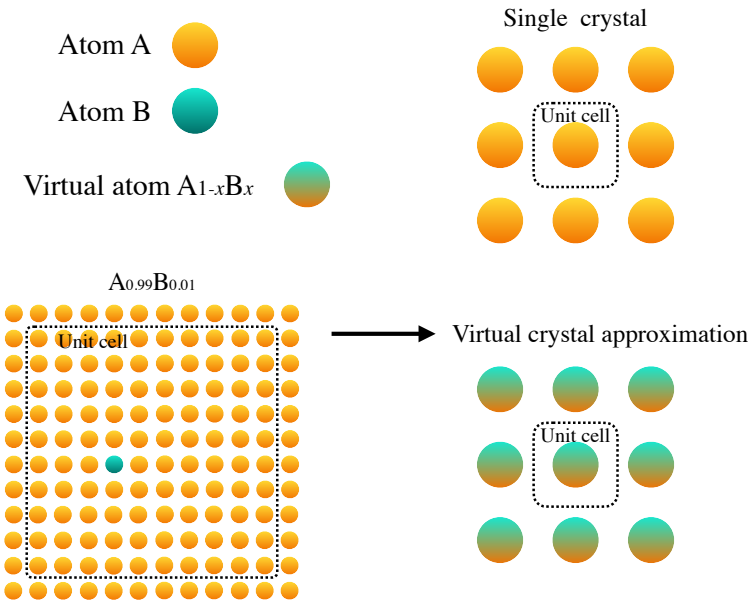

FIGURE 2.8
The concept of virtual crystal approximation.

Topology of BiSb

BiSb is a three-dimensional topological insulator first proposed by Fu and Kane in 2007 [17]. In $Bi_{1-x}Sb_x$, as the Sb content x is increased from pure Bi ($x = 0.00$),

the band at the L-point is inverted at $x \simeq 0.02$[5] (Liu-Allen model calculation [20]), topologically switching from trivial to non-trivial (Fig 2.9(a)) [17, 19, 20]. The band symmetries of bulk Bi and Sb are listed in Tables 2.1 and 2.2.

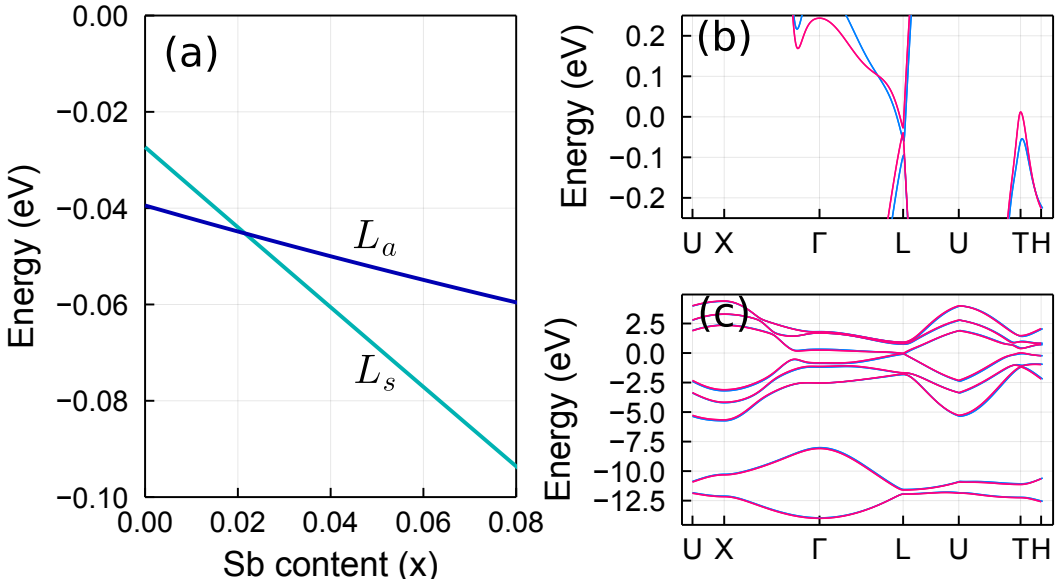

FIGURE 2.9
(a) The Sb content x-dependence of the conduction and valence bands at the L-point of bulk $Bi_{1-x}Sb_x$. The topological transition (band inversion) occurs at $x_c \simeq 0.02$. (b) and (c) Band structure of bulk $Bi_{1-x}Sb_x$, where $x = 0.0$ and $x = 0.08$ are indicated by red and blue lines, respectively.

TABLE 2.1: Band symmetry in the TRIMs of Bismuth

	s	s	p	p	p	p	p	p	δ
1Γ	Γ_6^+	Γ_6^-	Γ_6^+	Γ_6^+	Γ_{45}^+	(Γ_6^-)	(Γ_6^-)	(Γ_{45}^-)	-1
$3L$	L_s	L_a	L_s	L_a	L_a	L_s	(L_s)	(L_a)	-1
$3X$	X_a	X_s	X_s	X_a	X_a	(X_s)	(X_s)	(X_a)	-1
$1T$	T_6^-	T_6^+	T_6^-	T_6^+	(T_{45}^-)	(T_6^+)	(T_{45}^+)	(T_6^-)	-1

TABLE 2.2: Band symmetry in the TRIMs of Antimony

	s	s	p	p	p	p	p	p	δ
1Γ	Γ_6^+	Γ_6^-	Γ_6^+	Γ_6^+	Γ_{45}^+	(Γ_6^-)	(Γ_6^-)	(Γ_{45}^-)	-1
$3L$	L_s	L_a	L_s	L_a	L_s	L_a	(L_s)	(L_a)	1
$3X$	X_a	X_s	X_s	X_a	X_a	(X_s)	(X_s)	(X_a)	-1
$1T$	T_6^-	T_6^+	T_6^-	T_{45}^-	(T_6^+)	(T_6^+)	(T_6^-)	(T_{45}^+)	-1

[5] We adopt the virtual crystal approximation with a linear extrapolation of tight-binding parameters of pure Bi and Sb. Within this approximation, the topological transition occurs at $x \simeq 0.02$, which is less than the experimental value $x^{exp} \simeq 0.04$. The quantitative mismatch can be attributed to the overly simple linear extrapolation. However, this mismatch does not affect the overall quantum size effect findings.

In the table 2.1 and 2.2, s is symmetric, and a is anti-symmetric. Unoccupied bands are denoted by (). The exponent δ in TRIM is switched from -1 to $+1$ by the band inversion at L-point.

Nevertheless, 15 years after Fu-Kane's proposal [17], the discussion about the topology of BiSb is continuing. According to Fu-Kane, the topology of Bi can be determined by whether the Bi(111) surface state intersects the Fermi level an even or odd number of times. If the surface state crosses the Fermi level an even number of times, it is trivial, and if it crosses the Fermi level an odd number of times, it is non-trivial. However, measuring the surface state takes work. The $\bar{M}$-points in the two-dimensional Brillouin zone projected onto the (111) surface reflect the information at the L-point. The L-point band gap and the effective mass of Bi are extremely small. The penetration length of the wave function of the surface state is exceptionally long and is likely to be affected by the substrate and film thickness. Even in an independent system, interference between the top and bottom surfaces persists up to 200 BL [12]. Therefore, it is complicated to obtain the $\bar{M}$-point information necessary for topology determination, which deepens the problem of Bi topology determination.

Quantum well of Bismuth

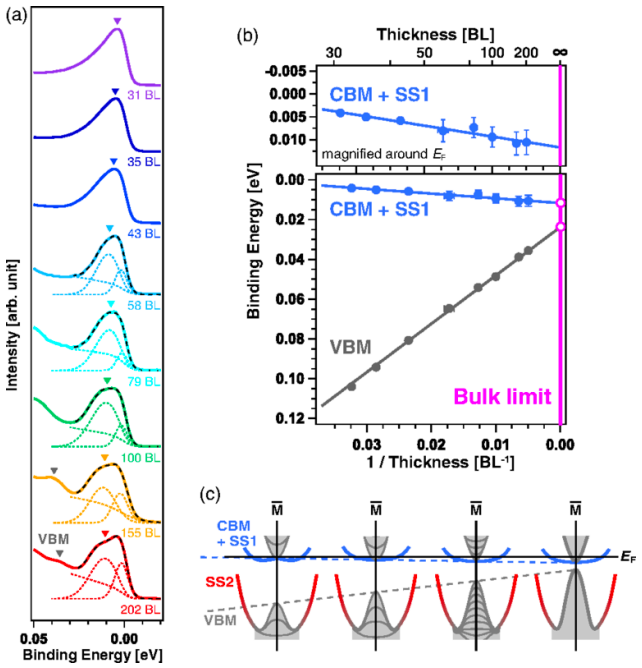

FIGURE 2.10
(a) Energy distribution curves at $\bar{M}$. (b) inverse thickness ($1/N$) dependence of peak positions in (a) and valence band maximum. (c) The evolution in electronic structures of Bi films approaching the bulk limit.[Taken from Ref. [57] S. Ito, B. Feng, M. Arita, et al., Phys. Rev. Lett(2016).]

Ito et al. focused on the quantum well state of Bi [57]. They explained the energy and k_z dependence by measuring the quantum well states for thin films with information perpendicular to the surface. However, the thin film measurement changes to open the band gap due to interference effects between the surface and interface. In systems with

sufficient film thickness to prevent surface-interface interference, it is impossible to measure quantum wells with the resolution of ARPES. In order to solve this problem, Ito et al. measured the electronic structure of the Bi film at different thicknesses. The topology was determined by analyzing the behavior as the film converged to the bulk limit. As a result, Ito et al. proposed to realize a topological phase of Bi[6]. Direct observation of the surface and bulk band structure, which is important for determining the topology of Bi, is difficult. Currently, the small band gap of Bi is not measurable with the resolution of the ARPES experiment [7].

Topological proximity effect

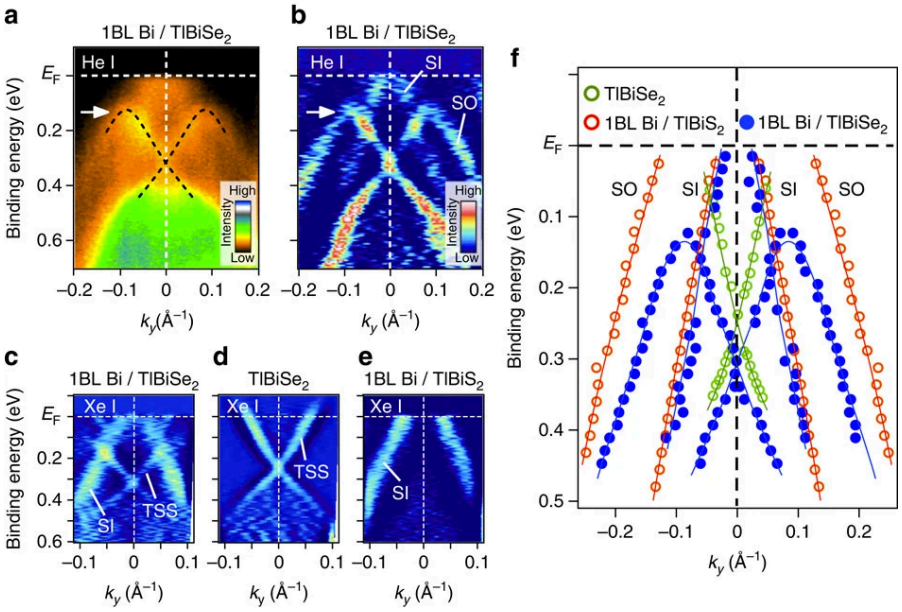

FIGURE 2.11
(a,b) ARPES intensity and second-derivative intensity for $Bi(1BL)/TlBiSe_2$. (c–e) Second-derivative intensity for $Bi(1BL)/TlBiSe_2$, $TlBiSe_2$ and $Bi(1BL)/TlBiS_2$ (f) Experimental band dispersions.[Taken from Ref. [14] T. Shoman, A. Takayama, T. Sato, et al., Nat. Commun(2015).]

A topological proximity effect is a unique physical phenomenon in topological heterojunction systems. It is a relatively new topic, discovered in 2015 by Shoman et

[6]Figure. 2.10(b) shows the $1/thickness$ dependence of the surface states, the conduction band maximum, and the valence band minimum. Bi is assumed to be non-trivial because the band gap is open in the bulk limit ($1/thickness = 0$).

[7]Angle-Resolved PhotoEmission Spectroscopy (ARPES) experiments can directly observe the energy-momentum relationship of electrons in materials. The surface state of the first three-dimensional topological insulator $Bi_{1-x}Sb_x$ was discovered by ARPES in 2008 [58]. Since then, topological insulators, e.g., Bi_2Se_3 and Bi_2Te_3 have been discovered. Research is rapidly progressing to understand the physical properties of these topological insulators. ARPES measurements are suitable for measuring topological surface states because of their surface sensitivity. Therefore, ARPES measurements are becoming increasingly important. For example, observing surface states can determine the topology of the $Bi_{1-x}Sb_x$ system. However, insufficient resolution of ARPES has led to conflicts over whether the topology of the Bi is trivial or non-trivial[57, 59, 60].

al. [14]. The trivial/non-trivial insulator heterojunction system has been widely investigated both theoretically and experimentally [4, 15, 16, 51, 52, 61]. This report by Shoman et al. is new in that they bonded a metallic Bi ultrathin film (1 BL) to the topological insulator $TlBiSe_2$. This paper reported that the topological surface state appears on the metallic Bi surface of Bi(1 BL)/$TlBiSe_2$ heterojunction. In Fig. 2.11(a), there is a black dotted line, which is a modulated Dirac cone. In Bi(1 BL)/$TlBiSe_2$, the topological insulator surface state exists on the Bi surface.

The numerical simulation for ZnM/Bi_2Se_3 (M=S, Se, Te) by Wu et al. also reported that the topological surface state appears on the surface of a trivial material (ZnM ultrathin film)[13]. Several pioneering works, numerical simulations by Wu et al. and experimental evidence by Shoman et al., report topological proximity effects. The attached trivial material is only one thick atomic layer in these works. However, ultrathin heterojunctions make it difficult to investigate how quantum size effects affect topological heterojunctions. The difficulty arises due to the surface not separating from the surface, interface, and bulk, resulting in too much interference.

In particular, BiSb, our target material in this study, is known to change even topologically protected conditions due to quantum size effects[12, 54]. In addition, when the electron wavelength is long-range, as in Bi/BiSb, quantum size effects appear strongly. The effective mass of Bi is on the order of $m^* = 0.001m_e$, which is extremely small among topological materials[62]. Compared to the electrons at the $\bar{\Gamma}$ point of $TlBiTe_2$/$InBiTe_2$ topological heterojunction[63, 64], which have Dirac-like electrons, the electrons at the $\bar{M}$ point of Bi/BiSb topological heterojunction have an unusually small effective mass. Compared to the electrons at the $\bar{\Gamma}$-point of the $TlBiTe_2$/$InBiTe_2$ heterojunction, which has Dirac-like electrons, the electrons at the $\bar{M}$-point of the Bi/BiSb heterojunction have a minimal effective mass. In addition, the effective masses of electrons and holes in Bi/BiSb systems are strongly anisotropic: $m^*/m_e = 0.00585$ for electrons at $\bar{M}$ point, $m^*/m_e = 0.721$ for holes at $\bar{\Gamma}$ point. Therefore, we infer from the anisotropy of the effective mass in the Bi/BiSb heterojunction system that the quantum size effect is wave number dependent.

Analytical solution for the surface state of BiSb

This section presents an analytical solution for the surface state of finite-thickness BiSb proposed by Fuseya and Fukuyama[12]. It is well established that the effective Hamiltonian for a bulk system with strong spin-orbit coupling is commonly represented by the Wolff Hamiltonian[65, 66], which is fundamentally equivalent to the Dirac Hamiltonian but with spatial anisotropy[19]. The Wolff Hamiltonian is derived by applying $k \cdot p$ theory exclusively to a two bands of a system, i.e., the conduction and valence band. The original Wolff Hamiltonian does not incorporate contributions from other bands. However, the surface state of BiSb that arises from spin-orbit coupling possesses contributions from other bands. Thus, this section presents an extended Wolff Hamiltonian utilizing Löwdin partitioning up to the second order[67, 68]. The extended Wolff Hamiltonian is described by

$$\mathcal{H} = \begin{pmatrix} \Delta + \epsilon'(\boldsymbol{p}) & i\boldsymbol{p} \cdot \left[\sum_\mu \boldsymbol{W}(\mu)\sigma_\mu\right] \\ -i\boldsymbol{p} \cdot \left[\sum_\mu \boldsymbol{W}(\mu)\sigma_\mu\right] & -\Delta - \epsilon'(\boldsymbol{p}) \end{pmatrix} \tag{2.37}$$

where

$$\epsilon'(\boldsymbol{p}) = \frac{\boldsymbol{p} \cdot \boldsymbol{\alpha}' \cdot \boldsymbol{p}}{2}. \tag{2.38}$$

ϵ' is the contribution from the other bands, α' is an inverse effective mass tensor, σ_μ is the Pauli matrix ($\mu = 1, 2, 3$), and the vectors $\boldsymbol{W}(\mu)$ are the matrix element of the velocity operator[66]. The z-axis was set as to be perpendicular to the surface and we consider a thin film with a finite-thickness L, where $|z| \leq L/2$ is the thin film and $|z| > L/2$ is a vacuum. The Hamiltonian for this system is commonly represented by the substitution $p_z \to -i\hbar\nabla_z$. The $p_{x,y} (= \hbar k_{x,y})$ will not be considered to be an operator. The in-plane wave numbers $k_{x,y}$ are good quantum numbers. By incorporating an ansatz wave function of the form $\phi = e^{\lambda z}$ into the extended Wolff Hamiltonian, equation 2.37 is transformed into the following form

$$\mathcal{H} = \begin{pmatrix} \Delta + \xi' - \frac{\alpha_{zz}}{2}\Lambda^2 & iK_\mu\sigma_\mu \\ -iK_\mu\sigma_\mu & -(\Delta + \xi' - \frac{\alpha_{zz}}{2}\Lambda^2) \end{pmatrix}, \tag{2.39}$$

where $\lambda = \Lambda/\hbar (> 0)$ is the inverse of the localization length, and

$$K_\mu = p_x W_x(\mu) + p_y W_y(\mu) - i\Lambda W_z(\mu). \tag{2.40}$$

By separating α' into parallel (x, y) and perpendicular (z) components of the plane, we get the following equations

$$\alpha'(\boldsymbol{p}) = \xi' - \frac{\alpha'_{zz}}{2}\Lambda^2 \tag{2.41}$$

$$\xi' = \frac{1}{2}\left(\alpha'_{xx}p_x^2 + \alpha'_{yy}p_y^2 + 2\alpha'_{xy}p_x p_y\right). \tag{2.42}$$

The eigenvalues of this extended Wolff Hamiltonian are obtained by considering its square ($\mathcal{H}^2\psi = E^2\psi$),

$$\mathcal{H}^2 = \begin{pmatrix} \left(\Delta + \xi' - \frac{\alpha_{zz}}{2}\Lambda^2\right)^2 \boldsymbol{I} + (iK_\mu\sigma_\mu)^2 & \mathbf{0} \\ \mathbf{0} & \left(\Delta + \xi' - \frac{\alpha_{zz}}{2}\Lambda^2\right)^2 \boldsymbol{I} + (iK_\mu\sigma_\mu)^2 \end{pmatrix}. \tag{2.43}$$

Using a relation

$$(K_\mu\sigma_\mu)^2 = 2\Delta\left(\xi - \alpha_z z\Lambda^2/2\right), \tag{2.44}$$

where the inverse effective mass

$$\alpha_{ij} = \frac{1}{\Delta}W_i(\mu)W_j(\mu), \tag{2.45}$$

, the in-plane dispersion

$$\xi = \frac{1}{2}\left(\alpha_{xx}p_x^2 + \alpha_{yy}p_y^2 + 2\alpha_{xy}p_xp_y\right), \tag{2.46}$$

we can obtain the eigenvalues[8]

$$E = \pm\sqrt{\left(\Delta + \xi' - \frac{\alpha'_{zz}}{2}\Lambda^2\right)^2 + 2\Delta\left(\xi - \frac{\alpha_{zz}}{2}\Lambda^2\right)}. \tag{2.48}$$

From equation 2.48, we can obtain Λ as a function E in the form

$$\Lambda_n^2(E) = \frac{2\Delta}{{\alpha'}_{zz}^2}\Bigg[\alpha_{zz} + {\alpha'}_{zz}\left(1 + \frac{\xi'}{\Delta}\right) \pm \sqrt{\alpha_{zz}\left(\alpha_{zz} + 2{\alpha'}_{zz}\right) + {\alpha'}_{zz}^2\left(\frac{E}{\Delta}\right)^2 + 2{\alpha'}_{zz}\left(\alpha_{zz}\frac{\xi'}{\Delta} - {\alpha'}_{zz}\frac{\xi}{\Delta}\right)}\Bigg], \tag{2.49}$$

where the sign of square root is defined to as $+$ for $n = 1$ and $-$ for $n = 2$. As the eigenvalues are doubly degenerate, the corresponding wave function can be expressed

[8]The energy of bulk

$$E_{bulk} = \pm\sqrt{(\Delta + \xi')^2 + 2\Delta\xi}. \tag{2.47}$$

as a linear combination of two linearly independent eigenfunctions[9][10],

$$\psi_{1mn} = \begin{pmatrix} E+1+\xi'-\frac{\alpha'_{zz}}{2}\Lambda^2 \\ 0 \\ -i\left(P_3 - im\Lambda_n Z_3\right) \\ -i\left(P_+ - im\Lambda_n Z_3\right) \end{pmatrix}, \tag{2.51}$$

$$\psi_{2mn} = \begin{pmatrix} 0 \\ E+1+\xi'-\frac{\alpha'_{zz}}{2}\Lambda^2 \\ -i\left(P_- - im\Lambda_n Z_-\right) \\ -i\left(P_3 - im\Lambda_n Z_3\right) \end{pmatrix}, \tag{2.52}$$

where

$$P_\mu = p_x W_x(\mu) + p_y W_y(\mu), \tag{2.53}$$
$$P_\pm = P_1 \pm iP_2, \tag{2.54}$$
$$Z_\mu = W_z(\mu), \tag{2.55}$$
$$Z_\pm = Z_1 \pm iZ_2. \tag{2.56}$$

The general solution for the wave function is given by a linear combination of eight eigenfunctions[11]

$$\Psi(z) = \sum_{l=1,2}\sum_{m=\pm}\sum_{n=1,2} C_{lmn}\psi_{lmn}e^{m\lambda_n z}, \tag{2.57}$$

taking into account $n = 1, 2$ and $m = \pm$ in $e^{\pm\Lambda_n z/\hbar}$.

- Semi-infinite system

  The boundary conditions are given by

$$\Psi(0) = \Psi(\infty) = 0. \tag{2.58}$$

The condition $\Psi(\infty) = 0$ requires $m = -$, therefore the wave function is given as a linear combination of four eigenfunctions

$$\Psi(z) = \left(C_{1-1}\psi_{1-1} + C_{2-1}\psi_{2-1}\right)e^{-\lambda_1 z} + \left(C_{1-2}\psi_{1-2} + C_{2-2}\psi_{2-2}\right)e^{-\lambda_2 z} \tag{2.59}$$

By utilizing the condition $\Psi(0) = 0$, the four eigenfunctions conform to

$$0 = C_{1-1}\psi_{1-1} + C_{2-1}\psi_{2-1} + C_{1-2}\psi_{1-2} + C_{2-2}\psi_{2-2}. \tag{2.60}$$

This lead to the eigenfunctions in the form

$$\Psi(z) = \left(C_{1-1}\psi_{1-1} + C_{2-1}\psi_{2-1}\right)\left(e^{-\lambda_2 z} - e^{-\lambda_1 z}\right). \tag{2.61}$$

[9] The unit of the energy Δ set to 1.

[10] The summation

$$\begin{aligned}\sum_\mu K_\mu\sigma_\mu &= (P_1 - i\Lambda Z_1)\begin{pmatrix}0 & 1\\ 1 & 0\end{pmatrix} + (P_2 - i\Lambda Z_2)\begin{pmatrix}0 & -i\\ i & 0\end{pmatrix} + (P_3 - i\Lambda Z_3)\begin{pmatrix}1 & 0\\ 0 & -1\end{pmatrix} \\ &= \begin{pmatrix}P_3 - im\Lambda_n Z_3 & P_- - im\Lambda_n Z_- \\ P_+ - im\Lambda_n Z_+ & -P_3 + im\Lambda_n Z_3\end{pmatrix}.\end{aligned} \tag{2.50}$$

[11] C_{lmn} is a normalization constant.

The secular equation of equation 2.60 is

$$\begin{vmatrix} \left(E+1+\xi'-\frac{\alpha'_{zz}}{2}\Lambda_1^2\right)\boldsymbol{I} & \left(E+1+\xi'-\frac{\alpha'_{zz}}{2}\Lambda_2^2\right)\boldsymbol{I} \\ -i\left(P_\mu+i\Lambda_1 Z_\mu\right)\sigma_\mu & -i\left(P_\mu+i\Lambda_2 Z_\mu\right)\sigma_\mu \end{vmatrix} = 0 \tag{2.62}$$

From the secular equation 2.62, we obtain

$$(\Lambda_1-\Lambda_2)^2\left[\frac{\alpha'^2_{zz}}{4}\xi\left(\Lambda_1+\Lambda_2\right)^2-\frac{\alpha_{zz}}{2}\left(E+1+\xi'-\frac{\alpha'_{zz}}{2}\Lambda_1\Lambda_2\right)^2\right]=0 \tag{2.63}$$

By substituting $\Lambda_{1,2}$ into equation 2.63, we can obtain the following equation

$$\left(E+1+\xi'-\beta\xi\right)\left\{1+\xi'+\mathrm{sgn}(\beta)\sqrt{\left(1+\xi'\right)^2+2\xi-E^2}\right\}=0, \tag{2.64}$$

where

$$\beta=\frac{\alpha'_{zz}}{\alpha_{zz}}. \tag{2.65}$$

The parameter β is of significant importance as it characterizes the relative curvature of contributions from other bands. The sign of β is closely linked to the topological characteristics of the system. Finally, the energy dispersion[12] are as follows

$$E_{s1\pm}=\pm\sqrt{2\xi}, \tag{2.67}$$

where $\beta<0$ and $1+\xi'>0$ for solution (I-a); $\beta>0$ and $1+\xi'<0$ for solution (I-b).

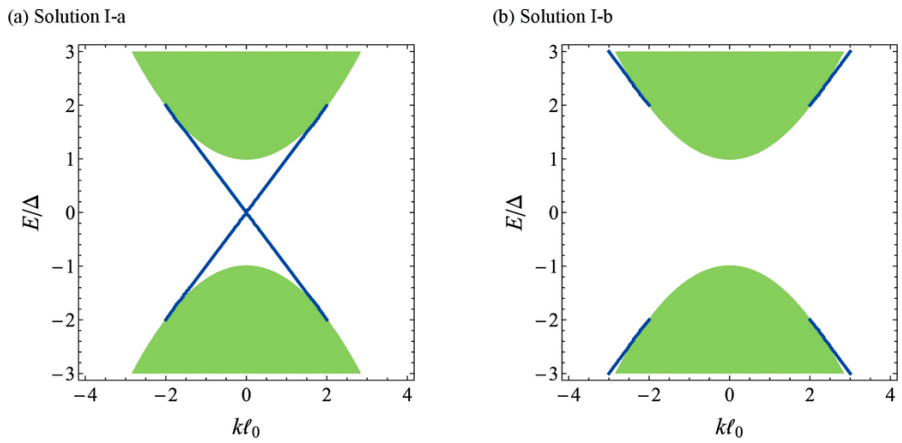

FIGURE 2.12
Analytical solution for semi-infinite system. (a) Solution I-a ($\beta=-0.1$, $\alpha_\parallel=1.0/m$, $\alpha'_\parallel=-0.5/m$) and (b) Solution I-b ($\beta=0.1$, $\alpha_\parallel=1.0/m$, $\alpha'_\parallel=-0.5/m$) [Taken from Ref. [12] Y. Fuseya and H. Fukuyama, JPSJ(2018).]

[12]The corresponding wave function for the solution II,

$$E_{s2\pm}=\pm\left(1+\xi'-\beta\xi\right), \tag{2.66}$$

becomes zero.

In addition, the inverse localization length Λ of solution I is obtained as

$$\Lambda_{1,2}^2 = \frac{2}{\alpha_{zz}\beta^2}\left[1+\beta\left(1+\xi'\right) \pm \sqrt{1+2\beta\left(1+\xi'\right)}\right]. \tag{2.68}$$

- Finite-thickness system

The boundary conditions are given by

$$\Psi(L/2) = \Psi(-L/2) = 0. \tag{2.69}$$

The wave function is given as a linear combination of eight eigenfunctions 2.57, with terms including C_{1+1} and C_{1-1} being explicitly written as

$$\begin{aligned}
\Psi_{1,1}(z) &= C_{1+1}\psi_{1+1}e^{\lambda_1 z} + C_{1-1}\psi_{1-1}e^{-\lambda_1 z} \\
&= \begin{pmatrix} \left(E+1+\xi'-\frac{\alpha'_{zz}}{2}\Lambda_1^2\right)\left(C_{1+1}e^{\lambda_1 z}+C_{1-1}e^{-\lambda_1 z}\right) \\ 0 \\ -iP_3\left(C_{1+1}e^{\lambda_1 z}+C_{1-1}e^{-\lambda_1 z}\right)+\Lambda_1 Z_3\left(-C_{1+1}e^{\lambda_1 z}+C_{1-1}e^{-\lambda_1 z}\right) \\ -iP_+\left(C_{1+1}e^{\lambda_1 z}+C_{1-1}e^{-\lambda_1 z}\right)+\Lambda_1 Z_+\left(-C_{1+1}e^{\lambda_1 z}+C_{1-1}e^{-\lambda_1 z}\right) \end{pmatrix} \\
&= \begin{pmatrix} \left(E+1+\xi'-\frac{\alpha'_{zz}}{2}\Lambda_1^2\right)\left\{D_1\cosh\lambda_1 z + D_2\sinh\lambda_1 z\right\} \\ 0 \\ -iP_3\left\{D_1\cosh\lambda_1 z + D_2\sinh\lambda_1 z\right\}-\Lambda_1 Z_3\left\{D_1\sinh\lambda_1 z + D_2\cosh\lambda_1 z\right\} \\ -iP_+\left\{D_1\cosh\lambda_1 z + D_2\sinh\lambda_1 z\right\}-\Lambda_1 Z_+\left\{D_1\sinh\lambda_1 z + D_2\cosh\lambda_1 z\right\} \end{pmatrix}
\end{aligned} \tag{2.70}$$

where $D_1 = C_{1+1} + C_{1-1}$ and $D_2 = C_{1+1} - C_{1-1}$. Similarly, the terms including C_{2+1} and C_{2-1} are given as

$$\Psi_{2,1}(z) = \begin{pmatrix} 0 \\ \left(E+1+\xi'-\frac{\alpha'_{zz}}{2}\Lambda_1^2\right)\left\{D_3\cosh\lambda_1 z + D_4\sinh\lambda_1 z\right\} \\ -iP_-\left\{D_3\cosh\lambda_1 z + D_4\sinh\lambda_1 z\right\}-\Lambda_1 Z_-\left\{D_3\sinh\lambda_1 z + D_4\cosh\lambda_1 z\right\} \\ -iP_+\left\{D_3\cosh\lambda_1 z + D_4\sinh\lambda_1 z\right\}-\Lambda_1 Z_3\left\{D_3\sinh\lambda_1 z + D_4\cosh\lambda_1 z\right\} \end{pmatrix}, \tag{2.71}$$

where $D_3 = C_{2+1} + C_{2-1}$ and $D_4 = C_{2+1} - C_{2-1}$. $\Psi_{2,1}$ and $\Psi_{2,2}$ can be obtained by changing $n = 1 \to 2$ and their coefficients $D_{1-4} \to D_{5\to 8}$. The eight simultaneous equations for D_{1-8}, derived from the boundary condition, yield a secular equation (8×8) which is given by the following equations:

$$|L| = \begin{vmatrix} L_1 & L_2 \\ L_3 & L_4 \end{vmatrix}, \tag{2.72}$$

where

$$L_1 = \begin{pmatrix} E_1\cosh\lambda_1 z\boldsymbol{I} & E_1\sinh\lambda_1 z\boldsymbol{I} \\ -\Lambda_1\sinh\lambda_1 z Z_\mu\sigma_\mu - i\cosh\lambda_1 z P_\mu\sigma_\mu & -\Lambda_1\cosh\lambda_1 z Z_\mu\sigma_\mu - i\sinh\lambda_1 z P_\mu\sigma_\mu \end{pmatrix}, \tag{2.73}$$

$$L_2 = L_1(1\to 2), \tag{2.74}$$

$$L_3 = L_1(S_1 \to -S_1), \tag{2.75}$$

$$L_4 = L_2(S_2 \to -S_2), \tag{2.76}$$

and

$$E_n = E + 1 + \xi' - \frac{\alpha'_{zz}}{2}\Lambda_n^2. \tag{2.77}$$

|L| is given by

$$\begin{aligned}|L| = 16\Big[&2\xi(E_1 - E_2)^2 \cosh\lambda_1 z \cosh\lambda_2 z \sinh\lambda_1 z \sinh\lambda_2 z \\ &- \alpha_{zz}(E_1\Lambda_2 \cosh\lambda_1 z \sinh\lambda_2 z - E_2\Lambda_1 \cosh\lambda_2 z \sinh\lambda_1 z) \\ &\times (E_1\Lambda_2 \cosh\lambda_2 z \sinh\lambda_1 z - E_2\Lambda_1 \cosh\lambda_1 z \sinh\lambda_2 z)\Big]^2.\end{aligned} \tag{2.78}$$

Using the three relations[13], we can obtain the analytical solution:

$$\begin{aligned}0 = &2\xi(E1 - E2)^2 \tanh\lambda_1 z \tanh\lambda_2 z \\ &- \alpha_{zz}(E_1\lambda_2 \tanh\lambda_2 z - E_2\lambda_1 \tanh\lambda_1 z)(E_1\lambda_2 \tanh\lambda_1 z - E_2\lambda_1 \tanh\lambda_2 z)\end{aligned} \tag{2.82}$$

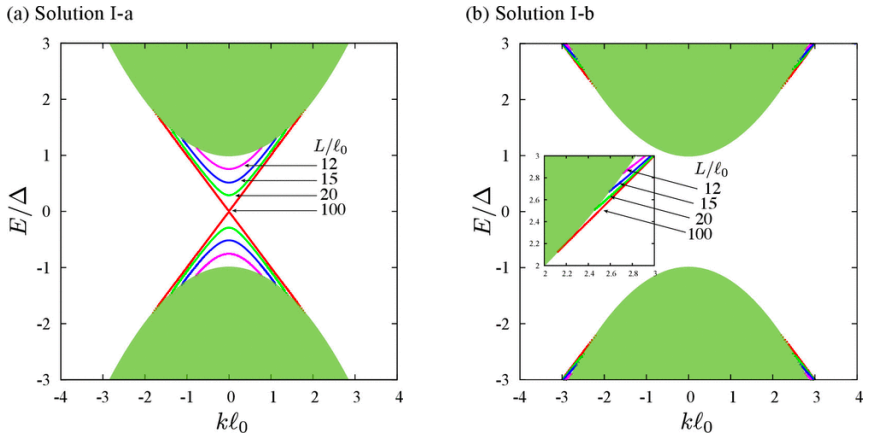

FIGURE 2.13
Analytical solution for finite thickness system: $L/l = 12, 15, 20$,and 100, $\alpha_{zz} = 100/m$, $\alpha_{\|} = 1/m$, and $\alpha'_{\|} = -0.5/m$. (a) Solution I-a: $\alpha'_{zz} = -1(\beta = -0.01)$. (b) Solution I-b: $\alpha'_{zz} = 1(\beta = 0.01)$ [Taken from Ref. [12] Y. Fuseya and H. Fukuyama, JPSJ(2018).]

[13]The three relations are described by

$$\sum_\mu P_\mu^2 = 2\Delta\xi, \tag{2.79}$$

$$\sum_\mu Z_\mu^2 = \Delta\alpha_{zz}, \tag{2.80}$$

$$\begin{aligned}&4(P_1P_2Z_1Z_2 + P_2P_3Z_2Z_3 + P_3P_1Z_3Z_1) \\ &\quad + P_1^2(Z_1^2 - Z_2^2 - Z_3^2) + P_2^2(-Z_1^2 + Z_2^2 - Z_3^2) + P_3^2(-Z_1^2 - Z_2^2 + Z_3^2) \\ &= \Delta^2\left[(2\alpha_{xz}^2 - \alpha_{xx}\alpha_{zz})p_x^2 + (2\alpha_{yz}^2 - \alpha_{yy}\alpha_{zz})p_y^2 + (2\alpha_{xz}\alpha_{yz} - \alpha_{xy}\alpha_{zz})p_xp_y\right]\end{aligned} \tag{2.81}$$

2.5.3 $Pb_{1-x}Sn_xTe$ systems

Crystal structure of PbSnTe

$Pb_{1-x}Sn_xTe$ is a well-known material that has been studied in the semiconductor materials field[69–71]. Its crystal structure is a rock-salt (fcc) structure, unlike distorted Bi[55]. This material is a narrow-gap semiconductor, and band inversion occurs in the L point for x=0.04[72]. However, it is not topologically inversion because the number of TRIMs that are band-inversion point is an even number. From band calculations, PbTe and SnTe are trivial insulators in the Z_2 classification.

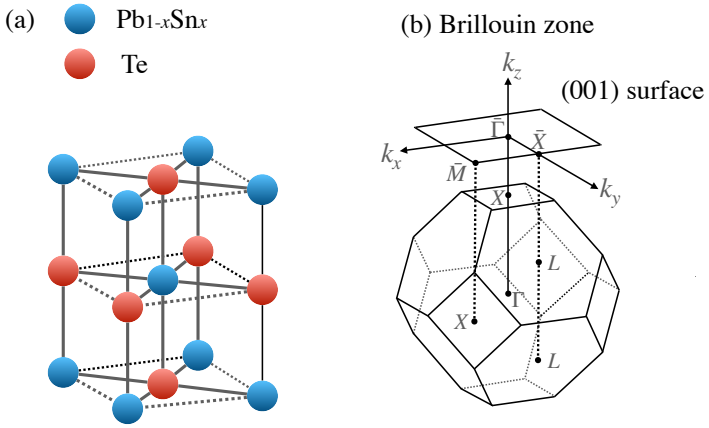

FIGURE 2.14
Crystal structure and Brillouin zone of PbSnTe

Topological crystalline insulator

PbSnTe is not a Z_2 topological insulator. However, it is a topological material with surface and edge states protected by the crystal point group symmetry of the crystal lattice instead of time-reversal symmetry. Such a material is called a topological crystalline insulator[73–75]. The topological invariants are defined by the crystal's rotational and mirror symmetry. Two Dirac cones would appear near the $\bar{X}$-point because $\bar{X}$-point of the SnTe surface Brillouin zone has two bulk L-points projected[76]. There have been studies on PbTe/SnTe heterojunction systems for a long time[4, 77]. Recently, topological crystalline insulator/ordinary insulator topological heterojunction has also been studied[51, 61].

PbTe/SnTe heterojunction

$Pb_{1-x}Sn_xTe$ shows a band inversion around x=0.04 at the L-point [72]. As a result, $Pb_{1-x}Sn_xTe$ transitions from a trivial insulator to a topological crystalline insulator [73, 74, 76]. When a topological crystalline insulator SnTe contacts an obvious insulator PbTe with a similar crystal structure, the band gap is expected to close at the interface [61]. Weyl and Dirac fermions are also involved in the conduction state at the interface. In this case, we expect the band alignment of the topological heterojunction system to be as shown in Fig. 2.15 (a).

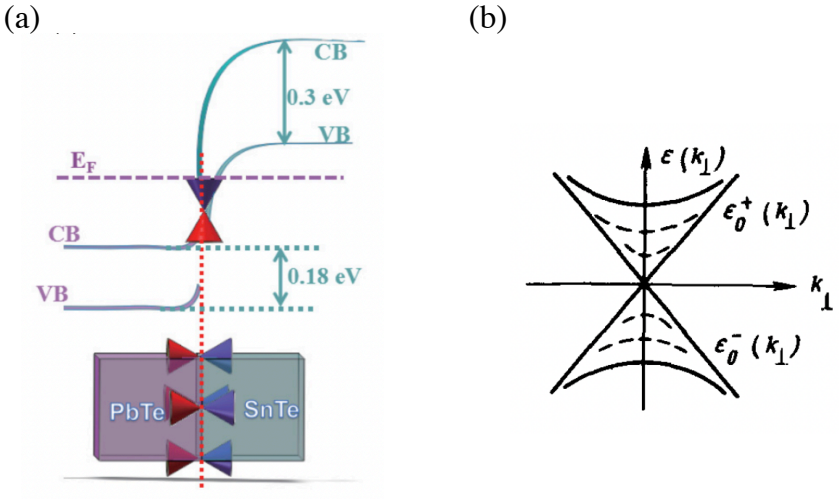

FIGURE 2.15
(a) Band alignment of the PbTe/SnTe topological heterojunction system. [Taken from Ref.[61] F. Wei, CW. Liu, D. Li, et al., Phys. Rev. B(2018).] (b) Energy spectrum of inverted contact at interface.[Taken from Ref.[4] B. A. Volkov and O. A. Pankratov, JETP Letter(1985).]

2.6 Purpose of this resarch

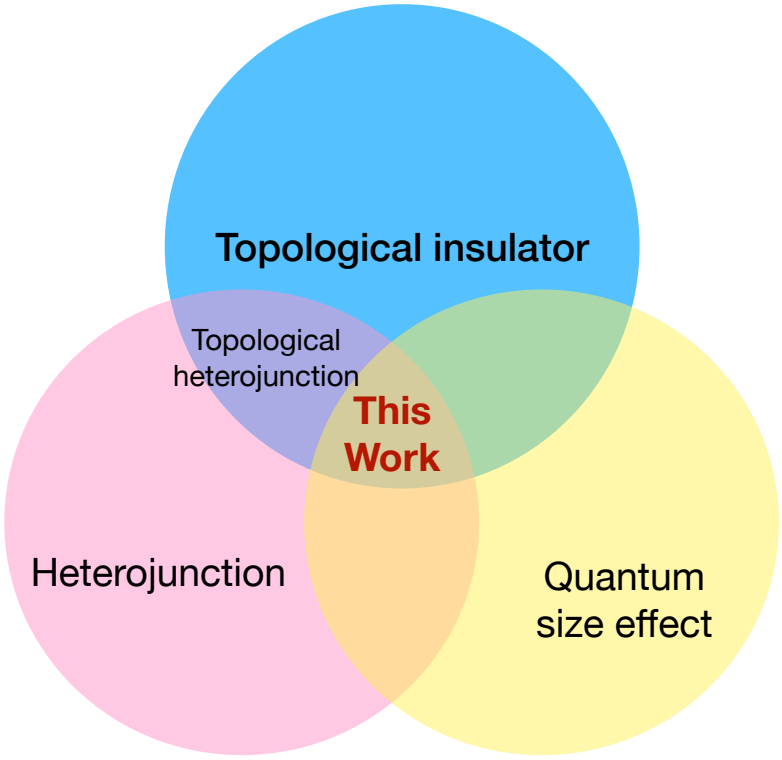

FIGURE 2.16
Areas of coverage for this research.

Based on the background described above, the purpose of this study is to be explained. The field of this study is a complex area that combines topological insulators, heterojunctions, and quantum size effects. In particular, the focus is on the Bi/BiSb heterostructure system. A model will be described in the next chapter (chapter 3) to investigate this system. In the following results chapter (chapter 4), a multidimensional analysis was conducted on the Bi/BiSb system. Additionally, comparisons were made with other systems in chapter 5, and verification was performed on quantum size effects in topological heterostructures.

Chapter 3

Tight-binding model and numerical caluculation

In this chapter, we explain the tight-binding model used in this study. In particular, we mention the Bi(111) surface and surface potentials. We also discuss the PbSnTe(001) surface using the Lent model. In addition, this chapter contained an explanation of numerical calculations.

3.1 Liu-Allen model

The Liu-Allen model is famous for the bulk electronic states of Bi and Sb[20]. The bulk of Bi and Sb has a rhombohedral crystal structure, a trigonally distorted fcc lattice of two atoms in one unit cell, which are interpenetrated with each other (Fig2.7). Table 3.1 shows the parameters related to the crystal structure.

TABLE 3.1: Crystal structure parameter of Bi and Sb at 4.2 K. [78, 79]

		Bi	Sb
Lattice constant	a (Å)	4.5332	4.3007
	c (Å)	11.7967	11.2221
Rhombohedral angle	α	57°19’	57°14’
Internal displacement parameter	μ	0.2341	0.2336
reciprocal-lattice constant	g	1.3861	1.4610
Nearest-neighber distance	d_1	3.0624	2.9024
Next nearest-neighber distance	d_2	3.5120	3.3427

The three primitive translation vectors of lattice are

$$\boldsymbol{a}_1 = \left(-\frac{1}{2}a, -\frac{\sqrt{3}}{6}a, \frac{1}{3}c\right), \tag{3.1}$$

$$\boldsymbol{a}_2 = \left(\frac{1}{2}a, -\frac{\sqrt{3}}{6}a, \frac{1}{3}c\right), \tag{3.2}$$

$$\boldsymbol{a}_3 = \left(0, -\frac{\sqrt{3}}{3}a, \frac{1}{3}c\right). \tag{3.3}$$

The three corresponding reciprocal-lattice vectors of lattice are given by

$$\boldsymbol{b}_1 = \left(-1, -\frac{\sqrt{3}}{3}, b\right) g, \tag{3.4}$$

$$\boldsymbol{b}_2 = \left(1, -\frac{\sqrt{3}}{3}, b\right) g, \tag{3.5}$$

$$\boldsymbol{b}_3 = . \left(0, 2\frac{\sqrt{3}}{3}, b\right) g, \tag{3.6}$$

where

$$b = a/c. \tag{3.7}$$

The relative position of the two basis atoms is given by

$$\boldsymbol{d} = (0, 0, 2\mu)\, c. \tag{3.8}$$

The vectors from a central atom to the nearest neighbors are

$$\boldsymbol{a}_1 - \boldsymbol{d}, \boldsymbol{a}_2 - \boldsymbol{d}, \boldsymbol{a}_3 - \boldsymbol{d}. \tag{3.9}$$

The vectors from a central atom to the next nearest neighbors are

$$\boldsymbol{a}_1 + \boldsymbol{a}_2 - \boldsymbol{d}, \boldsymbol{a}_1 + \boldsymbol{a}_3 - \boldsymbol{d}, \boldsymbol{a}_2 + \boldsymbol{a}_3 - \boldsymbol{d}. \tag{3.10}$$

Liu-Allen model has 14 adjustable parameters (Table 3.2, Table 3.3 and Table 3.4). E_s and E_p are the on-site orbital energy. $V_{ss\sigma}, V_{sp\sigma}, V_{pp\sigma}$ and $V_{pp\pi}$ are for the nearest neighbors hopping. $V'_{ss\sigma}, V'_{sp\sigma}, V'_{pp\sigma}$ and $V'_{pp\pi}$ are for the 2nd nearest neighbors hopping. $V''_{ss\sigma}, V''_{sp\sigma}, V''_{pp\sigma}$ and $V''_{pp\pi}$ are for the 3rd nearest neighbors hopping. And the spin-orbit coupling parameters are $\lambda_{\mathrm{Sb}} = 0.6(\mathrm{eV})$ for Sb and $\lambda_{\mathrm{Bi}} = 1.5(\mathrm{eV})$ for Bi[80].

TABLE 3.2: On-site orbital energy and hopping parameter for the nearest neighbors of Bi and Sb.

		Bi	Sb
Orbital energy (s-orbitals)	E_s	-10.906	-10.068
Orbital energy (p-orbitals)	E_p	-0.486	-0.926
Hopping parameter ($ss\sigma$)	$V_{ss\sigma}$	-0.608	-0.694
Hopping parameter ($sp\sigma$)	$V_{sp\sigma}$	1.320	1.554
Hopping parameter ($pp\sigma$)	$V_{pp\sigma}$	1.854	2.342
Hopping parameter ($pp\pi$)	$V_{pp\pi}$	-0.600	-0.582

TABLE 3.3: Hopping parameter for the next nearest neighbors of Bi and Sb.

		Bi	Sb
Hopping parameter ($ss\sigma$)	$V'_{ss\sigma}$	-0.384	-0.366
Hopping parameter ($sp\sigma$)	$V'_{sp\sigma}$	0.433	0.478
Hopping parameter ($pp\sigma$)	$V'_{pp\sigma}$	1.396	1.418
Hopping parameter ($pp\pi$)	$V'_{pp\pi}$	-0.344	-0.393

TABLE 3.4: Hopping parameter for the 3rd neighbors of Bi and Sb.

		Bi	Sb
Hopping parameter $(ss\sigma)$	$V''_{ss\sigma}$	0	0
Hopping parameter $(sp\sigma)$	$V''_{sp\sigma}$	0	0
Hopping parameter $(pp\sigma)$	$V''_{pp\sigma}$	0.156	0.352
Hopping parameter $(pp\pi)$	$V''_{pp\pi}$	0	0

The direction cosines for the nearest neighbors and the next neighbors are also given by

$$\begin{pmatrix}\alpha_{1st}\\ \beta_{1st}\\ \gamma_{1st}\end{pmatrix} = \arccos\left(\frac{|\boldsymbol{a}_2-\boldsymbol{d}|}{\sqrt{(\boldsymbol{a}_2-\boldsymbol{d})\cdot(\boldsymbol{a}_2-\boldsymbol{d})}}\right), \tag{3.11}$$

$$\begin{pmatrix}\alpha_{2nd}\\ \beta_{2nd}\\ \gamma_{2nd}\end{pmatrix} = \arccos\left(\frac{|\boldsymbol{a}_1+\boldsymbol{a}_3-\boldsymbol{d}|}{\sqrt{(\boldsymbol{a}_1+\boldsymbol{a}_3-\boldsymbol{d})\cdot(\boldsymbol{a}_1+\boldsymbol{a}_3-\boldsymbol{d})}}\right). \tag{3.12}$$

First, we described the matrix elements of the H_{11} Hamiltonian (8×8 matrix) using these adjustable parameters and direction cosines; the bases of H_{11} are $|s1,\uparrow\rangle, |s1,\downarrow\rangle, |p_x1,\uparrow\rangle, |p_y1,\uparrow\rangle, |p_z1,\uparrow\rangle, |p_x1,\downarrow\rangle, |p_y1,\downarrow\rangle$ and $|p_z1,\downarrow\rangle$.

TABLE 3.5: The matrix element of H^{ss}.

	$\lvert s1,\uparrow\rangle$	$\lvert s1,\downarrow\rangle$
$\langle s1,\uparrow\rvert$	$E_s + V''_{ss\sigma}\mathrm{g}_{26}$	0
$\langle s1,\downarrow\rvert$	0	$E_s + V''_{ss\sigma}\mathrm{g}_{26}$

TABLE 3.6: The matrix element of $H^{sp}_{\uparrow\uparrow}$.

	$\lvert p_x1,\uparrow\rangle$	$\lvert p_y1,\uparrow\rangle$	$\lvert p_z1,\uparrow\rangle$
$\langle s1,\uparrow\rvert$	$V''_{sp\sigma}\mathrm{g}_{27}$	$V''_{sp\sigma}\mathrm{g}_{28}$	0

TABLE 3.7: The matrix element of $H^{pp}_{\uparrow\uparrow}$.

	$\lvert p_x1,\uparrow\rangle$	$\lvert p_y1,\uparrow\rangle$	$\lvert p_z1,\uparrow\rangle$
$\langle p_x1,\uparrow\rvert$	$E_p + V''_{pp\sigma}\mathrm{g}_{29} + V''_{pp\pi}\mathrm{g}_{30}$	$-i\lambda/3 + (V''_{pp\sigma} - V''_{pp\pi})\mathrm{g}_{31}$	0
$\langle p_y1,\uparrow\rvert$		$E_p + V''_{pp\sigma}\mathrm{g}_{30} + V''_{pp\pi}\mathrm{g}_{29}$	0
$\langle p_z1,\uparrow\rvert$	h.c.		$E_p + V''_{pp\pi}\mathrm{g}_{26}$

TABLE 3.8: The matrix element of $H^{pp}_{\downarrow\downarrow}$.

	$\lvert p_x1,\downarrow\rangle$	$\lvert p_y1,\uparrow\rangle$	$\lvert p_z1,\downarrow\rangle$
$\langle p_x1,\downarrow\rvert$	$E_p + V''_{pp\sigma}\mathrm{g}_{29} + V''_{pp\pi}\mathrm{g}_{30}$	$i\lambda/3 + (V''_{pp\sigma} - V''_{pp\pi})\mathrm{g}_{31}$	0
$\langle p_y1,\downarrow\rvert$		$E_p + V''_{pp\sigma}\mathrm{g}_{30} + V''_{pp\pi}\mathrm{g}_{29}$	0
$\langle p_z1,\downarrow\rvert$	h.c.		$E_p + V''_{pp\pi}\mathrm{g}_{26}$

TABLE 3.9: The matrix element of $H^{pp}_{\uparrow\downarrow}$.

	$\|p_x1,\downarrow\rangle$	$\|p_y1,\downarrow\rangle$	$\|p_z1,\downarrow\rangle$
$\langle p_x1,\uparrow\|$	0	0	$i\lambda/3$
$\langle p_y1,\uparrow\|$	0	0	$-i\lambda/3$
$\langle p_z1,\uparrow\|$	$-i\lambda/3$	$i\lambda/3$	0

$$H_{11} = \begin{pmatrix} H^{ss} & H^{sp} & \mathbf{0} \\ & \mathbf{0} & H^{sp} \\ (H^{sp})^\dagger \quad \mathbf{0} & H^{pp}_{\uparrow\uparrow} & H^{pp}_{\uparrow\downarrow} \\ \mathbf{0} \quad (H^{sp})^\dagger & \left(H^{pp}_{\uparrow\downarrow}\right)^\dagger & H^{pp}_{\downarrow\downarrow} \end{pmatrix} \tag{3.13}$$

Next, we described the H_{12} Hamiltonian (8×8 matrix); H_{12} takes into account inter-plane and intra-plane hopping (hopping from atom 1 to atom 2).

TABLE 3.10: The matrix element of H^{ss}_{12}.

	$\|s2,\uparrow\rangle$	$\|s2,\downarrow\rangle$
$\langle s1,\uparrow\|$	$V_{ss\sigma}\mathrm{g}_0 + V'_{ss\sigma}\mathrm{g}_{13}$	0
$\langle s1,\downarrow\|$	0	$V_{ss\sigma}\mathrm{g}_0 + V'_{ss\sigma}\mathrm{g}_{13}$

TABLE 3.11: The matrix element of H^{sp}_{12}.

	$\|p_x2,\uparrow\rangle$	$\|p_y2,\uparrow\rangle$	$\|p_z2,\uparrow\rangle$
$\langle s1,\uparrow\|$	$V_{sp\sigma}\mathrm{g}_1 + V'_{sp\sigma}\mathrm{g}_{14}$	$V_{sp\sigma}\mathrm{g}_2 + V'_{sp\sigma}\mathrm{g}_{15}$	$V_{sp\sigma}\mathrm{g}_3 + V'_{sp\sigma}\mathrm{g}_{16}$

TABLE 3.12: The matrix element of H^{pp}_{12}.

	$\|p_x2,\uparrow\rangle$	$\|p_y2,\uparrow\rangle$	$\|p_z2,\uparrow\rangle$
$\langle p_x1,\uparrow\|$	$V_{pp\sigma}\mathrm{g}_4 + V_{pp\pi}\mathrm{g}_5$	$(V_{pp\sigma} - V_{pp\pi})\mathrm{g}_{12}$	$(V_{pp\sigma} - V_{pp\pi})\mathrm{g}_6$
	$+V'_{pp\sigma}\mathrm{g}_{17} + V'_{pp\pi}\mathrm{g}_{18}$	$+(V'_{pp\sigma} - V'_{pp\pi})\mathrm{g}_{25}$	$+(V'_{pp\sigma} - V'_{pp\pi})\mathrm{g}_{19}$
$\langle p_y1,\uparrow\|$	$(V_{pp\sigma} - V_{pp\pi})\mathrm{g}_{12}$	$V_{pp\sigma}\mathrm{g}_7 + V_{pp\pi}\mathrm{g}_8$	$(V_{pp\sigma} - V_{pp\pi})\mathrm{g}_{11}$
	$+(V'_{pp\sigma} - V'_{pp\pi})\mathrm{g}_{25}$	$+V'_{pp\sigma}\mathrm{g}_{20} + V'_{pp\pi}\mathrm{g}_{21}$	$+(V'_{pp\sigma} - V'_{pp\pi})\mathrm{g}_{24}$
$\langle p_z1,\uparrow\|$	$(V_{pp\sigma} - V_{pp\pi})\mathrm{g}_6$	$(V_{pp\sigma} - V_{pp\pi})\mathrm{g}_{11}$	$V_{pp\sigma}\mathrm{g}_9 + V_{pp\pi}\mathrm{g}_{10}$
	$+(V'_{pp\sigma} - V'_{pp\pi})\mathrm{g}_{19}$	$+(V'_{pp\sigma} - V'_{pp\pi})\mathrm{g}_{24}$	$+V'_{pp\sigma}\mathrm{g}_{22} + V'_{pp\pi}\mathrm{g}_{23}$

$$H_{12} = \begin{pmatrix} H_{12}^{ss} & H_{12}^{sp} & \mathbf{0} \\ & \mathbf{0} & H_{12}^{sp} \\ -(H_{12}^{sp})^T \quad \mathbf{0} & H_{12}^{pp} & \mathbf{0} \\ \mathbf{0} \quad -(H_{12}^{sp})^T & \mathbf{0} & H_{12}^{pp} \end{pmatrix} \tag{3.14}$$

Using the Hamiltonians H_{11} and H_{12}, the bulk Hamiltonian (16×16 matrix) is expressed as follows

$$H = \begin{pmatrix} H_{11} & H_{12} \\ H_{21} & H_{22} \end{pmatrix} \tag{3.15}$$

where the matrices are $H_{11} = H_{22}$ and $H_{21} = H_{12}^{\dagger}$. The band structure of bulk Bi obtained using the Liu-Allen model is shown here.

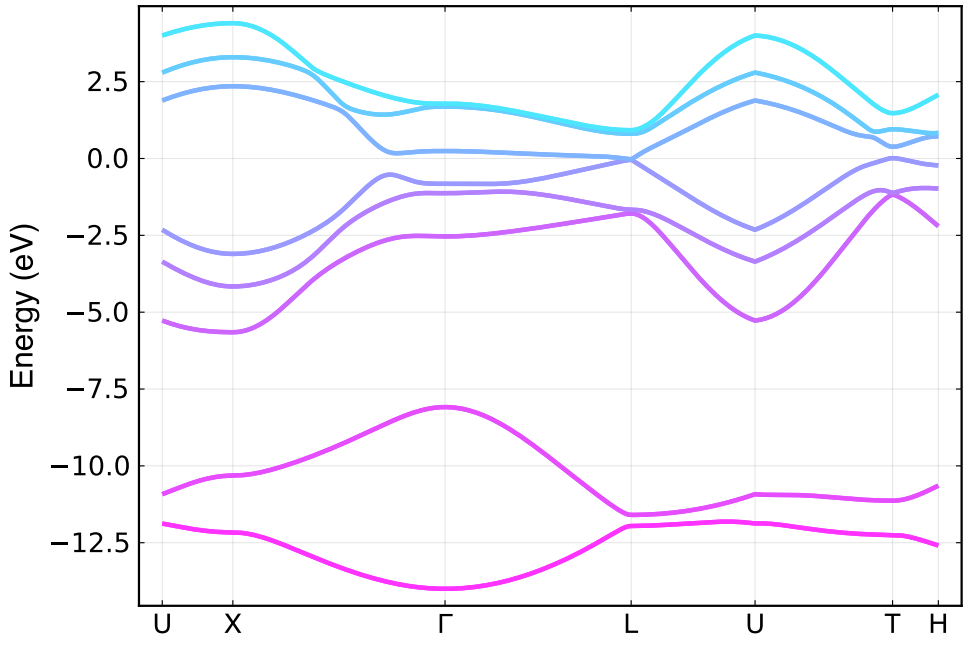

FIGURE 3.1
Band structure of bismuth crystal calculated by the tight binding model[20].

The expressions for g_0-g_{12}, g_{13}-g_{25}

$$
\begin{aligned}
g_0 &= e^{i\boldsymbol{k}\cdot(\boldsymbol{a}_1-\boldsymbol{d})} + e^{i\boldsymbol{k}\cdot(\boldsymbol{a}_2-\boldsymbol{d})} + e^{i\boldsymbol{k}\cdot(\boldsymbol{a}_3-\boldsymbol{d})} \\
g_1 &= \left(e^{i\boldsymbol{k}\cdot(\boldsymbol{a}_2-\boldsymbol{d})} - e^{i\boldsymbol{k}\cdot(\boldsymbol{a}_1-\boldsymbol{d})}\right)\cos\left(\alpha_{1st}\right) \\
g_2 &= \left(e^{i\boldsymbol{k}\cdot(\boldsymbol{a}_1-\boldsymbol{d})} + e^{i\boldsymbol{k}\cdot(\boldsymbol{a}_2-\boldsymbol{d})} - 2e^{i\boldsymbol{k}\cdot(\boldsymbol{a}_3-\boldsymbol{d})}\right)\cos\left(\beta_{1st}\right) \\
g_3 &= g_0\cos\left(\gamma_{1st}\right) \\
g_4 &= \left(e^{i\boldsymbol{k}\cdot(\boldsymbol{a}_1-\boldsymbol{d})} + e^{i\boldsymbol{k}\cdot(\boldsymbol{a}_2-\boldsymbol{d})}\right)\cos^2\left(\alpha_{1st}\right) \\
g_5 &= g_0 - g_4 \\
g_6 &= g_1\cos\left(\gamma_{1st}\right) \\
g_7 &= \left(e^{i\boldsymbol{k}\cdot(\boldsymbol{a}_1-\boldsymbol{d})} + e^{i\boldsymbol{k}\cdot(\boldsymbol{a}_2-\boldsymbol{d})} + 4e^{i\boldsymbol{k}\cdot(\boldsymbol{a}_3-\boldsymbol{d})}\right)\cos^2\left(\beta_{1st}\right) \\
g_8 &= g_0 - g_7 \\
g_9 &= g_0\cos^2\left(\gamma_{1st}\right) \\
g_{10} &= g_0\sin^2\left(\gamma_{1st}\right) \\
g_{11} &= g_2\cos\left(\gamma_{1st}\right) \\
g_{12} &= g_1\cos\left(\beta_{1st}\right)
\end{aligned}
$$

$$
\begin{aligned}
g_{13} &= e^{i\boldsymbol{k}\cdot(\boldsymbol{a}_2+\boldsymbol{a}_3-\boldsymbol{d})} + e^{i\boldsymbol{k}\cdot(\boldsymbol{a}_1+\boldsymbol{a}_3-\boldsymbol{d})} + e^{i\boldsymbol{k}\cdot(\boldsymbol{a}_1+\boldsymbol{a}_2-\boldsymbol{d})} \\
g_{14} &= \left(e^{i\boldsymbol{k}\cdot(\boldsymbol{a}_1+\boldsymbol{a}_3-\boldsymbol{d})} - e^{i\boldsymbol{k}\cdot(\boldsymbol{a}_2+\boldsymbol{a}_3-\boldsymbol{d})}\right)\cos\left(\alpha_{2nd}\right) \\
g_{15} &= \left(e^{i\boldsymbol{k}\cdot(\boldsymbol{a}_2+\boldsymbol{a}_3-\boldsymbol{d})} + e^{i\boldsymbol{k}\cdot(\boldsymbol{a}_1+\boldsymbol{a}_3-\boldsymbol{d})} - 2e^{i\boldsymbol{k}\cdot(\boldsymbol{a}_1+\boldsymbol{a}_2-\boldsymbol{d})}\right)\cos\left(\beta_{2nd}\right) \\
g_{16} &= g_{13}\cos\left(\gamma_{2nd}\right) \\
g_{17} &= \left(e^{i\boldsymbol{k}\cdot(\boldsymbol{a}_2+\boldsymbol{a}_3-\boldsymbol{d})} + e^{i\boldsymbol{k}\cdot(\boldsymbol{a}_1+\boldsymbol{a}_3-\boldsymbol{d})}\right)\cos^2\left(\alpha_{2nd}\right) \\
g_{18} &= g_{13} - g_{17} \\
g_{19} &= g_{14}\cos\left(\gamma_{2nd}\right) \\
g_{20} &= \left(e^{i\boldsymbol{k}\cdot(\boldsymbol{a}_2+\boldsymbol{a}_3-\boldsymbol{d})} + e^{i\boldsymbol{k}\cdot(\boldsymbol{a}_1+\boldsymbol{a}_3-\boldsymbol{d})} + 4e^{i\boldsymbol{k}\cdot(\boldsymbol{a}_1+\boldsymbol{a}_2-\boldsymbol{d})}\right)\cos^2\left(\beta_{2nd}\right) \\
g_{21} &= g_{13} - g_{20} \\
g_{22} &= g_{13}\cos^2\left(\gamma_{2nd}\right) \\
g_{23} &= g_{13}\sin^2\left(\gamma_{2nd}\right) \\
g_{24} &= g_{15}\cos\left(\gamma_{2nd}\right) \\
g_{25} &= g_{14}\cos\left(\beta_{2nd}\right)
\end{aligned}
$$

The expressions for g_{26}-g_{31}

$$
\begin{aligned}
g_{26} =& e^{i\boldsymbol{k}\cdot(\boldsymbol{a}_1-\boldsymbol{a}_2)} + e^{i\boldsymbol{k}\cdot(\boldsymbol{a}_2-\boldsymbol{a}_1)} + e^{i\boldsymbol{k}\cdot(\boldsymbol{a}_2-\boldsymbol{a}_3)} \\
&+ e^{i\boldsymbol{k}\cdot(\boldsymbol{a}_3-\boldsymbol{a}_2)} + e^{i\boldsymbol{k}\cdot(\boldsymbol{a}_1-\boldsymbol{a}_3)} + e^{i\boldsymbol{k}\cdot(\boldsymbol{a}_3-\boldsymbol{a}_1)} \\
g_{27} =& \left(e^{i\boldsymbol{k}\cdot(\boldsymbol{a}_2-\boldsymbol{a}_1)} - e^{i\boldsymbol{k}\cdot(\boldsymbol{a}_1-\boldsymbol{a}_2)}\right) \\
&+ \frac{1}{2}\left(e^{i\boldsymbol{k}\cdot(\boldsymbol{a}_2-\boldsymbol{a}_3)} - e^{i\boldsymbol{k}\cdot(\boldsymbol{a}_3-\boldsymbol{a}_2)}\right) \\
&+ \frac{1}{2}\left(e^{i\boldsymbol{k}\cdot(\boldsymbol{a}_3-\boldsymbol{a}_1)} - e^{i\boldsymbol{k}\cdot(\boldsymbol{a}_1-\boldsymbol{a}_3)}\right) \\
g_{28} =& \frac{\sqrt{3}}{2}\left(e^{i\boldsymbol{k}\cdot(\boldsymbol{a}_3-\boldsymbol{a}_1)} - e^{i\boldsymbol{k}\cdot(\boldsymbol{a}_1-\boldsymbol{a}_3)}\right) \\
&+ \frac{\sqrt{3}}{2}\left(e^{i\boldsymbol{k}\cdot(\boldsymbol{a}_3-\boldsymbol{a}_2)} - e^{i\boldsymbol{k}\cdot(\boldsymbol{a}_2-\boldsymbol{a}_3)}\right) \\
g_{29} =& \frac{1}{4}\left(e^{i\boldsymbol{k}\cdot(\boldsymbol{a}_1-\boldsymbol{a}_3)} + e^{i\boldsymbol{k}\cdot(\boldsymbol{a}_3-\boldsymbol{a}_1)}\right) \\
&+ \frac{1}{4}\left(e^{i\boldsymbol{k}\cdot(\boldsymbol{a}_2-\boldsymbol{a}_3)} + e^{i\boldsymbol{k}\cdot(\boldsymbol{a}_3-\boldsymbol{a}_2)}\right) \\
&+ \left(e^{i\boldsymbol{k}\cdot(\boldsymbol{a}_1-\boldsymbol{a}_2)} + e^{i\boldsymbol{k}\cdot(\boldsymbol{a}_2-\boldsymbol{a}_1)}\right) \\
g_{30} =& \frac{3}{4}\left(e^{i\boldsymbol{k}\cdot(\boldsymbol{a}_1-\boldsymbol{a}_3)} + e^{i\boldsymbol{k}\cdot(\boldsymbol{a}_3-\boldsymbol{a}_1)}\right) \\
&+ \frac{3}{4}\left(e^{i\boldsymbol{k}\cdot(\boldsymbol{a}_2-\boldsymbol{a}_3)} + e^{i\boldsymbol{k}\cdot(\boldsymbol{a}_3-\boldsymbol{a}_2)}\right) \\
g_{31} =& \frac{\sqrt{3}}{4}\left(e^{i\boldsymbol{k}\cdot(\boldsymbol{a}_3-\boldsymbol{a}_1)} + e^{i\boldsymbol{k}\cdot(\boldsymbol{a}_1-\boldsymbol{a}_3)} - e^{i\boldsymbol{k}\cdot(\boldsymbol{a}_3-\boldsymbol{a}_2)} - e^{i\boldsymbol{k}\cdot(\boldsymbol{a}_2-\boldsymbol{a}_3)}\right)
\end{aligned}
$$

The expressions g_0-g_{12} are the direction exponentials for the nearest neighbors, g_{13}-g_{25} for the next nearest neighbors and g_{26}-g_{31} for the 3rd neighbors.

3.1.1 Bi(111) surface

Since we focus on the Bi(111) surface, we extend the Liu-Allen model to construct a Bi bilayer film thickness model in this section. First, we construct a bilayer Bi model using the Hamiltonian H_{12}^{intra}, representing intra-bilayer hopping.

Intra-bilayer Hamiltonian H_{12}^{intra} (8×8 matrix)

We could express H_{12}^{intra} by setting the next nearest neighbor hopping parameters in H_{12} to 0.($V'_{ss\sigma} = V'_{sp\sigma} = V'_{pp\sigma} = V'_{pp\pi} = 0$).

Hamiltonian H_{1BL}

$$
H_{1BL} = \begin{pmatrix} H_{11} & H_{12}^{intra} \\ \left(H_{12}^{intra}\right)^{\dagger} & H_{22} \end{pmatrix} \tag{3.16}
$$

Next, we stack H_{1BL} using H_{12}^{inter}[1], which represents the inter-layer hopping.

[1]The basis of H_{12}^{inter} is $\langle n, B|H_{12}^{inter}|n+1, A\rangle$, where n is the layer number and A or B is the atom in the unit cell.

Inter-bilayer Hamiltonian H_{12}^{inter} (8×8 matrix)

We could express H_{12}^{inter} by setting the nearest neighbor hopping parameters in H_{12} to 0. ($V_{ss\sigma} = V_{sp\sigma} = V_{pp\sigma} = V_{pp\pi} = 0$).

H_{nBL} is then expressed as follows.

$$H_{nBL} = \begin{pmatrix} H_{1BL}^{1st} & H_{12}^{inter} & & & \\ (H_{12}^{inter})^{\dagger} & H_{1BL}^{2nd} & H_{12}^{inter} & & \\ & (H_{12}^{inter})^{\dagger} & H_{1BL}^{3rd} & & \\ & & & \ddots & \\ & & & & H_{1BL}^{nth} \end{pmatrix} \tag{3.17}$$

Using Equation 3.17, we obtained the result in Fig 3.2.

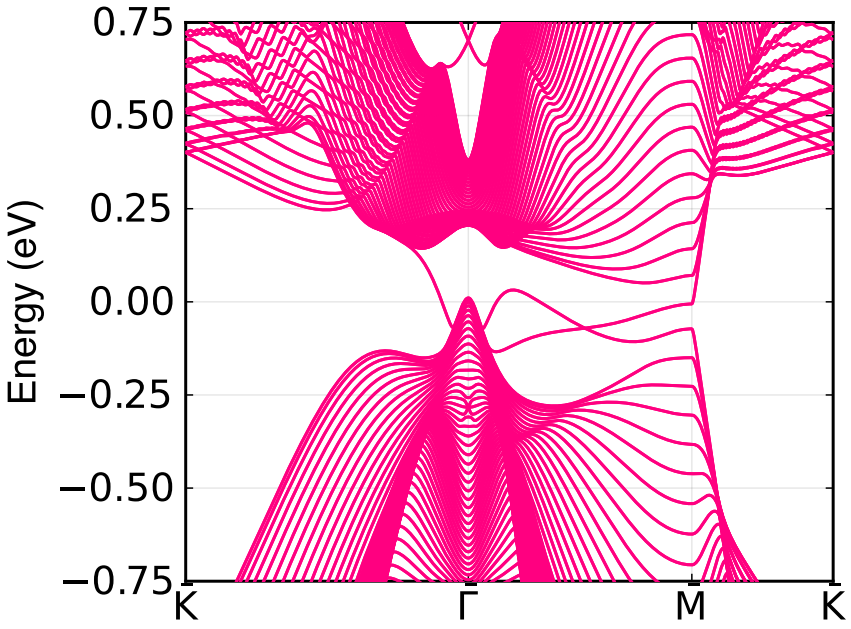

FIGURE 3.2
Band structure of Bi(111) 50BL thick slabs.

However, the results obtained here are not consistent with the experimental results[57, 81–84]. The surface states crossing between $\bar{\Gamma}$ and $\bar{M}$ point. This crossing surface state is physically incorrect. In order to solve this problem, we use the surface potential introduced by Saito et al.[21].

3.1.2 Bi(111) surface potential

A surface potential gradient along the z-axis exists between the surface Bi atoms and the vacuum on the surface BL. This potential gradient caused the surface Rashba effect[85]. These reasons are why the surface conditions using the Liu-Allen model[20] do not match the experimental results. Saito et al. introduced the surface potential to solve this problem[21]. This section explains the surface potential introduced by Saito et al. The surface potential is as follows.

The Bi surface Hamiltonian $H_{11}^{surface}$ (8×8 matrix) considering the surface potential is expressed using the following parameters γ_{sp} and γ_{pp}($\gamma_{sp}=0.45$, $\gamma_{pp}=-0.27$). The parameter between the s and p_z orbitals at the surface is γ_{sp}. The parameter between p_x (or p_y) and p_z orbitals is γ_{pp}. The hopping between orbits is

$$\begin{aligned} t_{s,p_z} &= \gamma_{sp}, \\ t_{p_x,p_z} &= \gamma_{pp}\cos\theta_{ij}, \\ t_{p_y,p_z} &= \gamma_{pp}\sin\theta_{ij}, \end{aligned}$$

where θ_{ij} given is the angle to the p_z orbit. The θ_{ij} given here is expressed as

$$\begin{aligned} \theta_{1,2} = \theta_{2,1} &= \arctan\left(\frac{(\boldsymbol{a}_1-\boldsymbol{a}_2)_{[y]}}{(\boldsymbol{a}_1-\boldsymbol{a}_2)_{[x]}}\right), \\ \theta_{1,3} = \theta_{3,1} &= \arctan\left(\frac{(\boldsymbol{a}_1-\boldsymbol{a}_3)_{[y]}}{(\boldsymbol{a}_1-\boldsymbol{a}_3)_{[x]}}\right), \\ \theta_{2,3} = \theta_{3,2} &= \arctan\left(\frac{(\boldsymbol{a}_3-\boldsymbol{a}_2)_{[y]}}{(\boldsymbol{a}_3-\boldsymbol{a}_2)_{[x]}}\right). \end{aligned}$$

Using θ_{ij}, the matrix elements of the surface Hamiltonian $H_{surface}$ are

$$\langle s,1|H_{11}^{surface}|p_z,1\rangle = \gamma_{sp}\mathrm{g}_{26},$$

$$\begin{aligned} \langle p_x,1|H_{11}^{surface}|p_z,1\rangle = \gamma_{pp}\Big[&\cos\theta_{1,2}\left(e^{i\boldsymbol{k}\cdot(\boldsymbol{a}_1-\boldsymbol{a}_2)}+e^{i\boldsymbol{k}\cdot(\boldsymbol{a}_2-\boldsymbol{a}_1)}\right) \\ &+\cos\theta_{1,3}\left(e^{i\boldsymbol{k}\cdot(\boldsymbol{a}_1-\boldsymbol{a}_3)}+e^{i\boldsymbol{k}\cdot(\boldsymbol{a}_3-\boldsymbol{a}_1)}\right) \\ &+\cos\theta_{2,3}\left(e^{i\boldsymbol{k}\cdot(\boldsymbol{a}_2-\boldsymbol{a}_3)}+e^{i\boldsymbol{k}\cdot(\boldsymbol{a}_3-\boldsymbol{a}_2)}\right)\Big], \end{aligned}$$

$$\begin{aligned} \langle p_y,1|H_{11}^{surface}|p_z,1\rangle = \gamma_{pp}\Big[&\sin\theta_{1,2}\left(e^{i\boldsymbol{k}\cdot(\boldsymbol{a}_1-\boldsymbol{a}_2)}+e^{i\boldsymbol{k}\cdot(\boldsymbol{a}_2-\boldsymbol{a}_1)}\right) \\ &+\sin\theta_{1,3}\left(e^{i\boldsymbol{k}\cdot(\boldsymbol{a}_1-\boldsymbol{a}_3)}+e^{i\boldsymbol{k}\cdot(\boldsymbol{a}_3-\boldsymbol{a}_1)}\right) \\ &+\sin\theta_{2,3}\left(e^{i\boldsymbol{k}\cdot(\boldsymbol{a}_2-\boldsymbol{a}_3)}+e^{i\boldsymbol{k}\cdot(\boldsymbol{a}_3-\boldsymbol{a}_2)}\right)\Big], \end{aligned}$$

Also, $\langle\alpha,1|H_{11}^{surface}|p_z,1\rangle = \langle\alpha,2|H_{11}^{surface}|p_z,2\rangle$ ($\alpha=s,p_x,p_y$). In addition, the bottom surface Hamiltonian $H_{22}^{surface}$ is represented by switching the sign of $\gamma_{sp/pp}$.

Using $H_{11}^{surface}$ and $H_{22}^{surface}$, the surface bilayers are, respectively,

$$H_{1stBL}^{surface} = \begin{pmatrix} H_{11}^{surface} & H_{12}^{intra} \\ \left(H_{12}^{intra}\right)^{\dagger} & H_{22} \end{pmatrix}, \tag{3.18}$$

$$H_{nthBL}^{surface} = \begin{pmatrix} H_{11} & H_{12}^{intra} \\ \left(H_{12}^{intra}\right)^{\dagger} & H_{22}^{surface} \end{pmatrix}. \tag{3.19}$$

Changing H_{1BL}^{1st} and H_{1BL}^{nth} in Equation 3.17 to $H_{1stBL}^{surface}$ and $H_{nthBL}^{surface}$, respectively, we obtain the following results (Fig.3.3).

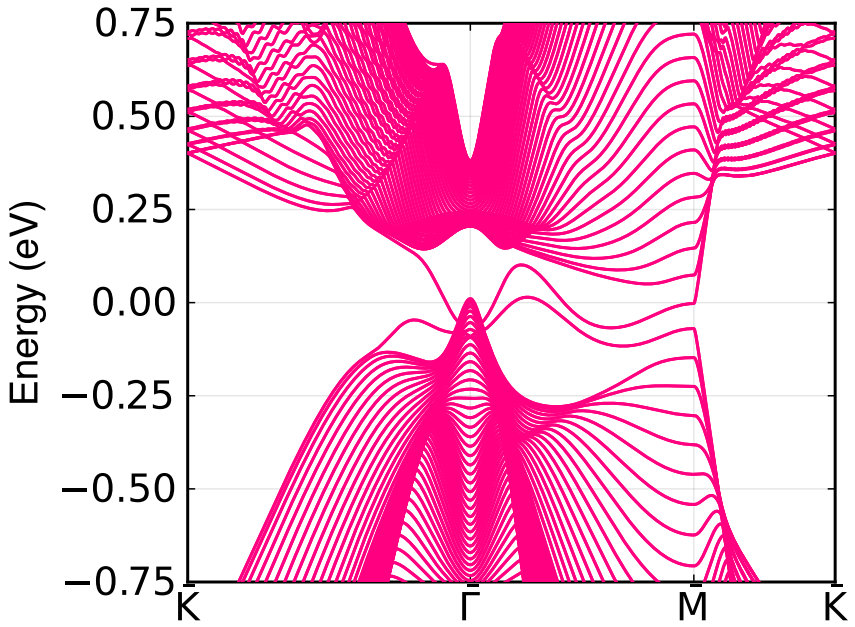

FIGURE 3.3
Band structure of Bi(111) 50BL thick slabs with the surface potential.

The band structure in Fig 3.3 is consistent with the experimental results. Saito et al.'s model allow the surface effects to be correctly confirmed. The model also allows for the investigation of the quantum well states because the film thickness can be easily changed.

3.1.3 Bi/Bi$_{1-x}$Sb$_x$ heterojunction

In this section, we describe a model of a Bi/BiSb heterojunction system. In the Bi/Bi$_{1-x}$Sb$_x$ heterojunction, the Sb content x can be adjusted freely using the virtual-crystal approximation. Therefore, it is possible to observe a continuous sequence of trivial/trivial to trivial/non-trivial heterojunctions. The difference between the lattice constants of Bi and BiSb ($x \leq 0.08$) is so tiny that this study treats the two as equal.

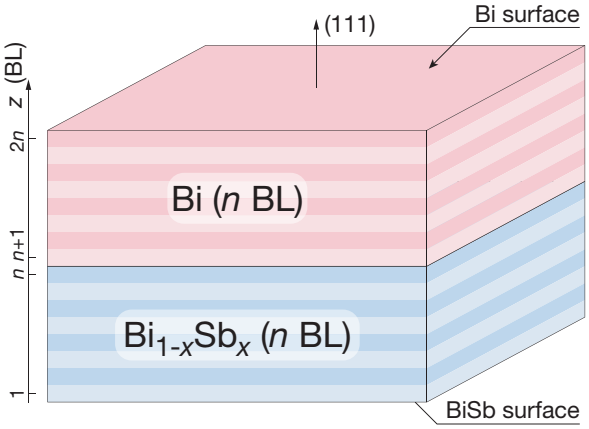

FIGURE 3.4
Schematic of the Bi/BiSb heterojunction (n+n BL).

The Hamiltonian is given by

$$H_{\text{Bi/BiSb}} = \begin{pmatrix} H^{surface}_{\text{Bi1}stBL} & H^{inter}_{\text{Bi12}} & & & \\ \left(H^{inter}_{\text{Bi12}}\right)^{\dagger} & H^{\text{Bi}}_{n-1BL} & H^{inter}_{\text{Bi12}} & & \\ & \left(H^{inter}_{\text{Bi12}}\right)^{\dagger} & H^{\text{BiSb}}_{n-1BL} & H^{inter}_{\text{BiSb12}} & \\ & & \left(H^{inter}_{\text{BiSb12}}\right)^{\dagger} & H^{surface}_{\text{BiSb}nthBL} \end{pmatrix}. \tag{3.20}$$

Fig 3.5 is obtained by numerically diagonalizing equation 3.20.

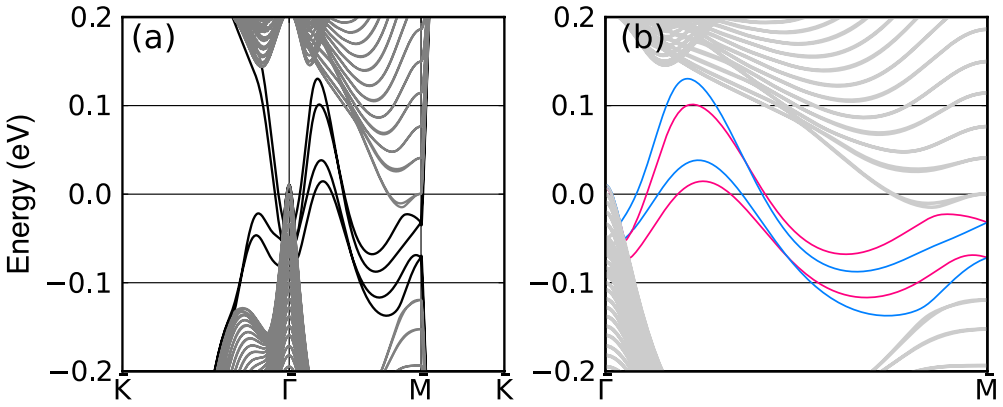

FIGURE 3.5
(a,b) Band structure of Bi/$Bi_{0.92}Sb_{0.08}$ (111) surface (50BL-50BL). The surface states of Bi and BiSb are represented by the red and blue lines, respectively. (a,b) The band structure of Bi/$Bi_{0.92}Sb_{0.08}$ (111) surface (50BL-50BL). The red and blue lines represent the surface states of Bi and BiSb, respectively.

The eigenvalues for the Bi(red line) and BiSb(blue line) surfaces in Fig 3.5(b) are determined from the wave functions and single-particle spectrum introduced in section 3.3 and 3.4.

3.2 Lent model

In this section, we describe the Hamiltonian introduced by Lent, et al.[55]. The parameters of PbTe and SnTe that compose the matrix elements of the Hamiltonian are listed below.

TABLE 3.13: The parameters of PbTe

$E_{s,c}$	= -7.612	$V_{s,s}$	= -0.474
$E_{s,a}$	= -11.002	$V_{s,p}$	= 0.705
$E_{p,c}$	= 3.195	$V_{p,s}$	= 0.633
$E_{p,a}$	= -0.237	$V_{p,p}$	= 2.066
$E_{d,c}$	= 7.73	$V_{p,p\pi}$	= -0.430
$E_{d,a}$	= 7.73	$V_{p,d}$	= -1.29
λ_a	= 1.500	$V_{p,d\pi}$	= 0.835
λ_c	= 0.428	$V_{d,p}$	= -1.59
		$V_{d,p\pi}$	= 0.531
		$V_{d,d}$	= -1.35
		$V_{d,d\delta}$	= 0.668

TABLE 3.14: The parameters of SnTe

$E_{s,c}$	= -6.578	$V_{s,s}$	= -0.510
$E_{s,a}$	= -12.067	$V_{s,p}$	= 0.949
$E_{p,c}$	= 1.659	$V_{p,s}$	= -0.198
$E_{p,a}$	= -0.167	$V_{p,p}$	= 2.218
$E_{d,c}$	= 8.38	$V_{p,p\pi}$	= -0.446
$E_{d,a}$	= 7.73	$V_{p,d}$	= -1.11
λ_a	= 0.592	$V_{p,d\pi}$	= 0.624
λ_c	= 0.594	$V_{d,p}$	= -1.67
		$V_{d,p\pi}$	= 0.766
		$V_{d,d}$	= -1.72
		$V_{d,d\delta}$	= 0.618

Lent Hamiltonian is a 36 × 36 matrix whose basis consists of s, p, and d orbitals.

Basis of 36 × 36 **Hamiltonian**

$$
\begin{aligned}
|s,c,\uparrow\rangle, |s,c,\downarrow\rangle, |s,a,\uparrow\rangle, |s,a,\downarrow\rangle \\
|p_x,c,\uparrow\rangle, |p_y,c,\uparrow\rangle, |p_z,c,\uparrow\rangle \\
|p_x,c,\downarrow\rangle, |p_y,c,\downarrow\rangle, |p_z,c,\downarrow\rangle \\
|p_x,a,\uparrow\rangle, |p_y,a,\uparrow\rangle, |p_z,a,\uparrow\rangle \\
|p_x,a,\downarrow\rangle, |p_y,a,\downarrow\rangle, |p_z,a,\downarrow\rangle \\
|d_1,c,\uparrow\rangle, |d_2,c,\uparrow\rangle, |d_3,c,\uparrow\rangle, |d_4,c,\uparrow\rangle, |d_5,c,\uparrow\rangle \\
|d_1,c,\downarrow\rangle, |d_2,c,\downarrow\rangle, |d_3,c,\downarrow\rangle, |d_4,c,\downarrow\rangle, |d_5,c,\downarrow\rangle \\
|d_1,a,\uparrow\rangle, |d_2,a,\uparrow\rangle, |d_3,a,\uparrow\rangle, |d_4,a,\uparrow\rangle, |d_5,a,\uparrow\rangle \\
|d_1,a,\downarrow\rangle, |d_2,a,\downarrow\rangle, |d_3,a,\downarrow\rangle, |d_4,a,\downarrow\rangle, |d_5,a,\downarrow\rangle
\end{aligned}
$$

The basis of d_1, d_2, d_3, d_4 and d_5 used here are $d_1 = d_{x^2-y^2}$, $d_2 = d_{3z^2-r^2}$, $d_3 = d_{xy}$, $d_4 = d_{yz}$ and $d_5 = d_{zx}$. The Lent Hamiltonian is described in block form as

$$
H = \begin{pmatrix}
H_{s,s} & & & & \\
H_{pc,s} & H_{pc,pc} & & & \\
H_{pa,s} & H_{pa,pc} & H_{pa,pa} & & \\
0 & 0 & H_{dc,pa} & H_{dc,dc} & \\
0 & H_{da,pc} & 0 & H_{da,dc} & H_{da,da}
\end{pmatrix}, \tag{3.21}
$$

where

$$
H_{s,s} = \begin{pmatrix}
E_{s,c} & & & \\
0 & E_{s,c} & & \\
\mathrm{g}_0 V_{ss} & 0 & E_{s,a} & \\
0 & \mathrm{g}_0 V_{s,s} & 0 & E_{s,a}
\end{pmatrix}, \tag{3.22}
$$

$$
H_{pc,s} = \begin{pmatrix} 0 & H_1 \\ 0 & H_2 \end{pmatrix}, \tag{3.23}
$$

$$
H_1 = \begin{pmatrix}
-2\mathrm{g}_1 V_{p,s} & 0 \\
-2\mathrm{g}_2 V_{p,s} & 0 \\
-2\mathrm{g}_3 V_{p,s} & 0
\end{pmatrix}, \tag{3.24}
$$

$$H_2 = \begin{pmatrix} 0 & -2g_1 V_{p,s} \\ 0 & -2g_2 V_{p,s} \\ 0 & -2g_3 V_{p,s} \end{pmatrix}, \tag{3.25}$$

$$H_{pa,s} = \begin{pmatrix} H_3 & 0 \\ H_4 & 0 \end{pmatrix}, \tag{3.26}$$

$$H_3 = \begin{pmatrix} -2g_1 V_{s,p} & 0 \\ -2g_2 V_{s,p} & 0 \\ -2g_3 V_{s,p} & 0 \end{pmatrix}, \tag{3.27}$$

$$H_4 = \begin{pmatrix} 0 & -2g_1 V_{s,p} \\ 0 & -2g_2 V_{s,p} \\ 0 & -2g_3 V_{s,p} \end{pmatrix}, \tag{3.28}$$

$$H_{da,pc} = \begin{pmatrix} H_5 & 0 \\ 0 & H_5 \end{pmatrix}, \tag{3.29}$$

$$H_5 = \begin{pmatrix} -\sqrt{3}g_1 V_{p,d} & \sqrt{3}g_2 V_{p,d} & 0 \\ g_1 V_{p,d} & g_2 V_{p,d} & -2g_3 V_{p,d} \\ -2g_2 V_{p,d\pi} & -2g_1 V_{p,d\pi} & 0 \\ 0 & -2g_3 V_{p,d\pi} & -2g_2 V_{p,d\pi} \\ -2g_3 V_{p,d\pi} & 0 & -2g_1 V_{p,d\pi} \end{pmatrix} \tag{3.30}$$

and

$$H_{da,dc} = \begin{pmatrix} dd1 & dd6 & & & & & & & & \\ dd6 & dd2 & & & & & & & & \\ & & dd3 & & & & & & & \\ & & & dd4 & & & & & & \\ & & & & dd5 & dd6 & & & & \\ & & & & dd6 & dd1 & & & & \\ & & & & & & dd2 & & & \\ & & & & & & & dd3 & & \\ & & & & & & & & dd4 & \\ & & & & & & & & & dd5 \end{pmatrix}. \tag{3.31}$$

The matrix elements used in equation 3.31 are expressed as follows.

$$\begin{aligned} dd1 &= \frac{3}{2}(g_4 + g_5)V_{d,d} + (2g_6 + \frac{g_4}{2} + \frac{g_5}{2})V_{d,d\delta} \\ dd2 &= \frac{3}{2}(g_4 + g_5)V_{d,d\delta} + (2g_6 + \frac{g_4}{2} + \frac{g_5}{2})V_{d,d} \\ dd3 &= 2(g_4 + g_5)V_{d,d\pi} + 2g_6 V_{d,d\delta} \\ dd4 &= 2(g_5 + g_6)V_{d,d\pi} + 2g_4 V_{d,d\delta} \\ dd5 &= 2(g_6 + g_4)V_{d,d\pi} + 2g_5 V_{d,d\delta} \\ dd6 &= \frac{\sqrt{3}}{2}(g_5 \cdot g_4)(V_{dd} - V_{d,d\delta}) \end{aligned}$$

The exponent that determines the direction of hopping is expressed using the lattice constant a as

$$
\begin{aligned}
\mathrm{g}_0 &= \left[e^{ik_x a} + e^{-ik_x a} + e^{ik_y a} + e^{-ik_y a} + e^{ik_z a} + e^{-ik_z a}\right], \\
\mathrm{g}_1 &= \frac{i}{2}\left(e^{ik_x a} - e^{-ik_x a}\right), \\
\mathrm{g}_2 &= \frac{i}{2}\left(e^{ik_y a} - e^{-ik_y a}\right), \\
\mathrm{g}_3 &= \frac{i}{2}\left(e^{ik_z a} - e^{-ik_z a}\right), \\
\mathrm{g}_4 &= \frac{1}{2}\left(e^{ik_x a} + e^{-ik_x a}\right), \\
\mathrm{g}_5 &= \frac{1}{2}\left(e^{ik_y a} + e^{-ik_y a}\right), \\
\mathrm{g}_6 &= \frac{1}{2}\left(e^{ik_z a} + e^{-ik_z a}\right).
\end{aligned}
$$

From the above, the band structure of PbTe and SnTe shown in the Fig 3.6 is obtained.

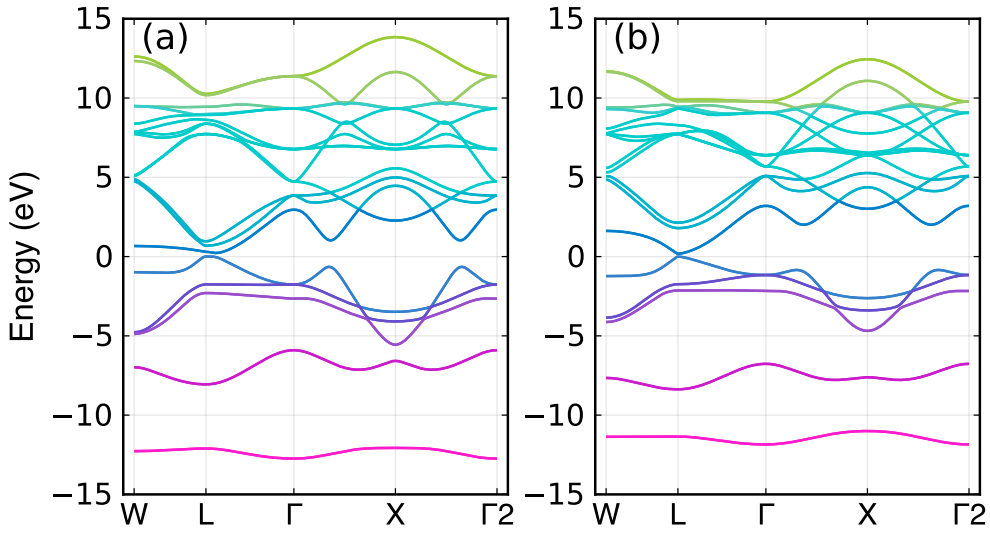

FIGURE 3.6
(a) and (b) are the band structure of PbTe and SnTe, respectively.

3.2.1 PbSnTe(001) surface

Construct the PbSnTe(001) monoatomic layer model. In order to construct the Hamiltonian, we only need to change the directional exponents g_0, g_3, and g_6. The changed direction exponents are

$$
\begin{aligned}
\mathrm{g}_0^{ML} &= \left[e^{ik_x a} + e^{-ik_x a} + e^{ik_y a} + e^{-ik_y a}\right], \\
\mathrm{g}_3^{ML} &= 0, \\
\mathrm{g}_6^{ML} &= 0.
\end{aligned}
$$

The Hamiltonian formed using these exponents is $H^{ML}(36 \times 36$ matrix). In the Hamiltonian $H^{inter}(36 \times 36$ matrix) hopping between monatomic layers, the directional exponents are

$$\begin{aligned}
\mathrm{g}_0^{inter} &= e^{ik_z a}, \\
\mathrm{g}_1^{inter} &= 0, \\
\mathrm{g}_2^{inter} &= 0, \\
\mathrm{g}_3^{inter} &= \frac{i}{2} e^{ik_z a}, \\
\mathrm{g}_4^{inter} &= 0, \\
\mathrm{g}_5^{inter} &= 0, \\
\mathrm{g}_6^{inter} &= \frac{1}{2} e^{ik_z a}.
\end{aligned}$$

Also, no orbital energy enters the hopping Hamiltonian H^{inter}. Therefore, $E_s^{inter} = E_p^{inter} = E_d^{inter} = 0$. The spin-orbit parameter $\lambda_a^{inter} = \lambda_c^{inter} = 0$ because the on-site elements must be cut off as well as the orbital energy. Using H^{ML} and H^{inter}, the n monolayer film is expressed as follows.

$$H_{nML} = \begin{pmatrix}
H_{1st}^{ML} & H^{inter} & & & & \\
(H^{inter})^\dagger & H_{2nd}^{ML} & H^{inter} & & & \\
 & (H^{inter})^\dagger & H_{3rd}^{ML} & H^{inter} & & \\
 & & (H^{inter})^\dagger & & & \\
 & & & & \ddots & \\
 & & & & & H^{inter} \\
 & & & & (H^{inter})^\dagger & H_{nth}^{ML}
\end{pmatrix} \tag{3.32}$$

Using equation 3.32, we recalculated the 280 monolayer thick slabs calculated by Dziawa et al. Figure 3.7 shows the band diagram obtained from the calculation.

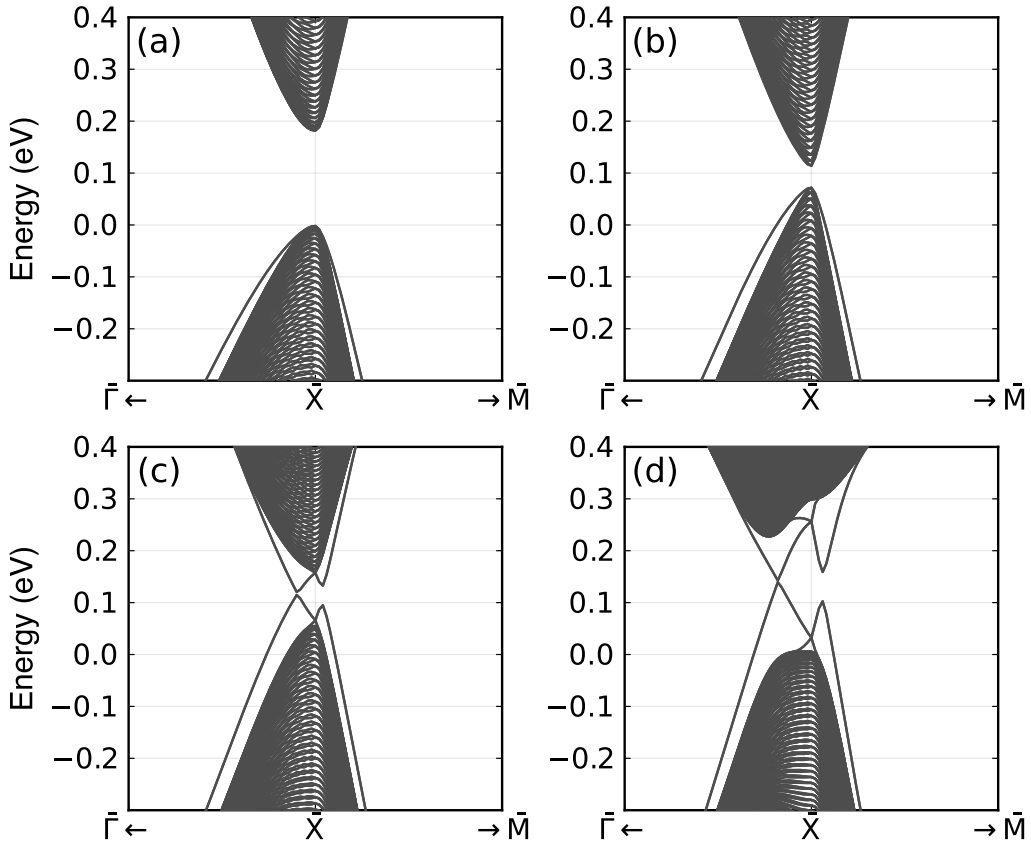

FIGURE 3.7
Band structure of 280-monolayer thick slab of $Pb_{1-x}Sn_xTe$ (001) substitutional alloys with varying Sn content. (a) and (b) are trivial insulator cases, $x = 0.0$ and $x = 0.3$, respectively. (c) and (d) are for topological crystalline insulator case, $x = 0.6$ and $x = 1.0$, respectively.

3.2.2 PbTe/SnTe heterojunction

Next, we described a PbTe/SnTe heterojunction's Hamiltonian using H_{nML} and H^{inter} constructed from the Lent model as follows

$$H_{\text{PbTe/SnTe}} = \begin{pmatrix} H_{nML}^{\text{PbTe}} & H^{inter} \\ (H^{inter})^{\dagger} & H_{nML}^{\text{SnTe}} \end{pmatrix}. \tag{3.33}$$

The model focuses only on topological inversion. Therefore, it does not take into account the deviation of the lattice constants. The band structure obtained using the formula 3.33 is shown in Fig. 3.8.

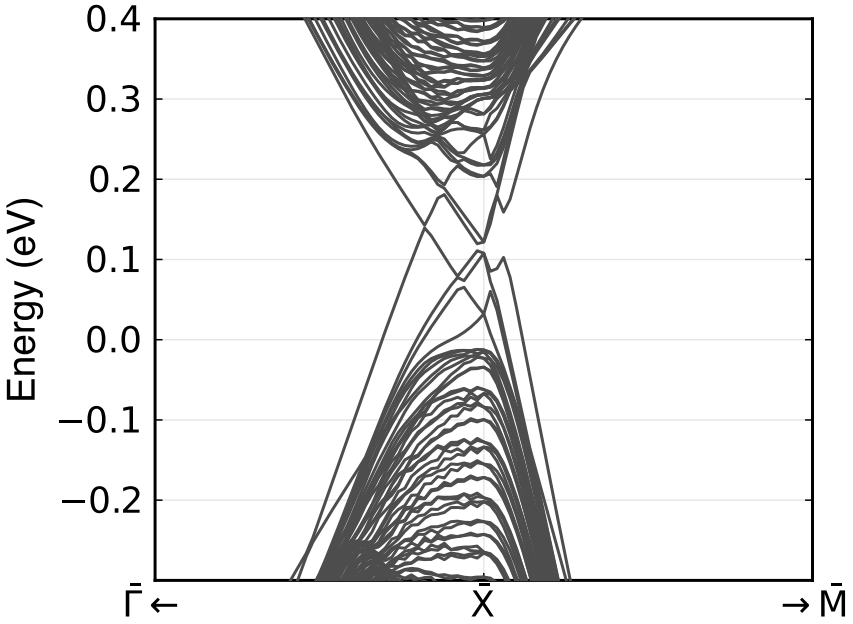

FIGURE 3.8
Band dispersion of PbTe/SnTe heterojunction for 50+50 thick slab.

3.3 Probability distribution $|\psi(k_\parallel, z)|^2$

We compute a probability densities to ascertain the spatial distribution of the eigenfunctions corresponding to the eigenvalues. From the following equation 3.34, use the wave function ψ to obtain $|\psi(k_\parallel, z)|^2$.

$$\mathscr{H}_{N\times N}\psi_N = E_N\psi_N \tag{3.34}$$

In the Bi/BiSb system, the space is ticked every 1BL (16 basis). Therefore, the numerical results satisfy the following equation

$$1 = \int_1^{100} |\psi(k_\parallel, \mathrm{BL})|^2 d\mathrm{BL}. \tag{3.35}$$

Assuming that Bi 100BL is approximately 40nm, $dz = 0.4$ nm. If we used a z-directional variable z, we need a normalization factor A.

$$1 = A\int_0^{40} |\psi(k_\parallel, z)|^2 dz. \tag{3.36}$$

In our calculations, the unit of z is unified to BL to avoid confusion.

3.3.1 Numerical calculation

We used Julia, a programming language suitable for numerical calculations. The Julia package LinearArgebra allows us to use LAPACK. We can obtain the eigenfunctions using the function syev from the LinearArgebra package. This section contains the programming code.

Set parameters

```
function ProbabilityDistribution(rate1,num_layer1,SS)

    a= Bia*rate +Sba*(1-rate1)
    c= Bic*rate +Sbc*(1-rate1)
    b= Bib*rate +Sbb*(1-rate1)
    g= Big*rate +Sbg*(1-rate1)
    μ= Biμ*rate +Sbμ*(1-rate1)

    b1=[-1, -sqrt(3)/3, b]g
    b2=[1, -sqrt(3)/3, b]g
    b3=[0, 2sqrt(3)/3, b]g

    num_sym=4

    G=[0,0,0]
    K=[2/3,1/3,0]
    M=[1/2,0,0]

    sym_p = zeros(Float64,num_sym,3)

    sym_p[1,:]=K[1]*b1+K[2]*b2+K[3]*b3
    sym_p[2,:]=G[1]*b1+G[2]*b2+G[3]*b3
    sym_p[3,:]=M[1]*b1+M[2]*b2+M[3]*b3
    sym_p[4,:]=K[1]*b1+K[2]*b2+K[3]*b3

    num_band=16*(num_layer1)
    num_layer=num_layer1

    len_p = zeros(Float64,num_sym)
    klen = zeros(Int64,num_sym)
    klen[1]=0
    for i = 1:num_sym-1
        len_p[i+1] = sqrt(
        (sym_p[i+1,1]-sym_p[i,1])^2
        +(sym_p[i+1,2]-sym_p[i,2])^2
        +(sym_p[i+1,3]-sym_p[i,3])^2)
        klen[i+1]=Int(floor(len_p[i+1]*100))
    end

    num_kpoint=klen[1]+klen[2]+klen[3]+klen[4]
```

Calculate Probability Distribution ($\bar{\Gamma}$-$\bar{M}$ line)

```
    density=zeros(Float64,num_layer,num_kpoint,21)
    i=1
    for nx = 1:klen[i+1]
        kxin=(
            sym_p[i,1]+nx*(sym_p[i+1,1]-sym_p[i,1])
            /klen[i+1])
        kyin=(
            sym_p[i,2]+nx*(sym_p[i+1,2]-sym_p[i,2])
            /klen[i+1])
        kzin=(
            sym_p[i,3]+nx*(sym_p[i+1,3]-sym_p[i,3])
            /klen[i+1])

        vals, vecs=LAPACK.syev!('V','U',
            Hamiltonian.(kxin,kyin,kzin,rate1,num_layer1))

        for k = SS-10:SS+10
            for j = 1:num_layer
                vector_layer=zeros(ComplexF64,16)
                for basis1 = 1:16
                    vector_layer[basis1]=
                        vecs[16*(j-1)+basis1,k]
                end
                density[j,nx+klen[2],k-SS+11]=abs(
                    dot(vector_layer[:],vector_layer[:]))
            end
            open(@sprintf("PD%02d.csv",k),"w") do file
                Base.print_array(file, density[:,:,k-SS+11])
            end
        end
    end

end
```

3.4 Single-particle spectrum $A(k_\parallel, z, \varepsilon)$

Using the spectral function $A(\boldsymbol{p}, \varepsilon)$[2] [86–88], the retarded Green's function for fermion $G^R(\boldsymbol{p}, \varepsilon)$ becomes

$$G^R(\boldsymbol{p}, \varepsilon) = \int_{-\infty}^{\infty} \frac{1}{2\pi} \frac{A(\boldsymbol{p}, \varepsilon')}{\varepsilon - \varepsilon' + i\delta} d\varepsilon', \tag{3.37}$$

where

$$A(\boldsymbol{p}, \varepsilon) = 2\pi e^{\beta\Omega} \sum_{m,n} |\langle n|\psi_{\boldsymbol{p}}|m\rangle|^2 \left(e^{-\beta E_n} + e^{-\beta E_m}\right) \delta\left(\varepsilon + E_n - E_m\right). \tag{3.38}$$

$\beta = 1/k_B T$ and Ω is thermodynamic potential. The relation between the spectral function and the retarded Green's function is

$$A(\boldsymbol{p}, \varepsilon) = -2\mathrm{Im} G^R(\boldsymbol{p}, \varepsilon). \tag{3.39}$$

The energy-momentum representation of the retarded Green's function for a free particle is

$$G_0^R(\boldsymbol{k}, \varepsilon) = \frac{1}{\varepsilon - \xi(\boldsymbol{k}) + i\delta}, \tag{3.40}$$

And the spectral function $A(\boldsymbol{k}, \varepsilon)$ is written as

$$A(\boldsymbol{k}, \varepsilon) = -\frac{1}{\pi} \mathrm{Im} G_0^R(\boldsymbol{k}, \varepsilon). \tag{3.41}$$

For multi-state system such as a stacking layer structure, the equation 3.40 is not sufficient. In order to consider a multi-state system with n states, we substitute an $n \times n$ matrix[89], i. e., Hamiltonian H instead of ξ. Thus, the retarded Green's function for a multi-state system is written as

$$G(\boldsymbol{k}, \varepsilon) = \left[(\varepsilon + i\delta) I - H(\boldsymbol{k})\right]^{-1}, \tag{3.42}$$

where I is the identity matrix of size n. The retarded Green's function presented here has information for the entire system. Therefore, it is possible to obtain the spatial dependence by dividing the information into layer-by-layer. To confirm the spatial distribution, a matrix trace is taken in the basis of each film. For example, in the case of Bi(111) stacking system, traces are taken in 16 basis:$(s\uparrow\downarrow, p_x\uparrow\downarrow, p_y\uparrow\downarrow, p_z\uparrow\downarrow) \times 2$. From the above, we obtained the single-particle spectrum

$$A(\boldsymbol{k}, z, \varepsilon) = -\frac{1}{\pi} \mathrm{Tr}_{layer} \left[\mathrm{Im}\, G(\boldsymbol{k}, \varepsilon)\right]. \tag{3.43}$$

ARPES experiments can directly observe the angle-resolved photocurrent $J(\boldsymbol{k}, \varepsilon)$. From this observation, the relation between the energies of the electrons and wavenumber in the material can be determined. Using the single-particle spectrum $A(\boldsymbol{k}, \varepsilon)$, the Fermi-Dirac distribution function $f(\varepsilon)$, and the dipole interaction M, we obtain the angle-resolved photocurrent

$$J(\boldsymbol{k}, \varepsilon) = M f(\varepsilon) A(\boldsymbol{k}, \varepsilon). \tag{3.44}$$

[2] Lehmann representation

Here, the observed single-particle spectrum is written by

$$A(\boldsymbol{k}, \varepsilon) = \frac{1}{\pi} \mathrm{Im} \left(\frac{1}{\varepsilon - \epsilon_0(\boldsymbol{k}) + i\Sigma"} \right), \tag{3.45}$$

where ϵ_0 is the bare energy band and $\Sigma"$[3] is lifetime. Based on this understanding, it is more consistent with the realistic system to write the retarded Green's function and the spectral function $A(\boldsymbol{k}_{\|}, z, \varepsilon)$ as follows.

$$A(\boldsymbol{k}_{\|}, z, \varepsilon) = -\frac{1}{\pi} \mathrm{Tr}_{layer} \left[\mathrm{Im}\, G(\boldsymbol{k}_{\|}, \varepsilon) \right], \tag{3.46}$$

$$G(\boldsymbol{k}_{\|}, \varepsilon) = \left[\varepsilon - H(\boldsymbol{k}_{\|}) + i\Sigma'' \right]^{-1}. \tag{3.47}$$

[3]The parameter $\Sigma"$ was set to 0.01.

3.4.1 Numerical calculation

Set parameters

```
function SingleParticleSpectrum(rate1,num_layer1)
    a= Bia*rate +Sba*(1-rate1)
    c= Bic*rate +Sbc*(1-rate1)
    b= Bib*rate +Sbb*(1-rate1)
    g= Big*rate +Sbg*(1-rate1)
    μ= Biμ*rate +Sbμ*(1-rate1)
    b1=[-1, -sqrt(3)/3, b]g
    b2=[1, -sqrt(3)/3, b]g
    b3=[0, 2sqrt(3)/3, b]g
    num_sym=4
    G=[0,0,0]
    K=[2/3,1/3,0]
    M=[1/2,0,0]
    sym_p = zeros(Float64,num_sym,3)
    sym_p[1,:]=K[1]*b1+K[2]*b2+K[3]*b3
    sym_p[2,:]=G[1]*b1+G[2]*b2+G[3]*b3
    sym_p[3,:]=M[1]*b1+M[2]*b2+M[3]*b3
    sym_p[4,:]=K[1]*b1+K[2]*b2+K[3]*b3
    num_band=16*(num_layer1)
    num_layer=num_layer1
    len_p = zeros(Float64,num_sym)
    klen = zeros(Int64,num_sym)
    klen[1]=0
    for i = 1:num_sym-1
        len_p[i+1] = sqrt(
        (sym_p[i+1,1]-sym_p[i,1])^2
        +(sym_p[i+1,2]-sym_p[i,2])^2
        +(sym_p[i+1,3]-sym_p[i,3])^2)
        klen[i+1]=Int(floor(len_p[i+1]*100))
    end
    num_kpoint=klen[1]+klen[2]+klen[3]+klen[4]
```

Calculate single-particle spectrum ($\bar{\Gamma}$-$\bar{\mathrm{M}}$ line)

```
    d_ene=200
    k_mesh=200
    Green=zeros(ComplexF64,num_band,num_band)
    Imatrix=Matrix{ComplexF64}(I, num_band, num_band)
    SPS=zeros(Float64,d_ene+1,k_mesh+1,num_layer1)
    ithGreen=zeros(ComplexF64,16,16)
    tr_ithGreen=zeros(Float64,d_ene+1,k_mesh+1,num_layer1)

    for Ene = 0:d_ene
        energy = -0.2 + i*0.4/d_ene
        i=1
        for nk = 0:k_mesh
            kxin=(sym_p[i,1]+nk*(sym_p[i+1,1]-sym_p[i,1])
                /k_mesh)
            kyin=(sym_p[i,2]+nk*(sym_p[i+1,2]-sym_p[i,2])
                /k_mesh)
            kzin=(sym_p[i,3]+nk*(sym_p[i+1,3]-sym_p[i,3])
                /k_mesh)
            Green = inv(energy*Imatrix+im*0.01*Imatrix
            -Hamiltonian.(kxin,kyin,kzin,rate1,num_layer1))

            for j = 1:num_layer1
                for l = 1:16
                    for m = 1:16
                        ithGreen[l,m]=
                        Green[16*(j-1)+l,16*(j-1)+m]
                    end
                end
                tr_ithGreen[Ene+1,nk+1,j]=tr(imag(ithGreen))

            end
        end
    end
    SPS =-(1/)*tr_ithGreen

    for BL= 1:num_layer1
        open(@sprintf("SPS%02d.csv",BL),"w") do file
            Base.print_array(file, SPS[:,:,BL])
        end
    end

end
```

Chapter 4

Bi/BiSb topological heterojunction

Band alignment, represented by connecting the band of two dissimilar semiconductors (Fig. 4.1 (a)), is mentioned in many textbooks dealing with heterojunctions[1–3]. In the mid-1980s, the possibility of interface state in heterojunctions with inverted bands was proposed[4–9]. Recently, this interface state has been reexamined from the viewpoint of topology[51, 52].

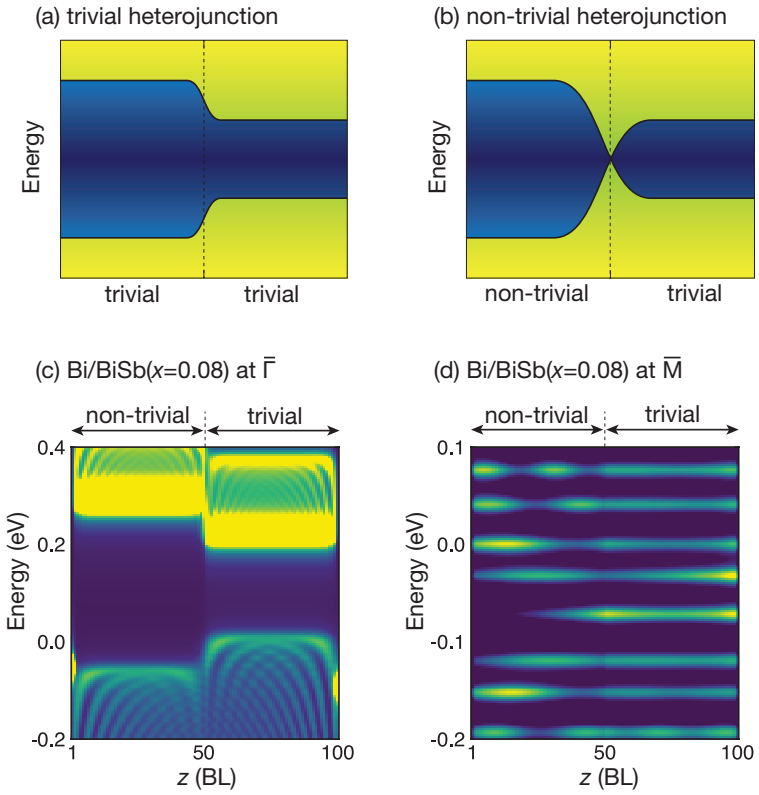

FIGURE 4.1
(a), (b) Schematics of heterojunctions between topologically trivial semiconductors and between trivial and non-trivial semiconductors, respectively. (c), (d) Present results of topological heterojunction $Bi/Bi_{1-x}Sb_x$ ($x = 0.08$) of 50+50 BL at $\bar{\Gamma}$-point and $\bar{M}$-point, respectively.

Topological insulators are one of the major topics in recent condensed matter physics. Materials are divided into two groups: metals and insulators. This classification is based on the presence or absence of electrical conduction. However, topological insulators cannot be classified by both. Topological insulators are characterized by the fact that the bulk is an insulator, and the surface has a metallic conduction state. In order to connect bands of the same symmetry at the junction interface of a topological insulator and a trivial insulator, a gapless conduction state must exist at the interface (Fig. 4.1 (b)). Considering the vacuum as a trivial insulator with a huge bandgap, there is no contradiction in the presence of a gapless conduction state on the surface, which is the interface between the topological insulator and the vacuum.

Fu and Kane proposed in 2007 that BiSb is a three-dimensional topological insulator[17]. In the Liu-Allen model[20], the topology of $Bi_{1-x}Sb_x$ switches from trivial to non-trivial at $x = 0.02$ as the Sb content x increases. In other words, it transitions from a semimetal to a topological insulator. However, some reports suggest pure Bi ($x = 0.00$) is a topological insulator[57, 59, 60]. This opposition to the topology of pure Bi originates from the convenient determination of the topology of BiSb proposed by Fu and Kane[17]. The way of Fu and Kane determines the topology by counting surface Fermi surfaces. However, the bandgap of the BiSb system is extremely small, and it is difficult to measure the "true surface state" with the resolution of the current ARPES experiment (used for direct surface measurement). In addition, it is widely known that the quantum size effect affects surface electrons[46–48]. Topologically protected surface electrons are no exception. In finite-thickness topological insulator films, the quantum size effect opens gaps of topologically protected gapless surface states. This qualitative change in the surface state also makes it difficult to determine the topology of the BiSb system.

The quantum size effect appears more prominently when the Fermi wavelength of the material is long. However, the quantum size effects on band alignment in "topological" heterojunctions consisting of two materials with different topologies has not been extensively investigated. The Fermi wavelength of BiSb is very long, and even with a film thickness of about 100 nm, the top and bottom surfaces interfere with each other[12]. It is considering that the penetration length of the surface wavefunction of topological materials, e.g., Bi_2Se_3, is on the order of a few nanometers[90–92]. In the Bi_2Se_3 system, the region where the quantum size effect can be confirmed is relatively narrow, so it isn't easy to investigate the quantum size effect on the topological heterojunction. On the other hand, in the BiSb system, the penetration length of the wave function is long, and the region where the quantum size effect can be confirmed is wide. Therefore, the Bi/BiSb heterojunctions is suitable for investigating quantum size effects on topological heterojunctions. Moreover, in the Liu-Allen model, the topology of $Bi_{1-x}Sb_x$ is switched only by the parameter Sb content x. Therefore, the Bi/BiSb heterojunction system is an excellent model that can be changed from trivial to non-trivial by a single parameter.

We calculated the Bi(111)/BiSb(111) heterojunction at a finite-thickness based on the Liu-Allen model. As a result, we discovered that the band alignment of the Bi/BiSb heterojunction is a new type that does not belong to any known band alignments (Fig. 4.1 (d)). The band alignment expected for the topological interface state is shown in Fig. 4.1 (b). Since band inversion appears at $\bar{\text{M}}$-point, a topological interface state should appear. However, no band bending occurred appeared in Fig. 4.1 (d). In addition, it was theoretically clarified that one of the two surface state spectra obtained on the Bi surface is not the original surface state of Bi. Due to the strong quantum size effect of the Bi/BiSb heterojunction system, this fake surface

state originated from the bulk wavefunction of the junction material (BiSb) penetrating the Bi surface. This occurs even in heterojunctions with thicknesses as thick as 80 nm, indicating that the wavefunctions penetrate each other through the bonded materials.

In this chapter, we explain the detail of the topological interface state and surface state in the Bi/BiSb heterojunction for finite-thickness.

4.1 Eigenfunctions of surface and interface states

We have calculated the z-dependence of the single-particle spectrum for topological heterojunction in Fig. 4.1; there is a peak structure at the interface. The unexpected band alignment in Fig. 4.1 (d) has a single-particle spectrum $A(\bar{\mathrm{M}}, z, \varepsilon)$ with a peak at the interface ($z = 50$ BL) between the energy range of -0.1 and 0.0 eV. In general, an interface state and a surface state are different. However, in Fig. 4.1 (d), the single-particle spectrum at one eigenvalue peaked at the Bi/BiSb interface and the Bi surface. This peak structure of the single-particle spectrum suggests that one eigenvalue is both for the interface state and the surface state. It is reasonable to assume that the surface influences the topological interface state. Therefore, in order to consider this unexpected interface state, We have investigated the quantum size effects in the Bi/BiSb heterojunctions with 50+50 BL film thickness.

We labeled the four eigenvalues at $\bar{\mathrm{M}}$-point to investigate this novel topological band alignment(Fig. 4.1 (d)). The conduction band minimum (CBM), surface state1 (S1), surface state2 (S2), and valence band maximum (VBM) is shown in Fig. 4.2.

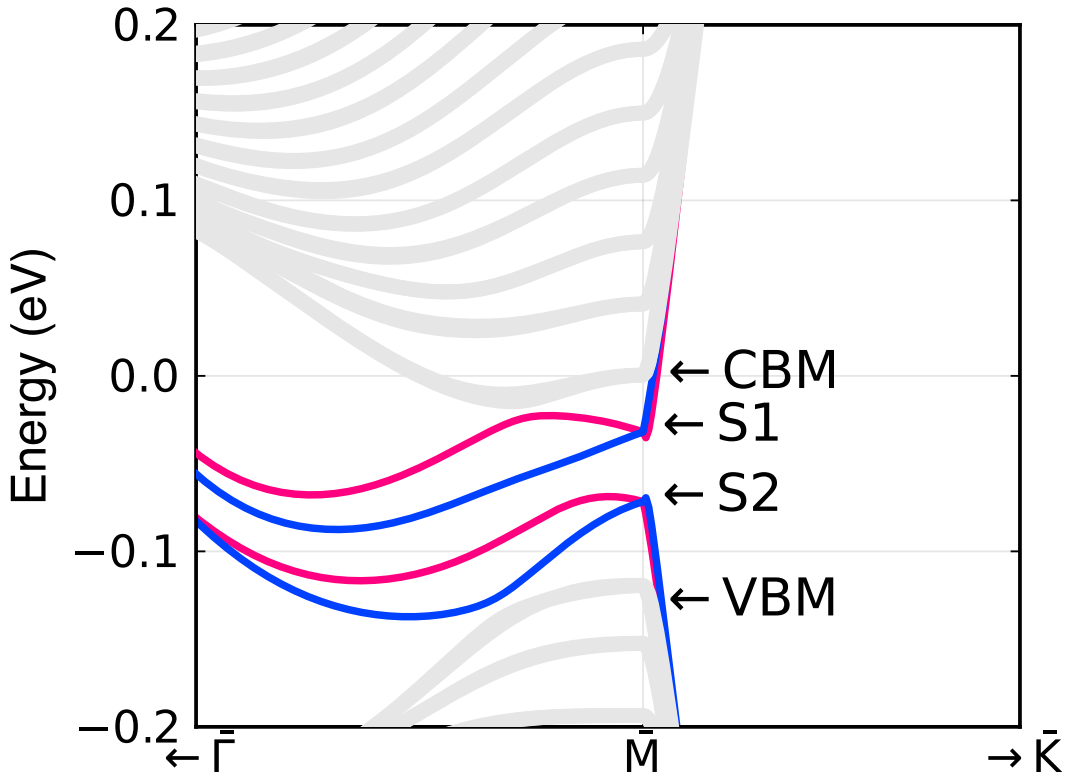

FIGURE 4.2
Band structure of the Bi/$Bi_{0.92}Sb_{0.08}$ heterojunction. The red and blue lines are Bi and BiSb surface bands, respectively. Eigenvalues were labeled from CBM, S1, S2, and VBM at $\bar{\mathrm{M}}$-point

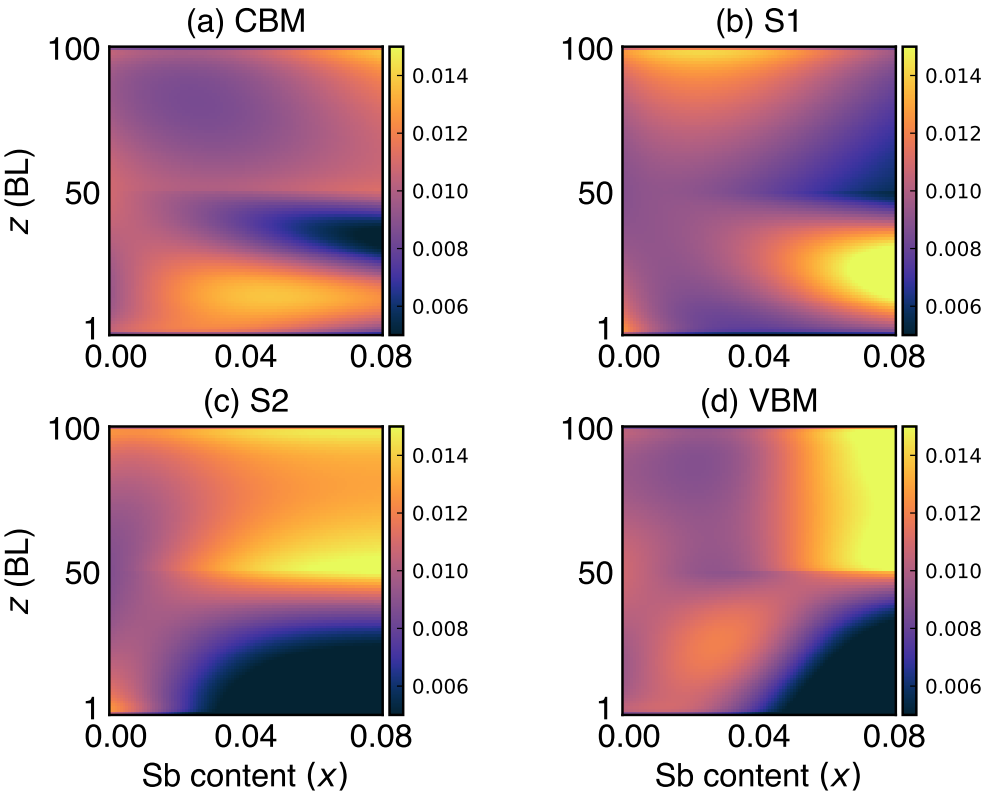

FIGURE 4.3
Sb content x-dependence of the probability distribution $|\psi(z)|^2$ for (a) CBM, (b) S1, (c) S2, and (d) VBM in the Bi/BiSb heterojunction for 50+50 BL thick slab. At the BiSb surface (z = 1 BL) of S1 and S2, the surface state appears for $x \leq x_c (\simeq 0.02)$ but does not for $x > x_c$, indicating a topological transition.

In Figs. 4.2 (a) S1 and (b) S2, the surface states of Bi and BiSb degenerate at the $\bar{\text{M}}$-point. In addition, the curvature of the surface band changes abruptly near the $\bar{\text{M}}$-point, indicating that the surface bands hybridized the bulk band. We obtained more detailed results by calculating the probability distribution shown in Fig. 4.3. Figure 4.3 shows the x-dependence of the probability distribution for (a) CBM, (b) S1, (c) S2, and (d) VBM in the Bi/BiSb heterojunction for 50+50 BL film thickness. The properties of change from trivial ($x \leq 0.02$) to non-trivial ($x \geq 0.02$), though the topological transition is blurry due to the finite thickness. In the trivial/trivial heterojunction case ($x \leq 0.02$), the peaks of $|\psi(z)|^2$ appear on Bi surface ($z = 100$) and BiSb surface ($z = 1$). Therefore, S1 and S2 are surface states. Moreover, there is no $|\psi(z)|^2$ peak at the interface ($z = 50$). In the trivial/non-trivial heterojunction ($x \geq 0.02$), the $|\psi(z)|^2$ peak disappears from the BiSb surface ($z = 1$) of S2 (Fig. 4.3 (c)). Also, the $|\psi(z)|^2$ peak appears approximately at the interface ($z = 50$); S2 is both a Bi surface state and a Bi/BiSb interface state; the BiSb surface state has disappeared. The disappearance of the surface state of BiSb ($x \geq 0.02$) at the $\bar{\text{M}}$-point is entirely consistent with the analytical solution [12]. The result is also reasonable, as an interface state appears between two materials with different topologies. There is an unexpected property that the $|\psi(z)|^2$ peak does not appear at the S1 interface ($z = 50$), shown in Fig. 4.3 (b). Interestingly, the CBM (Fig. 4.3 (a)) has the interface state. The interface peak appears in CBM instead of S1. The peak structure of the interface also exists in the VBM, shown in Fig. 4.3 (d). We have considered that the CBM is the Bi surface and Bi/BiSb interface state. The curvature of the CBM

near the $\bar{\text{M}}$-point appears to be affected by the surface energy band, which may indicate band hybridization. Therefore, the appearance of interface and surface peak structures in the CBM strongly suggests that the CBM, is considered in the bulk state, is not the bulk state. From the probability distribution in Fig. 4.3, the Bi surface state hybridized the BiSb bulk state in CBM and S1 at $x = 0.08$. In addition, the behavior of the Bi side (51 to 100 BL) of the CBM and S2 is similar to the surface state of the free-standing Bi with a 50 BL thick slab. Therefore, the surface state of the free-standing Bi may have the same energy levels as CBM and S2. On the other hand, in VBM, the bulk of Bi and the bulk of BiSb are hybridized. Energy levels cannot exist in the topologically protected BiSb region. Therefore, the probability distribution is localized on the Bi side, forming an interface state.

The information obtained from the Sb content x dependence of the probability distribution is summarized below.

- CBM($x \leq 0.02$):Bulk state(BS)
- S1($x \leq 0.02$):Surface state(SS)
- S2($x \leq 0.02$):SS
- VBM($x \leq 0.02$):BS
- CBM($0.02 \leq x$):Bi SS and Bi/BiSb interface state(IS) and BiSb BS
- S1($0.02 \leq x$):Bi SS and BiSb BS
- S2($0.02 \leq x$):Bi SS and Bi/BiSb IS
- VBM($0.02 \leq x \leq 0.04$):Bi bulk and BiSb bulk
- VBM($0.04 \leq x$: after band hybridization):Bi SS and Bi/BiSb IS

4.2 Thickness dependence of topological interface state

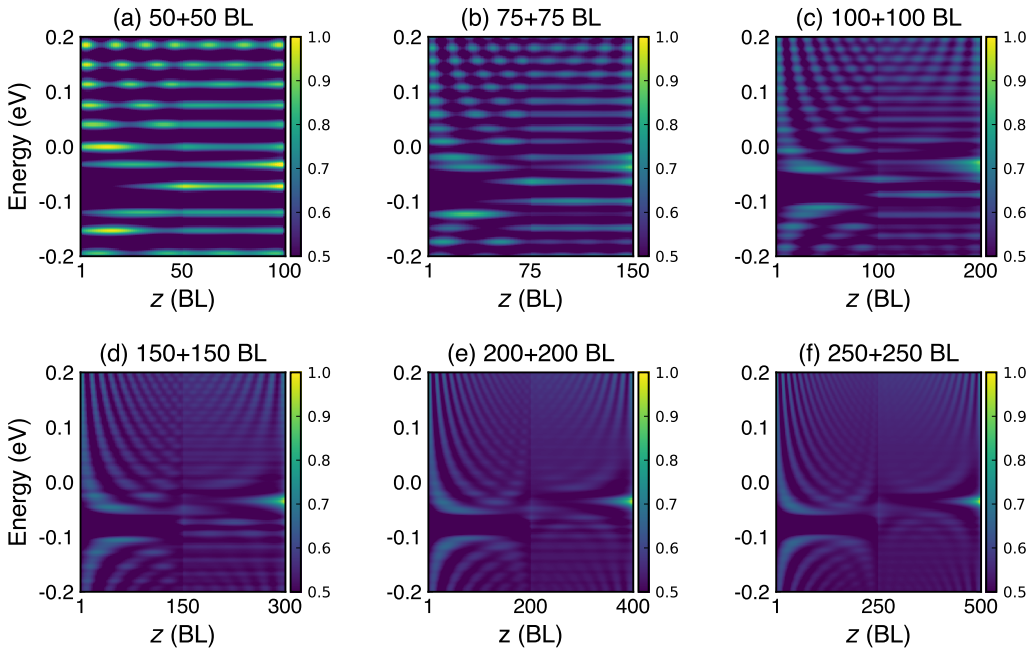

FIGURE 4.4
Single-particle spectrum $A(\bar{\mathrm{M}}, z, \varepsilon)$ from (a) 50+50 BL to (f) 250+250 BL.

We investigated the thickness dependence of the topological interface state. We plot the band alignment at the $\bar{\mathrm{M}}$-point, $A(\bar{\mathrm{M}}, z, \varepsilon)$, for different thickness of $\mathrm{Bi/Bi_{0.92}Sb_{0.08}}$ from 50+50 to 250+250 BL in Fig. 4.4. This result shows that the interface peak structure of the single-particle spectrum at the surface energy band begins to disappear from 150+150 BL. The quantum size effect in the Bi/BiSb heterojunctions disappears in 150+150 BL film thickness. Instead, the interface state appears at an energy level slightly lower than the Bi surface state. This interface peak disappearance is due to the resolution of the hybridization between the interface and surface states. On the other hand, in 50+50 BL film thickness, we could clearly confirmed the Bi surface state and the Bi/BiSb interface state due to the strong quantum size effect.

The quantum size effect appears more prominently when the Fermi wavelength of the material is long. The Fermi wavelength of BiSb is very long, and even with a film thickness of about 100 nm[12], the top and bottom surfaces interfere with each other. Considering that the penetration length of the surface wavefunction of topological materials, e.g. $\mathrm{Bi_2Se_3}$[90, 91], is on the order of few nm. Thus, the long-range wavelength in BiSb is rare. Figure 4.4 indicates that there is a strong surface-interface interference effect.

This strong surface-interface interference effect exists up to a film thickness of about 100+100 BL (40+40 nm) in the Bi/BiSb system. Therefore, in the BiSb system, a considerably thick film is required to confirm the same behavior as general topological materials. In other words, quantum size effects in topological heterojunctions, which cannot be seen in ordinary topological heterojunction, can be seen in the Bi/BiSb heterojunctions.

4.3 Band-bending-like behavior of interface state

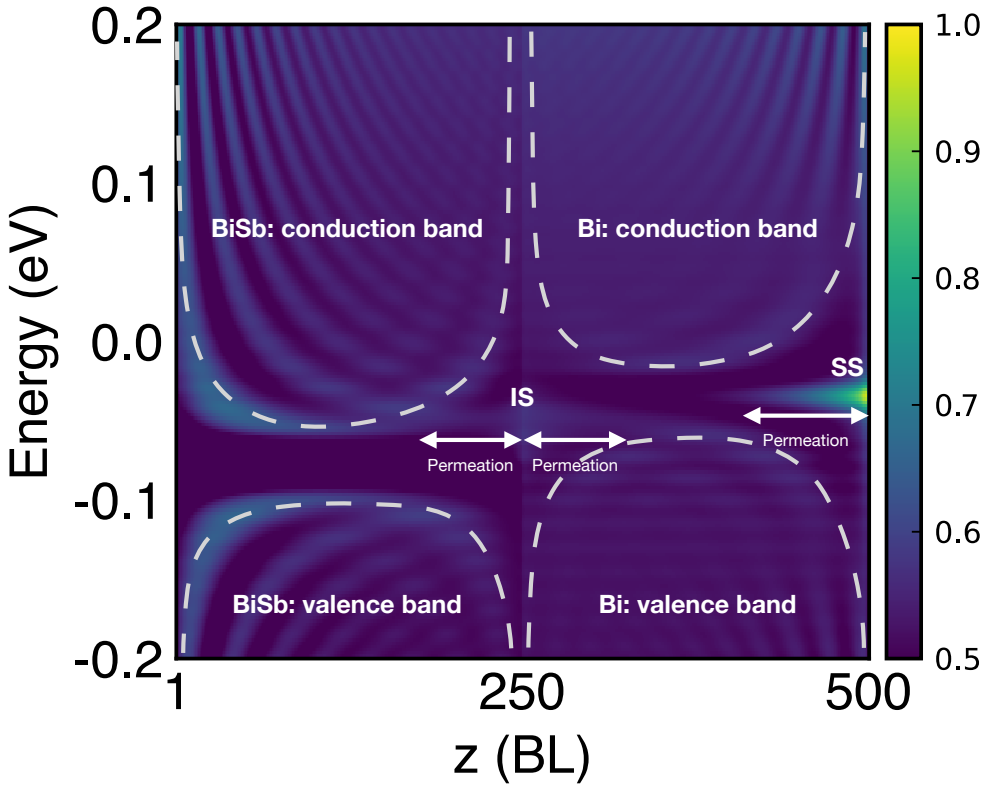

FIGURE 4.5
Band alignment at the $\bar{\mathrm{M}}$-point, $A(\bar{\mathrm{M}}, z, \varepsilon)$, for 250+250 BL. IS ($z = 250$) is the Bi/BiSb interface state, and SS ($z = 500$) is the Bi surface state. The long-range permeation of the interface state and the surface state is 50 to 100 BL (20 to 40 nm).

Above the 150+150 BL film thickness as in Fig. 4.4 (d-f), the expected band-bending-like behavior is visible. The subtle band connection between the conduction band of BiSb and the valence band of Bi in Fig. 4.4 (d-f) (150+150 to 250+250 BL) may represent the band connection expected at a topological heterojunction. If this band-bending were the situation of topological heterojunction as shown in Fig. 4.1 (b), the BiSb valence band would also connect the Bi conduction band, and the band crossing would form. However, no such energy band crossing exists. This band-bending-like behavior is not as expected in Fig 4.1 (b). More importantly, in the case of thin films, such band connections are never observed as shown in Fig. 4.4 (a-c). This band-bending-like behavior can be understood in Fig. 4.5. The interface and surface states in Fig. 4.5 are penetrated by approximately 50 to 100 BL (20 to 40 nm). The interface state has the same energy level as the BiSb conduction band and the Bi valence band. Therefore, the long-range permeation of the interface state in the Bi/BiSb heterojunction forms the band-bending-like behavior expected in Fig 4.1 (b). This band-bending is similar to that expected band alignment in Fig. 4.1 (b), but the formation process is completely different. The Bi/BiSb heterojunction's band alignment predicted in Fig. 4.1(b) cannot be obtained by simply connecting the free-standing Bi and BiSb band alignments.

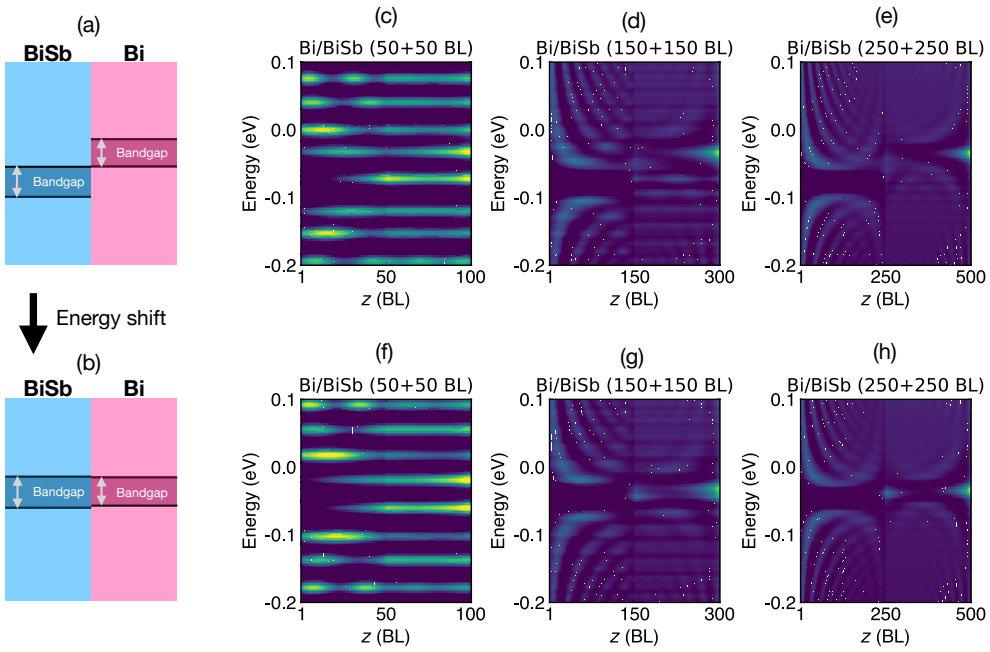

FIGURE 4.6
(a) and (b): Gap position of Bi/BiSb heterojunction. (a) is the original Bi/BiSb heterojunction, and (b) is the modified Bi/BiSb heterojunction in which parameter E_{BiSb} is changed to E_{Bi}. Band alignment of the original Bi/BiSb heterojunction in (c) 50+50 thick slab, (d) 150+150 thick slab, and (e) 250+250 thick slab. And band alignment of the modified Bi/BiSb heterojunction in (f) 50+50 thick slab, (g) 150+150 thick slab, and (h) 250+250 thick slab.

In order to confirm the scenario that the band bending in Fig. 4.5 is caused by the permeation of the interface state that accidentally matches the conduction band of BiSb and the valence band of Bi, we numerically shifted the band gap position[1] and the results are shown in Fig. 4.6. As the film thickness increases, the band alignment of the original Bi/BiSb heterojunction in Fig. 4.6 (d,e) shows a separation of the interface and surface states. Therefore, 150+150BL and 250+250BL are considered to be sufficiently thick. In the sufficiently thick slab in Fig. 4.6 (g,h), there is no band bending. Thus, the scenario that the interface states appear to be connected to other bands only by accident turns out to be correct.

[1]To shift the band gap, we performed the following operations

$$E_p^{\mathrm{BiSb}} = E_p^{\mathrm{BiSb}}, \tag{4.1}$$
$$E_s^{\mathrm{BiSb}} = E_s^{\mathrm{BiSb}}, \tag{4.2}$$

where E_p^{BiSb}, E_p^{BiSb}, E_s^{BiSb}, and E_s^{BiSb} are the Liu-Allen's parameters.

4.4 Interface potential

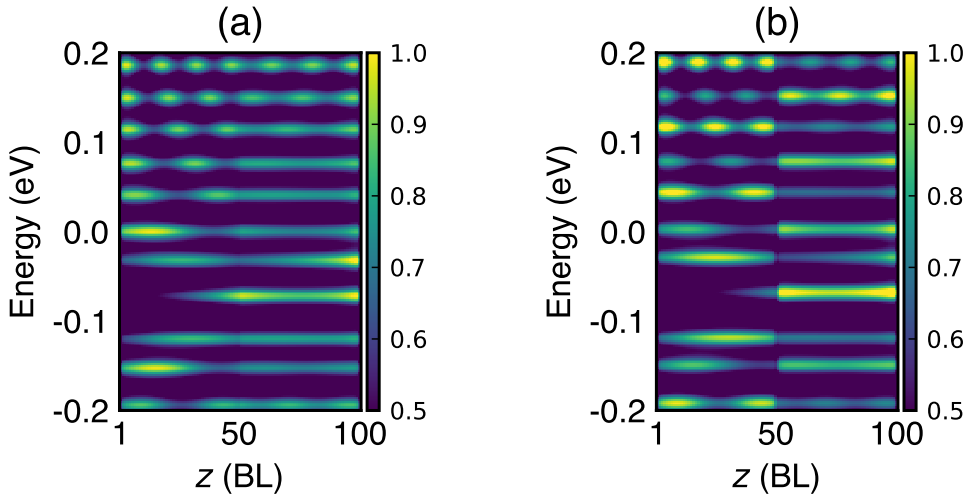

FIGURE 4.7
Band alignment at the $\bar{\mathrm{M}}$-point calculated from $A(\bar{\mathrm{M}}, z, \varepsilon)$ (a) without and (b) with the interface potential.

In general, lattice mismatch at the heterojunction interface causes some effects. However, such lattice mismatch is expected to be small in the Bi/BiSb heterojunctions because the crystal structure and lattice constants almost unchanged for small changes x ($0 < x < 0.08$). Here we check the effect of the interface potential by assuming the same form as the surface potential introduced by Saito et al,. This approximation may overestimate the influence of the interface potential since the surface potential is the potential between the slab and the vacuum.

In Fig. 4.7, we compare the band alignment at the $\bar{\mathrm{M}}$-point for the Bi/BiSb($x = 0.08$) heterojunction in 50+50 BL thick slab with (a) no interface potential and (b) with an interface potential. This comparison shows that an interface potential does not alter long-range permeation. The interface potential does weaken permeation, but as noted earlier, the interface potential in Fig. 4.7 (b) is overestimated relative to the actual interface potential. Therefore, the effect of the interface potential is irrelevant.

4.5 Determination of surface states

We calculated the $Bi/Bi_{1.0}Sb_{0.0}$ heterojunction for 50+50 BL film thickness. The calculation results are shown in Fig 4.8. Here, the thickness of $Bi/Bi_{1.0}Sb_{0.0}$ slab with 50+50BL film is identical to one of the pure Bi 100BL slab. This result is in good agreement with the experimental results[83]: for $Bi/Bi_{1.0}Sb_{0.0}$, both top and bottom surface states are the same, and the surface state is degenerate.

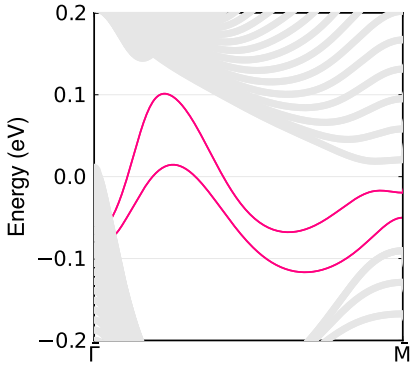

FIGURE 4.8
Band structure of pure-Bi for 100BL thick slab.

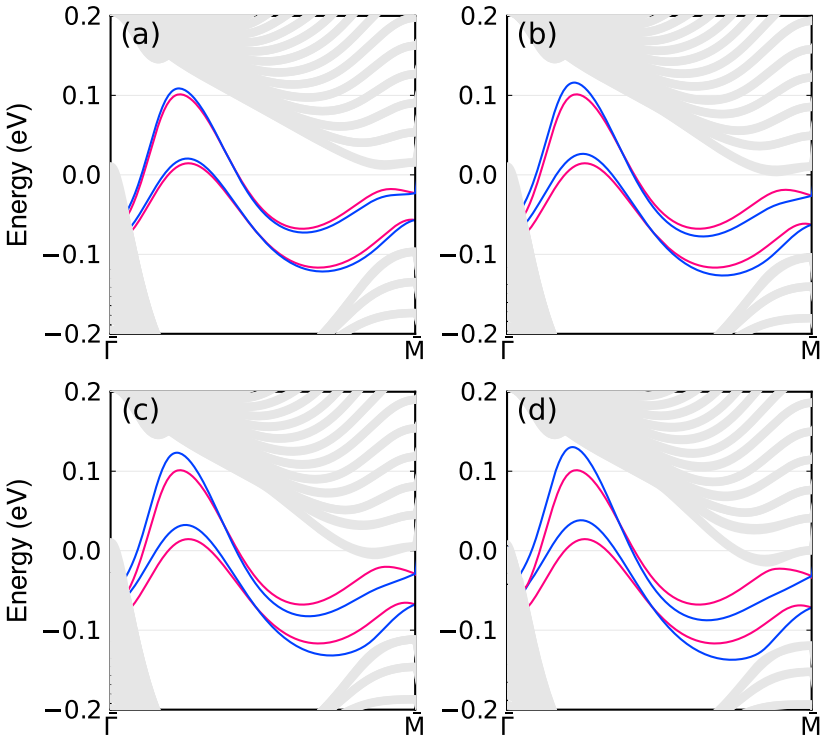

FIGURE 4.9
(a)-(d) are the band structures of the $Bi/Bi_{1-x}Sb_x$ heterojunction for 50+50 BL thick slab. $x = 0.02$, $x = 0.04$, $x = 0.06$, and $x = 0.08$, respectively. The red and blue lines are the Bi and BiSb surface bands. The gray lines are bulk bands.

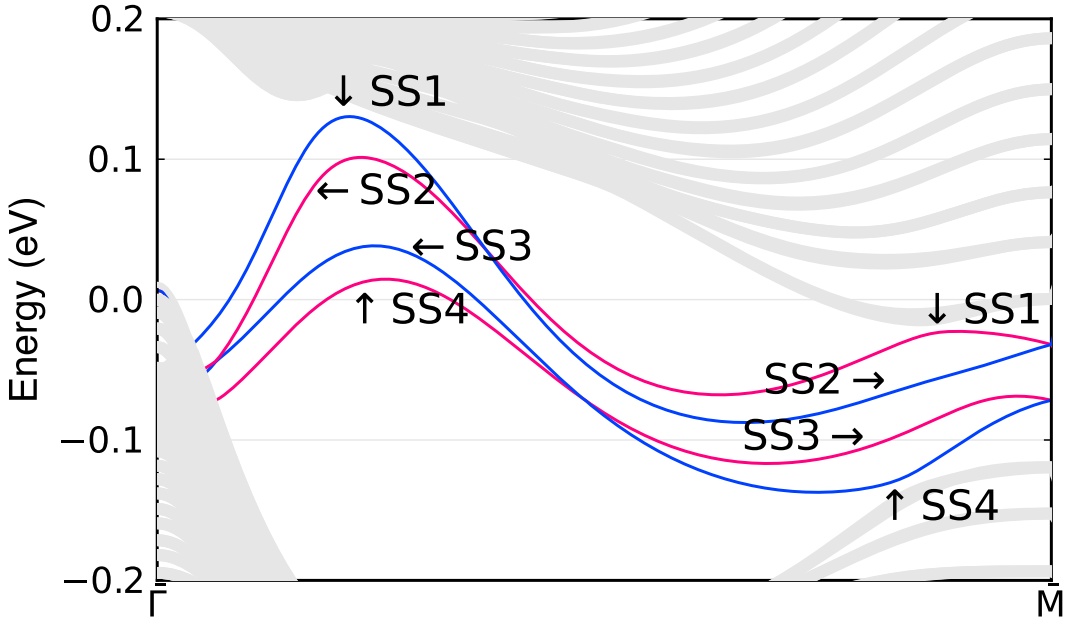

FIGURE 4.10
Band structure of the Bi/$Bi_{0.92}Sb_{0.08}$ heterojunction for 50+50 BL thick slab. Eigenvalues were labeled from SS1 to SS4.

In order to investigate the Sb content x-dependence of the Bi/BiSb heterojunction, we have calculated the energy dispersion, $x = 0.02$, $x = 0.04$, $x = 0.06$, and $x = 0.08$, respectively, in Fig 4.9. With increasing Sb content x, the difference between the red line representing the Bi surface state and the blue line representing the BiSb surface becomes remarkable.

The Bi surface states around $\bar{M}$-point, indicated by the red line, is influenced by the bulk band. The bulk conduction band shows a shift corresponding to an increase in Sb content x. Therefore, the shifted conduction band is the BiSb bulk band. On the other hand, the bulk valence band does not change with increasing Sb content x, so the un-changed valence band is the Bi bulk band. We focus on surface states. The red line of the Bi surface state is not affected by the change of Sb content x near the $\bar{\Gamma}$-point, while the red line shifts near the $\bar{M}$-point. The blue line of the BiSb surface state shows the linkage with Sb content x. From the above, it is possible to infer which eigenvalues correspond to the Bi and BiSb states. On the other hand, there is also a way to determine the eigenvalues strictly by calculation.

By calculating the probability distribution, we confirmed which of the red and blue lines is the Bi surface state or the BiSb surface state. The four eigenvalues considered surface states are labeled SS1, SS2, SS3, and SS4 from top to bottom, as shown in fig 4.10.

The probability distribution $|\psi(k_\parallel, z)|^2$ corresponding to SS1, SS2, SS3, and SS4 are in Fig. 4.11. The $|\psi(k_\parallel, z)|^2$ is normalized by the unit of BL, where $1 = \int_1^{100} |\psi|^2 d\mathrm{BL}$. The peak structure of $|\psi(k_\parallel, z)|^2$ in SS1 appears on the BiSb surface near $\bar{\Gamma}$ point and on the Bi surface near $\bar{M}$-point. For SS2, SS3, and SS4, it is possible to distinguish whether the surface state is Bi or BiSb. At the just $\bar{M}$-point of the probability distribution $|\psi(\bar{M}, z)|^2$, the peak structure of the Bi surface penetrates the inside of the thick slab.

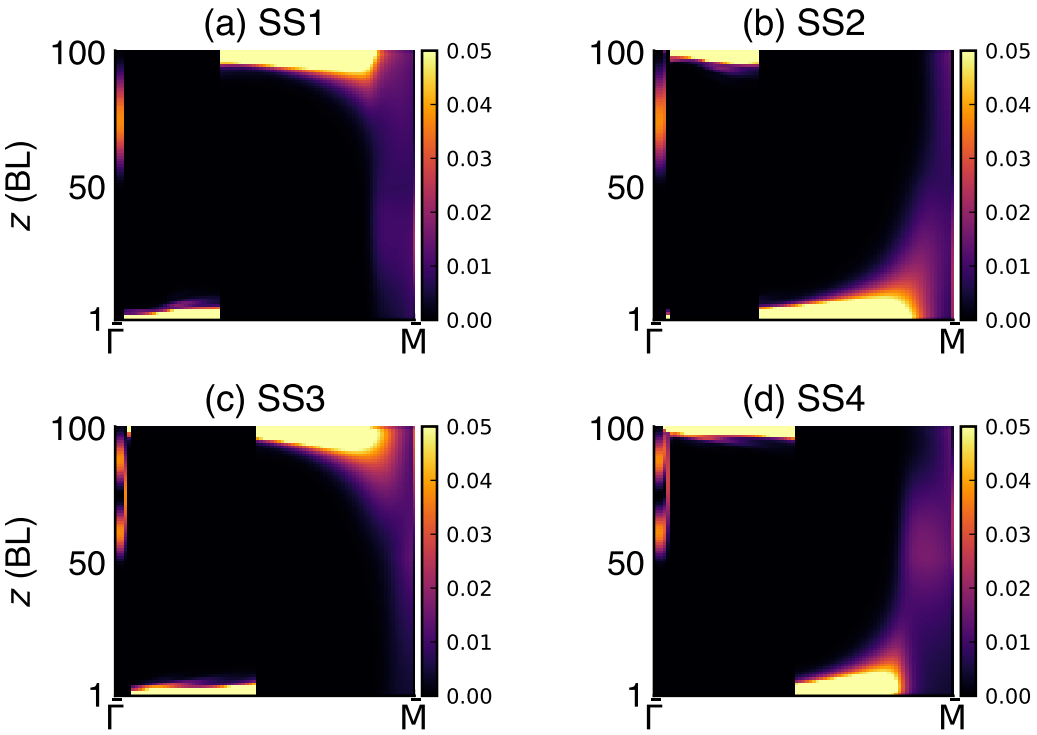

FIGURE 4.11
(a) to (d) are $k_{\|}$-dependence of probability distributions at SS1 to SS4, respectively. $z = 1$ is the BiSb surface. $z = 100$ is the Bi surface.

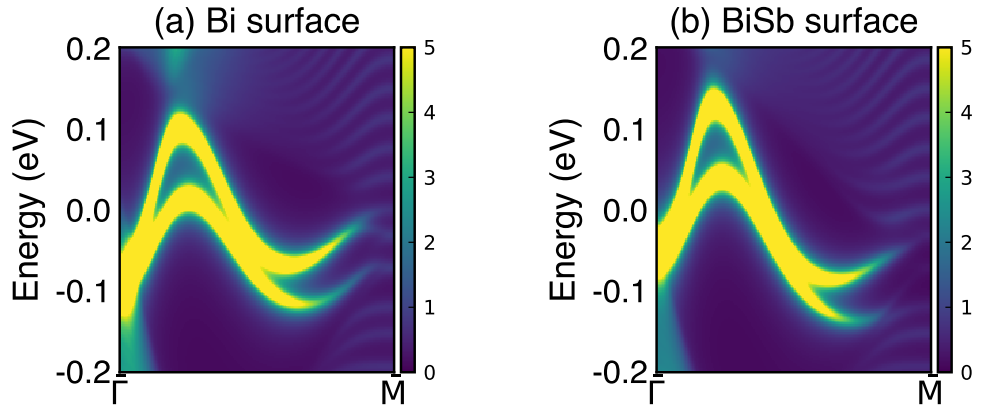

FIGURE 4.12
The $k_{\|}$-dependence of single-particle spectrum A of Bi/BiSb($x = 0.08$) (50+50 BL) for (a) Bi surface ($z = 100$ BL), and (b) BiSb surface ($z = 1$ BL).

The determination of the spatial distribution of eigenvalues based on the calculation of the probability distribution $|\psi(k_{\|}, z)|^2$ is consistent with the $k_{\|}$-dependence of the single-particle spectrum $A(k_{\|}, z, \varepsilon)$ on the Bi and BiSb surfaces shown in Fig. 4.12. However, we could not obtain detailed information near the $\bar{\text{M}}$-point. This is because the spectral intensity near the $\bar{\text{M}}$-point is unclear as shown in Fig. 4.12 and Fig. 4.13.

4.6 Sb content x-dependence of surface states

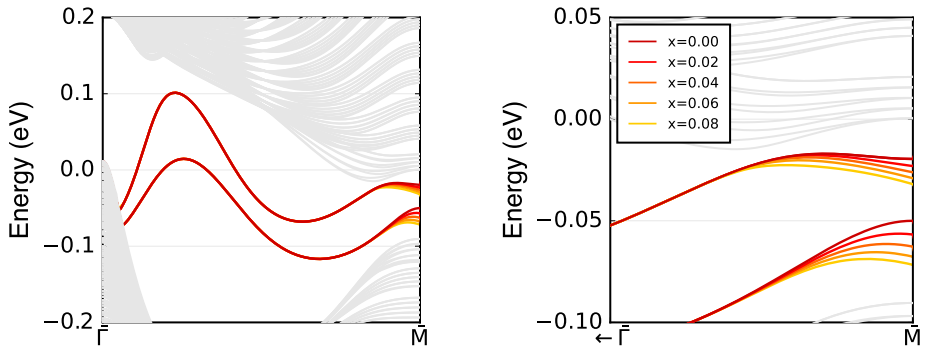

FIGURE 4.13
(a) Band structure of the Bi surface states of the Bi/BiSb heterojunctions for 50+50 thick slab. (b) Detailed Sb content x dependence of the Bi surface states at the $\bar{\text{M}}$-point

Figure 4.13 shows there is a x-dependence of the surface states around the $\bar{\text{M}}$-point and a no x-dependence of the surface states around the $\bar{\Gamma}$-point. We have calculated single-particle spectrums that allow us to obtain information for each bilayer in order to understand the cause of the difference between the $\bar{\Gamma}$- and $\bar{\text{M}}$-points. However, Fig. 4.11 and Fig. 4.12 could not display clear information about the $\bar{\text{M}}$-point. In order to obtain detailed results for the just $\bar{\text{M}}$-point, it is necessary to perform an analysis focusing on the $\bar{\text{M}}$-point. Therefore, we calculated the Sb content x-dependence of the single-particle spectrum at the just $\bar{\text{M}}$-point and we obtained a surprising result.

Figures 4.14 (a) and (b) show the x-dependence at the $\bar{\text{M}}$-point for the Bi and BiSb surfaces, respectively. The topologically non-trivial BiSb surface state ($x > 0.02$) does not exist because it is forbidden [12]. However, an extrapolation of the surface state ($x < 0.02$) to the prohibited region ($x > 0.02$) is in perfect match with the x-dependence of the Bi surface. In other words, the Bi surface state strongly interferes with the BiSb bulk state. Such a strong quantum size effect occurs between the Bi surface and Bi/BiSb interfaces at a spatial distance of 50 BL (approximately 20 nm). This long-range quantum size effect is unprecedented and completely unexpected. On the other hand, this quantum size effect does not exist at the $\bar{\Gamma}$-point. The x-dependence of Fig. 4.14 (c) and (d) is completely different. This difference between x-dependence of Bi surface and BiSb surface at the $\bar{\Gamma}$-point is evidence that the eigenvalues of the Bi surface state near the $\bar{\Gamma}$-point are un-changed for increasing Sb content x in the Fig. 4.9.

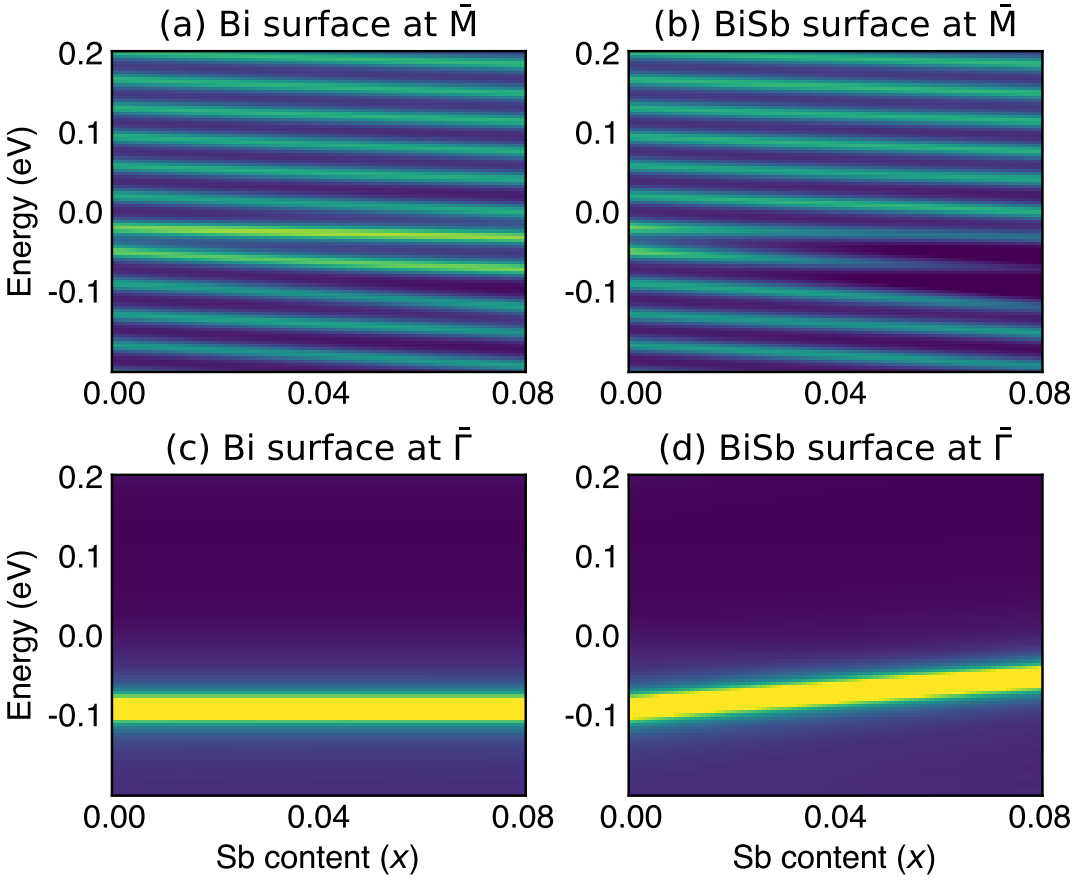

FIGURE 4.14
Sb content x-dependence of single-particle spectrum $A(k_{\|}, z, \varepsilon)$ of the Bi/BiSb heterojunction: (a) Bi surface ($z = 100$BL) at the $\bar{\text{M}}$-point, (b) BiSb surface ($z = 1$BL) at the $\bar{\text{M}}$-point, (c) Bi surface ($z = 100$BL) at the $\bar{\Gamma}$-point and (d) BiSb surface ($z = 1$BL) at the $\bar{\Gamma}$-point, respectively.

The difference between the $\bar{\Gamma}$-point (2D) and the $\bar{\text{M}}$-point (2D) originates from the large anisotropy of Bi. The valley at the $\bar{\Gamma}$-point (2D) corresponds to the hole at the T-point (3D) and the valley at the $\bar{\text{M}}$-point (2D) corresponds to the electron at the L-point (3D). The effective masses of holes and electrons are $m_h \sim 0.7$ and $m_e \sim 0.006$, respectively, and the wavelengths of the $\bar{\Gamma}$-point (2D) and the $\bar{\text{M}}$-point (2D) are 10 nm and 100 nm, respectively. As a result, there is the long-range permeation of electrons at the $\bar{\text{M}}$-point, but no permeation of electrons at the $\bar{\Gamma}$-point. The eigenvalues perform no x-dependence near the $\bar{\Gamma}$-point, but x-dependence near the $\bar{\text{M}}$-point as shown in Fig. 4.13.

4.7 Long-range permeation of wavefunction

We directly compare the free-standing Bi and BiSb energy band and single-particle spectrum for the CBM, S1, S2, and VBM labeled in the section 4.1.

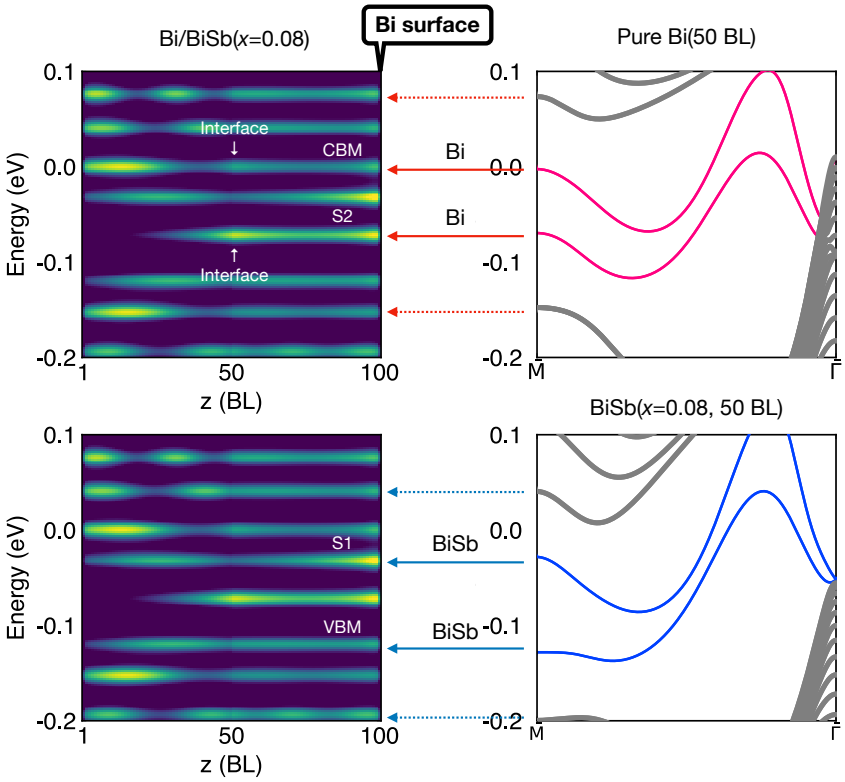

FIGURE 4.15
Comparison of single-particle spectrum $A(\bar{\mathrm{M}}, z, \varepsilon)$ of the Bi/BiSb heterojunction for 50+50 BL thick slab, and band structure of free-standing Bi and BiSb for 50BL thick slab.

Figure 4.15 shows that there is a characteristic structure on the Bi surface of the $\mathrm{Bi/Bi_{0.92}Sb_{0.08}}$ heterojunction for 50+50 BL film thickness at the $\bar{\mathrm{M}}$-point. In the comparison of the free-standing band structure and the single-particle spectrum at the $\bar{\mathrm{M}}$ point, the CBM and S2 peaks exist on the Bi surface ($z = 100$) of the Bi/BiSb heterojunction for 50+50 BL film thickness. They have energies consistent with the surface states of the free-standing Bi 50 BL. Therefore, the CBM is derived from the Bi surface state and is not a pure bulk state; the CBM is hybridized with the BiSb bulk through heterojunctions and appears to be a bulk state even though it is a Bi surface state from the energy band of the Bi/BiSb heterojunction. On the other hand, S1 does not have an interface state and has the same energy as the BiSb bulk state. S1 has a peak structure on the Bi surface. Therefore, S1 is the surface state of the Bi/BiSb heterojunction. However, S1 is not a pure Bi surface state and originates from BiSb bulk state.

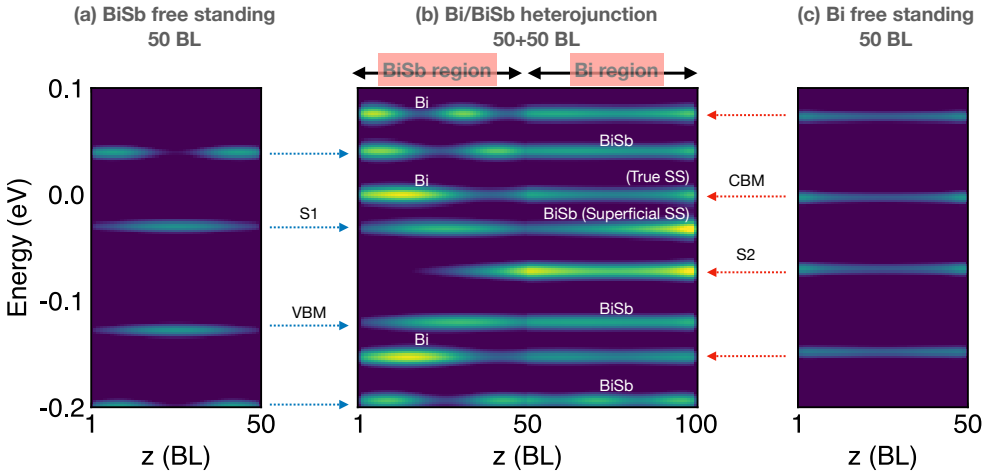

FIGURE 4.16
Comparison of single-particle spectrum $A(\bar{\mathrm{M}}, z, \varepsilon)$ of the Bi/BiSb heterojunction and the free-standing Bi and BiSb. (a) free-standing BiSb for 50 BL thick slab, (b) Bi/BiSb heterojunction for 50+50 BL thick slab, and (c) free-standing Bi for 50 BL thick slab. (For free-standing Bi and BiSb, the magnitude of A is reduced by 1/2 because their thickness is half that of Bi/BiSb heterojunction.)

Comparison of the free-standing BiSb and the single particle spectrum of the "Bi surface" at the $\bar{\mathrm{M}}$-points shows that S1 and VBM are consistent with the BiSb bulk state. Figure 4.16 demonstrates the emergence of a state-designated S1, which originates from the bulk of BiSb on the Bi surface of the Bi/BiSb heterojunction, and S1 is indicative of a surface state. There is no BiSb surface state at the $\bar{\mathrm{M}}$-point because the the BiSb surface state at the $\bar{\mathrm{M}}$-point is topologically forbidden [12]. In other words, the BiSb bulk state behaves surface state on the Bi surface as far as 50 BL (20 nm) away from BiSb. This behavior is a new example of the quantum size effect. Also, long-range penetration of the Bi wavefunction is observed in BiSb region away from Bi. Figure 4.16 shows that the wave functions of Bi and BiSb are mutually permeable. As described in the previous chapter, CBM and S2 derived from the surface state of the free-standing Bi for 50 BL thick slab. The CBM and S2 have peak structures of the single-particle spectrum not only at the Bi surface but also at the Bi/BiSb interface. The CBM and S2 behavior of the single-particle spectra in the Bi region, as shown in Fig. 4.15 and Fig. 4.16, is similar. This behavior is also similar to that of the free-standing Bi. From the above, we have considered the peaks at the interface of S2 and CBM are derived from the surface state of the free-standing Bi. On the other hand, S1 does not have the peak structure of the single-particle spectrum. BiSb does not have a surface state due to topological restriction. This inference answers the unexpected situation where S1 is not an interface state.

On the Bi surface, a "fake" surface state that does not originate from pure Bi appears. We call this "fake" surface state on the Bi surface a "superficial surface state". The CBM derived from the surface state of pure Bi is called the "true surface state."

4.8 Superficial surface state and topology of Bi

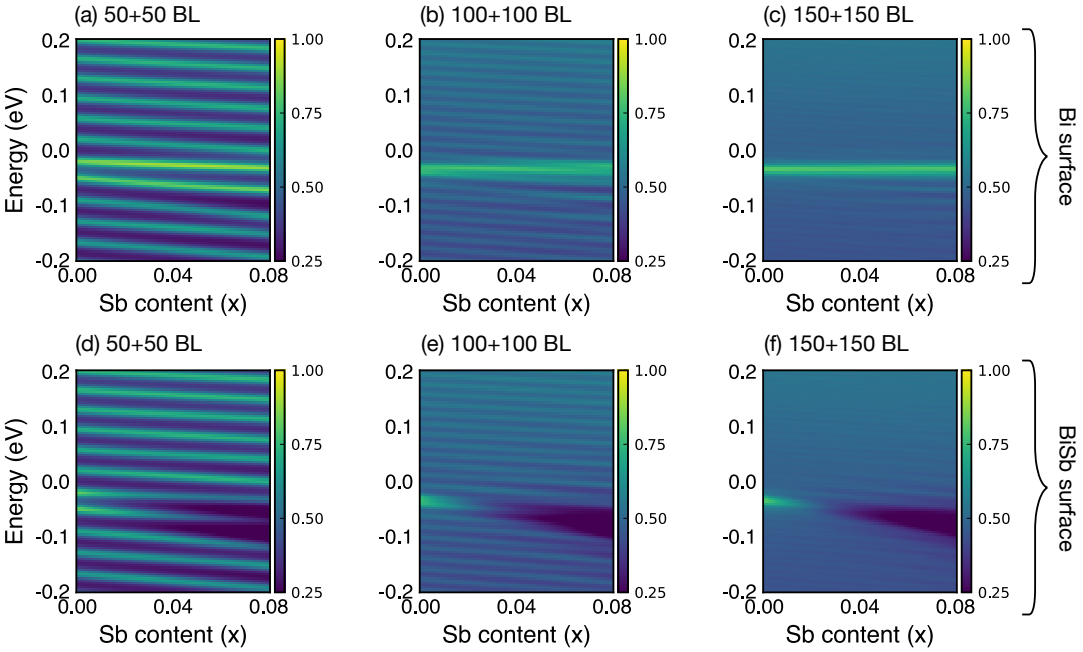

FIGURE 4.17
Sb content x-dependence of single-particle spectrum $A(\bar{\mathrm{M}}, z, \varepsilon)$ at the $\bar{\mathrm{M}}$-point. The upper panels are the spectra of the Bi surface for (a) 50+50 BL, (b) 100+100 BL, and (c) 150+150 BL thick slabs. The lower panels are the spectra of the BiSb surface for (d) 50+50 BL, (e) 100+100 BL, and (f) 150+150 BL thick slabs.

In Fig. 4.14, we mentioned that the Sb content x-dependence of the Bi surface and the BiSb surface at $\bar{\mathrm{M}}$-point are the same. If the interaction between the Bi surface and BiSb surface is due to the permeation of the wave function, the Sb content x-dependence of the Bi surface should disappear as the bilayer thickness is increased. Figure 4.17 shows the Sb content x-dependence of the $\bar{\mathrm{M}}$-point on the Bi and BiSb surfaces for each thickness. Figures 4.17 (a) and (d) illustrate that, in a 50+50BL, the dependence of Sb content x on the Bi and BiSb surfaces is consistent. Figures 4.17 (b) and (e) show that, in a 100+100BL, the dependence of Sb content x on the Bi surface is ambiguous. Finally, Figures 4.17 (c) and (f) indicate that, in a 150+150 BL, there is no correlation between the Bi and BiSb surfaces because of no Sb content x-dependence in the Bi surface. Figure 4.17 depicts the occurrence of permeation of the wave function, even within a 100+100 BL configuration, or a slab of 40 nanometers in thickness.

The penetration of wave functions imparts knowledge regarding another crucial characteristic of the Bi/BiSb heterojunction. S1 and S2 are distinctly discernible on the Bi surface; thus, it is evident that they are surface states. However, Figures 4.16 and 4.17 suggest that S1 is not a "true" surface state arising from Bi but rather a "fake" surface state arising from the BiSb substrate as a result of the penetration of the wave function.

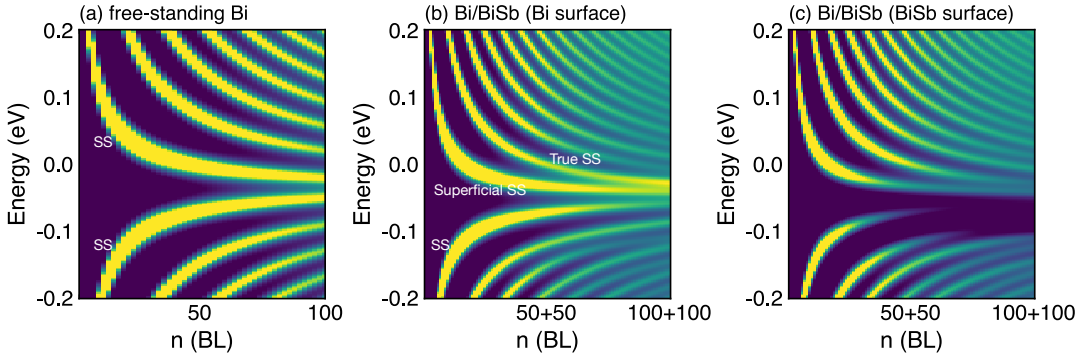

FIGURE 4.18
Thickness dependence of $A(\bar{\mathrm{M}}, \varepsilon)$ at the Bi surface for (a) free-standing Bi (n BL), (b) Bi/BiSb ($x = 0.08$) ($n + n$ BL) and (c) BiSb surface for Bi/BiSb ($x = 0.08$) ($n + n$ BL).

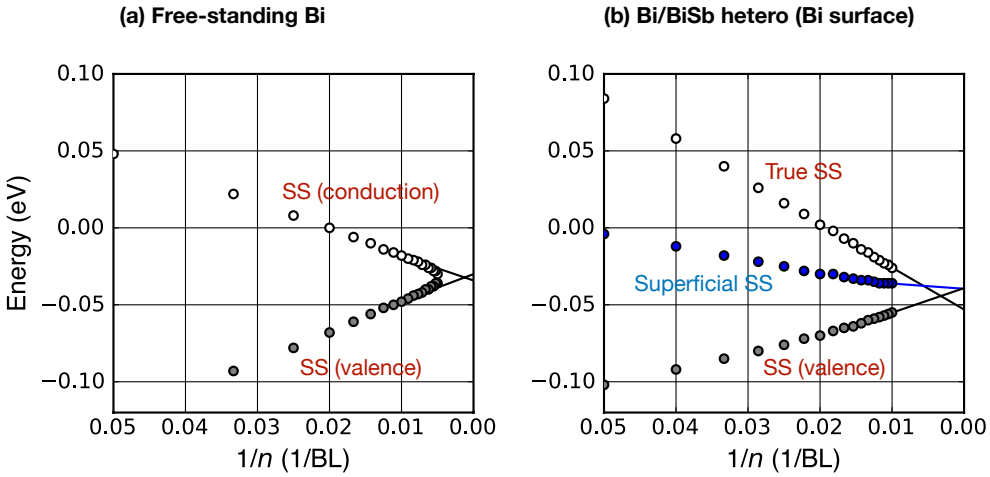

FIGURE 4.19
A peak positions of the single-particle spectrum $A(\bar{\mathrm{M}}, \varepsilon)$ are plotted as a function of $1/n$ for SS(valence) and SS(conduction) of (a) free-standing Bi and SS(valence), superficial surface state and true surface state of (d) Bi/BiSb($x = 0.08$). In (b), 1/n takes into account the film thickness on the Bi side. The lines are the extrapolated lines obtained by the least squares method for thick layers ($n \geq 80$ BL).

Figure 4.18 shows the thickness dependence of the single-particle spectrum at the surfaces of the free-standing Bi and the Bi/$Bi_{0.92}Sb_{0.08}$ heterojunction. The surface state disappears on the BiSb surface of the Bi/BiSb heterojunction. This is a reasonable result since this is the region where the surface state is prohibited by the topology. The surface state of the free-standing Bi appears symmetrical in the conduction and valence bands. In order to clarify this symmetric behavior of the surface bands, the dependence of the band gap on the inverse of the film thickness is plotted in Fig. 4.19. The thickness dependence of SS(conduction) and SS(valence) of the free-standing Bi is found to be nearly symmetric with respect to the center of the band gap; the symmetry of SS(conduction) and SS(valence) is a characteristic property of the Dirac electrons. The surface gap between SS(conduction) and SS(valence) appears to close around n = 200, clearly reflecting the topologically trivial property.

For example, Ito et al [57]. performed this plot for the ARPES measurement and concluded that Bi is non-trivial. On the other hand, for Bi/BiSb heterojunction systems, there exist true and superficial surface states in the conduction bands, which is very difficult to understand. The band gap of the Bi surface state of the Bi/BiSb heterojunction shows that the symmetry between SS(valence) and "superficial" surface state with respect to the gap center is broken. Furthermore, the chasm between SS(valence) and the "superficial" surface state is more substantial than in freestanding Bi and never converges around n = 200 to 300 BL. This gap symmetry breaking of two surface states and gap emergence in bulk limit is comprehensible, given that the "superficial" surface state emanates from the BiSb region. Therefore, in order to obtain true information about the Bi surface, we need to consider S2 and CBM: the thickness dependence of the band gap of SS(valence) and "true" surface state is more symmetric than that of SS(valence) and "superficial" surface state, and the gap between SS(valence) and "true" surface state closes after n = 200. Both the more symmetric behavior of SS(valence) and "true" surface state is consistent with the free-standing Bi surfaces.

Based on this understanding, the measurement of the surface state must take into account the influence of the substrate. Bi is a topologically trivial material. However, because of the existence of "superficial" surface state on the Bi surface due to BiSb substrate, the result is likely to be topologically non-trivial. The existence of superficial surface state has important implications for the determination of topology using Bi surface measurements[2].

Figure 4.18 (b) illustrates that the intensity of the "superficial" surface state, which was robust at thinner film thicknesses, becomes attenuated at thicker film thicknesses, and the "true" surface state appears to dominate at higher film thicknesses. The band gap gradient in Figure 4.19 (b) also appears to alter around 75 BL. This change in the gradient of the $1/n$ dependence can be attributed to the fact that the BiSb wavefunction does not interfere with a sufficient influence on the Bi surface. As the film thickness increases, the "superficial" surface state becomes indistinct. The SS(valence) and the "true" surface state appear to become more symmetrical with the gap center.

[2] A simple comparison with the experimental results of Ito et al [57]. is not possible due to the difference in the substrate material.

4.9 Thickness dependence of superficial surface state and true surface state

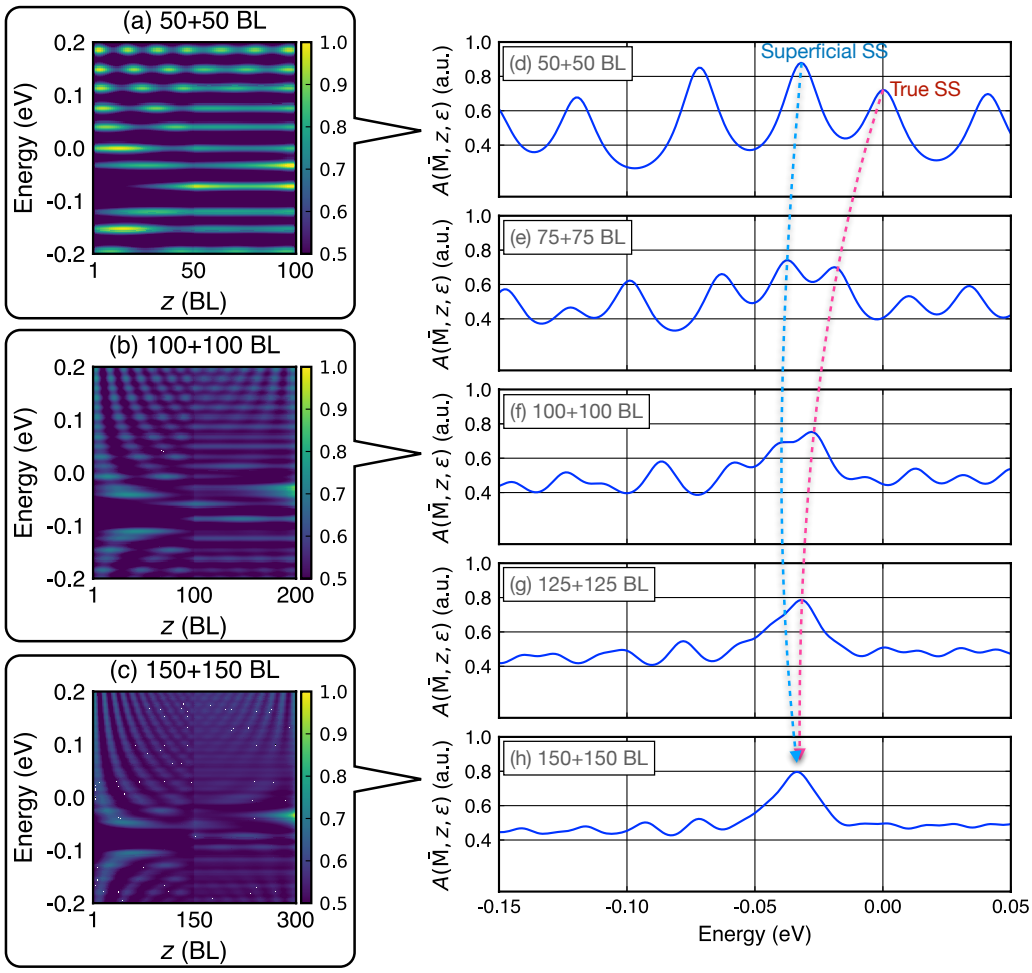

FIGURE 4.20
Band alignment at the $\bar{\mathrm{M}}$-point, $A(\bar{\mathrm{M}}, z, \varepsilon)$, for (a) 50+50 BL, (b) 100+100 BL and (c) 150+150 BL thick slabs. The profile of peak structure of single-particle spectrum on Bi surface at $\bar{\mathrm{M}}$ point for (d) 50+50 BL, (e) 75+75 BL, (f) 100+100 BL, (g) 125+125 BL and (h) 150+150 BL thick slabs.

The anomalous behavior of the "superficial" surface state originating from BiSb on the Bi surface can be noticed more clearly in the thickness dependence in Fig. 4.20. In the Fig. 4.20 (a-c), Bi surfaces ((a)$z = 100$, (b)$z = 200$ and (c)$z = 300$) clearly show the thickness dependence of the "true" surface state and the "superficial" surface state. For (a) 50+50 BL film thickness, the surface states are the "true" and "superficial" surface states. For (b) 100+100 BL film thickness, the "true" surface state and "superficial" surface state get to mix, and at (c) 150+150 BL film thickness, there is only one surface state. In order to observe this change in detail, we focused on the Bi surface and obtained the energy dependence of the single-particle spectra shown in Fig. 4.20 (d-h). The relation between the "superficial" surface state and "true" surface state peaks also has a thickness dependence. For the Bi/BiSb heterojunctions thinner than 75+75 BL (Fig. 4.20 (d,e)), "superficial" surface state is dominant. On the other hand, at thicknesses larger than 75+75 BL (Fig. 4.20 (f-h)), "true" surface state is dominant. After 75+75 BL, "superficial" surface state mixes with "true" surface state as the film thickness is increased, and at 150+150 BL (Fig. 4.20 (h)), the two are indistinguishable. For thinner films, less than 50+50 BL, the bulk wavefunction of BiSb reaches the Bi surface and appears as "superficial" surface state on the Bi surface. For the film thickness $z < 150 + 150$, there are two peaks in the single-particle spectrum that are considered to be surface states, so we distinguish between "superficial surface state" and "true surface state". The information in Fig. 4.20 (d-h) can be summarized as follows.

- (d) 50+50BL: Superficial SS (large) and True SS (small)
- (e) 75+75BL: Superficial SS and True SS
- (f) 100+100BL: Superficial SS (small) and True SS (large)
- (g) 125+125BL: Superficial SS and True SS get to mix.
- (h) 150+150BL: There is only one surface state.

"The true surface state" originated from free-standing Bi. On the other hand, "the superficial surface state" is that formed when the bulk wave function of BiSb reaches the Bi surface. The distinction of the presence of the quantum size effect is "whether the bulk wave function of BiSb is perceivable on the Bi surface or not."

4.10 Discussion

4.10.1 Topological interface state

The interface state of the topological heterojunction is clearly different from the expected picture in Fig. 4.1 (b). Band alignment in topological heterojunctions results in the formation of quantum well states. While the formation of quantum well states is a natural consequence, the mutual penetration of the wavefunctions of the junction materials is an unexpected result. In a trivial heterojunction case ($x < 0.02$), the electronic structures of the junction materials are analogous. Thus this mutual penetration is natural. However, in this unexpected result for $x = 0.08$, the energy levels of the junction materials are different, and the wavefunction penetrates a region where it cannot exist. It is not obvious that mutual permeation occurs even at $x = 0.08$ (trivial/non-trivial), where the energy levels are clearly different across the interface.

In such band-offset heterojunctions, it was naively expected that one energy band would spontaneously connect to an other band due to the band bending at the interface. However, no such band bending was observed. Instead, the energy levels permeated each other without bending. Therefore, we conclude that this long-range permeation is an unexpected result. The trivial heterojunction ($x < 0.02$) behaves as expected in a finite system (Fig. 4.1 (a)). On the other hand, we should carefully predict the topological heterojunction's property ($x = 0.08$) because it has long-range permeation.

The subtle band connection between the conduction band of BiSb and the valence band of Bi seen in Fig. 4.4 (f) (250+250 BL) may be an indication of the band connection expected in a topological heterojunction. If the scenario is as predicted in Fig. 4.1 (b), a valence band of the BiSb and a conduction band of the Bi should also be interconnected, resulting in the formation of crossing energy levels in the interface. However, no such crossing energy levels exist. More importantly, in the case of thin films, such connections are never observed. As shown in Fig. 4.4 (a), the band alignment of heterojunction Bi/BiSb cannot be obtained by simply connecting the free Bi and BiSb band alignments. The subtle band connection between the BiSb's conduction band and the Bi valence band only appears to be connected to both by permeation of the wavefunction of the interfacial state. The wavefunction's long-range penetration changes the energy bands at the surface and interface. The surface and interface states are divided into distinct eigenvalues in thicker film thickness as the surface-interface interference is resolved. Our calculations revealed that the interface state is unexpected. The interference between the surface and interface is up to about 100+100 BL.

4.10.2 Long-range permeation of wavefunction

The permeation of the Bi(BiSb) wavefunction creates states in the energy region that do not exist as eigenvalues of BiSb(Bi). The BiSb long-range wavefunction penetrates the Bi surface at a distance of 100 BL (40 nm) from the Bi/BiSb interface. This long-range permeation is a very unusual behavior. For $x < 0.02$ (trivial/trivial), the energy levels are almost the same, so mutual penetration of wavefunctions is possible. On the other hand, for $x = 0.08$ (trivial/non-trivial), the energy levels are different, and the topology is also different. In other words, our finding is that the energy levels appear in the region where the energy levels do not originally exist due to the long-range permeation. This long-range penetration results in the Sb content x-dependence between the top and bottom surfaces in the Bi/BiSb heterojunction being the same

behavior. The wavefunctions of the two substances coexist throughout the entire heterodevice, even though the substances are spatially separated. Precisely, we can fabricate "alloys" purely by engineering the heterojunction without the requirement of alloying the substances. This alloying technique is one method of band engineering without introducing a random distribution of atoms.

The wavefunctions of the surface states penetrate through the material with different topologies. Moreover, the surface states interfere with the surface states on the opposite side. Furthermore, when the film thickness is thin, and there are strong quantum size effects, the surface can even reflect information from the opposite material. A particularly iconic behavior of the wavefunction is that the bulk state of BiSb appears as a surface state at the Bi surface. Therefore, long-range penetration of the wave function can significantly impact surface-related measurements such as ARPES.

In other materials, such as $MnBi_2Se_4/Bi_2Se_3$ and $Bi_2Se_3/MnSe$, the penetration of the wave function is on the order of a few nm[90, 91]. The penetration length of the Bi/BiSb heterojunction's wave function differs from such materials by a factor of about 10. Hence, a weak quantum size effect between surfaces may exist in $MnBi_2Se_4/Bi_2Se_3$ and $Bi_2Se_3/MnSe$ [92], but it is not strong enough to allow for a superficial surface state. There are unique behaviors in the Bi/BiSb heterojunction system due to the long-range permeation of the wavefunction.

4.10.3 Other type quantum size effect

Interference effects between the surface and the interface are interesting as a phenomenon caused by the long-range penetration of the wavefunction. In the topological heterojunction shown in Fig.4.4 (a), the interface and the Bi surface have peaks at the same level. This result suggests that the surface state is pinned to the energy level of the interface state due to the interference effect between the surface and the interface. This effect appears at low film thicknesses of 50+50 BL. On the other hand, the interference effect disappears with increasing film thickness as shown in Fig.4.4 (d-f). The surface state can be fixed by the size effect. This study confirms the existence of such an unconventional quantum size effect.

4.10.4 Superficial surface state

Superficial surface state is the main finding in this study. The appearance of the superficial surface state is due to the strong quantum size effect caused by the long-range penetration of the wavefunction. The Bi and BiSb surfaces interfere strongly with each other in the Bi/BiSb heterojunction for 50+50 BL thick slab. Not only that, but also the mutual penetrating wave function reaches the surface up to 100+100 BL (40+40nm), and since there is no surface state at the $\bar{M}$-point of BiSb, the state that reaches the Bi surface is the BiSb bulk state. The superficial surface state originates from the BiSb bulk state. Therefore, the BiSb bulk state exists as a surface state at the Bi surface. Moreover, when the film thickness is less than 75+75 BL (30+30 nm), the superficial surface state has a more potent single-particle spectrum than the original Bi surface state. If the surface state information is to be used to determine the topology of Bi, the superficial surface state can have a negative impact on topology determination. From the analysis of the band gap of the surface state, we inferred that the superficial surface state might lead to the wrong result that Bi is non-trivial, even though Bi single-crystal is trivial in the calculation based on the Liu-Allen model. Of course, the situation differs depending on the substrate material. When analyzing

the band gap using BiSb as a substrate, it is necessary to start the measurement from a film thickness of 150 BL (60 nm) or more, where the superficial surface state is sufficiently small. Since surface-to-surface interferences remain from 200 to 300 BL(80 to 120 nm) [12], a film thickness of 300 BL or more is necessary to precisely determine the topology.

4.10.5 Topology of heterojunction systems

It has been reported that topological heterojunctions change the Chern number, which is a topological invariant of the system. Burkov et al.[15, 16] theoretically demonstrated that a superlattice consisting of a magnetized topological insulator and ordinary insulator layers stacked alternately could realize an intermediate phase between ordinary insulators and 3D quantum Hall insulators. However, heterojunctions do not affect the Z_2-topological invariants defined from a single bulk crystal. However, let us take the periodic boundary condition of two materials joined together and consider the giant system forming a superlattice as a bulk. We can newly determine the "Z_2-topology of heterojunction systems". Although the "Z_2 topology of heterojunction systems" has not been determined, Bi can have a surface state with information of BiSb bulk on its surface. Our study indicates that Bi is topologically trivial, but topological heterojunctions can generate surface states derived from "non-trivial BiSb" on the Bi surface.

Chapter 5

PbTe/SnTe topological heterojunction

PbTe and SnTe are thermoelectric materials known for a long time and have been studied from various aspects[71–77]. In the study of the PbSnTe system, topological properties have attracted the most attention in recent years. When PbTe is doped with Sn, band inversion occurs at the L-point in the three-dimensional Brillouin zone. The PbSnTe system has higher symmetry than the BiSb system, and the T-point of TRIM in the BiSb system does not exist because the symmetry at L-point and T-point is the same. Therefore, even if the band is inverted at the L-point, it is trivial for Z_2 classification. However, since PbSnTe has band inversion, it has a topological surface state protected by symmetry. In order to define a material, e.g., PbSnTe, as a topological material, an other classification is needed. The proposed classification in the PbSnTe system is that of a topological crystalline insulator. The mirror Chern number could classify topological crystalline insulators. Moreover, a gapless conduction state is expected at the PbTe/SnTe interface because the PbTe/SnTe system is band-inverded heterojunction; the PbTe/SnTe heterojunction can be a topological heterojunction. However, in the PbSnTe system, long-range penetration of the wavefunction cannot be expected. Therefore, the difference between PbTe/SnTe and Bi/BiSb heterojunctions is the existence of a strong quantum size effect. The PbTe/SnTe heterojunctions are good targets for comparison of the Bi/BiSb heterojunctions. In this chapter, we calculated the topological surface and interface states of the PbTe/SnTe heterojunction and discussed the differences between the Bi/BiSb and PbTe/SnTe heterojunction systems.

5.1 Surface and interface state

Band dispersions of free-standing PbTe and SnTe for 50 ML thick slab are shown in fig. 5.1. A band dispersion of the PbTe/SnTe heterojunction for a 50+50 ML thick slab is also shown in Fig. 5.2. Comparing Fig. 5.1 and Fig. 5.2, an energy band appears in the center of the energy gap in the PbTe/SnTe heterojunction at the $\bar{X}$-point that there is not in the single PbTe and SnTe. We calculated the single-particle spectrum $A(k_{\|}, z, \varepsilon)$ to obtain detailed information about this unexpected energy band in the gap, and $A(k_{\|}, z, \varepsilon)$ for the PbTe/SnTe heterojunction is shown in Fig. 5.3. From Fig. 5.3, the interface state appears in the gap. The surface states of the PbTe/SnTe heterojunction are perfectly consistent with the band dispersion of the free-standing PbTe and SnTe. The coincidence of the surface state of the PbTe/SnTe heterojunction and the band dispersion of the free-standing PbTe and SnTe indicate that the PbTe and SnTe surfaces are well separated from the PbTe/SnTe interface.

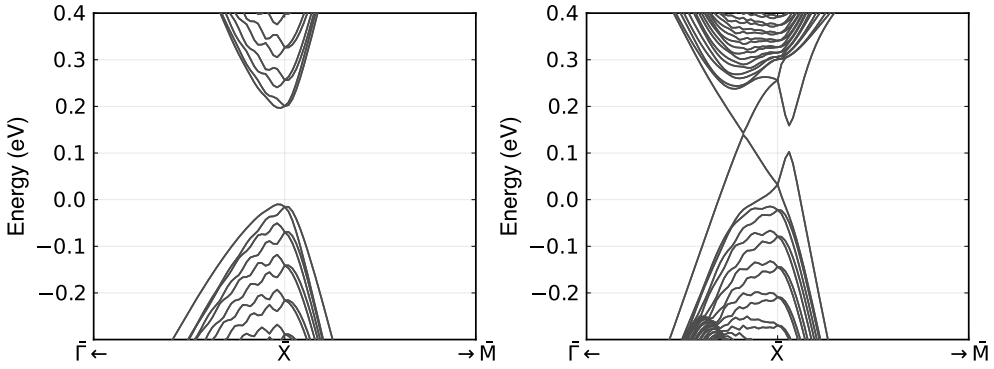

FIGURE 5.1
(a) Band structure of the free-standing PbTe for 50 ML thick slab.
(a) Band structure of the free-standing SnTe for 50 ML thick slab.

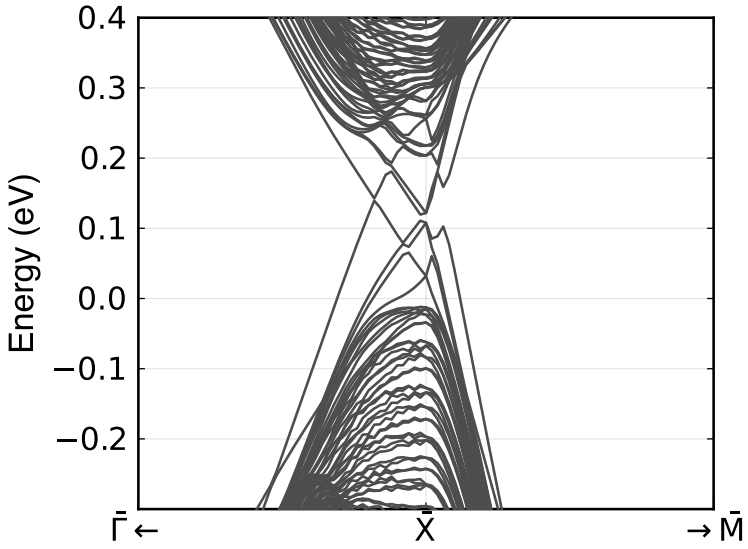

FIGURE 5.2
Band dispersion of the PbTe/SnTe heterojunction for 50+50 ML thick slab.

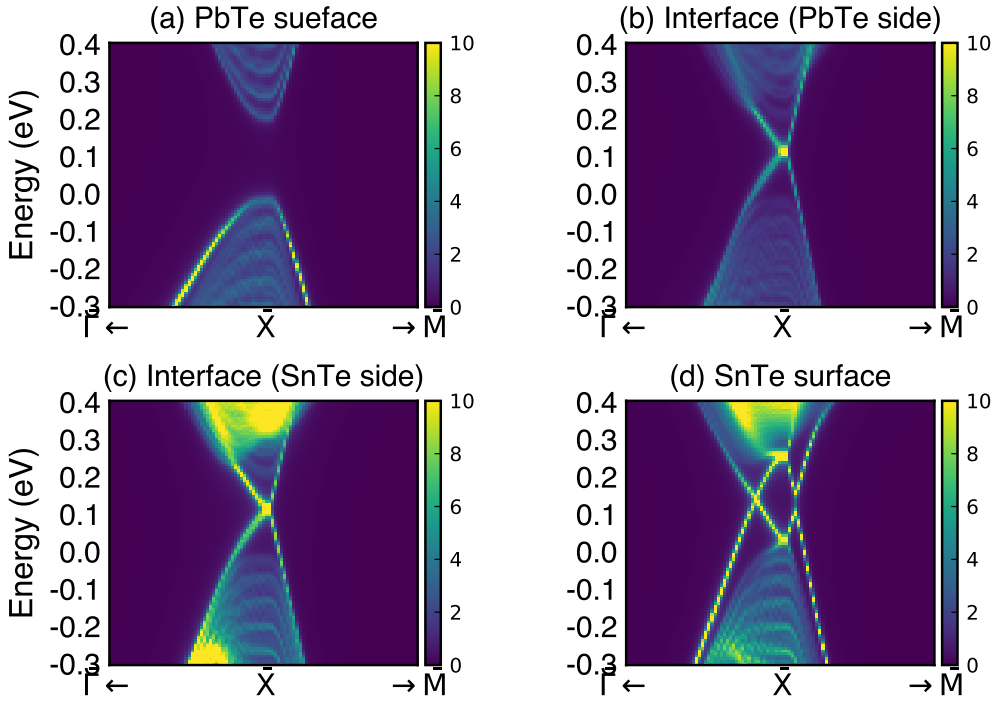

FIGURE 5.3
Single-particle spectrum $A(k_{\|}, z, \varepsilon)$ of the PbTe/SnTe topological heterojunction for 50+50 thick slab. (a) PbTe surface, (b) interface of PbTe side, (c) interface of SnTe side, and (d) SnTe surface, respectively.

In order to more clearly show the separation between the interface and surface, we calculated the z-dependence of the single-particle spectrum. Here, the penetration length of the interface and surface wavefunctions is about 15 ML(10nm). This penetration length is short compared to the Bi/BiSb heterojunction. There is no interference between the surface and interface state. The interface state has a tiny gap and is expected to become gapless when the film thickness increases. Band bending, which is expected for topological heterojunctions, is not observed. The interface state appears in the gap between the bulk bands of the free-standing PbTe and SnTe at the $\bar{\text{X}}$-point. The gapless state of the topological heterojunctions is realized at the interface. The band alignment that connects the conduction band (valence band) of PbTe and the valence band (conduction band) of SnTe, which is expected for a topological heterojunction, does not exist. Only a gapless state appears at the edge of the quantum well.

Next, we focus on the penetration of the bulk wavefunction. The penetration of the bulk wavefunction is also not so clear as shown in 5.4. However, the SnTe wavefunction permeates the inside of the PbTe region, although the intensity is weak. Similarly, the PbTe wavefunction also permeates the inside of the SnTe region. This weak intensity of permeation is because the effective masses of PbTe and SnTe are more significant than those of Bi and BiSb. Prominent quantum size effects, e.g., the superficial surface state in the Bi/BiSb heterojunctions, is not expected in the PbTe/SnTe heterojunctions.

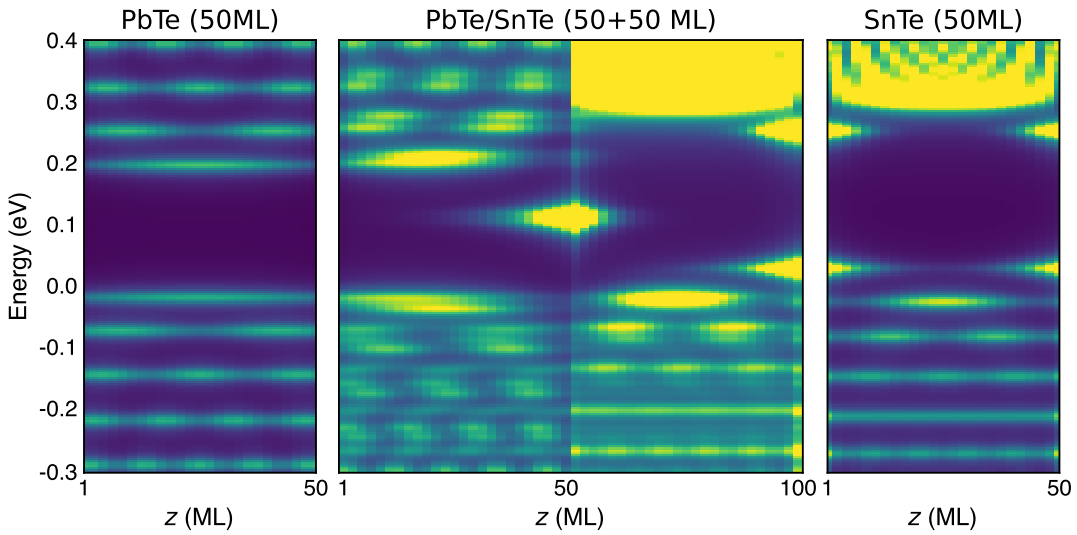

FIGURE 5.4
Comparison of the single-particle spectrum $A(\bar{\mathrm{M}}, z, \varepsilon)$ of the PbTe/SbTe heterojunction, free-standing PbTe, and SnTe 50ML. (a) free-standing PbTe for 50 ML thick slab, (b) PbTe/SnTe heterojunction for 50+50 ML thick slab, and (c) free-standing SnTe for 50 ML thick slab. (For the free-standing PbTe and SnTe, the magnitude of A is reduced by 1/2 because their thickness is half that of the PbTe/SnTe heterojunction.)

The difference is more clear when comparing the PbTe/SnTe heterojunction with the free-standing PbTe and SnTe in Fig. 5.4. In the free-standing SnTe, the bulk and surface states are consistent with the PbTe/SnTe heterojunction. The wavefunction of SnTe penetrates more deeply into PbTe, while the wavefunction of PbTe penetrates less deeply into SnTe. Here, the penetration lengths of each wave function are l_{PbTe} and l_{SnTe}, the relation is $l_{PbTe} < l_{SnTe}$. This relationship of the penetration length of the wavefunction is considered reasonable when looking at the interface state. The penetration length of the interface wave function is asymmetric between the PbTe side and the SnTe region; it is the SnTe electrons that seep into the PbTe side and the PbTe electrons that seep into the SnTe region. Since l_{SnTe} is larger, a permeation asymmetry is realized.

5.2 Difference between the Bi/BiSb and the PbTe/SnTe heterojunctions

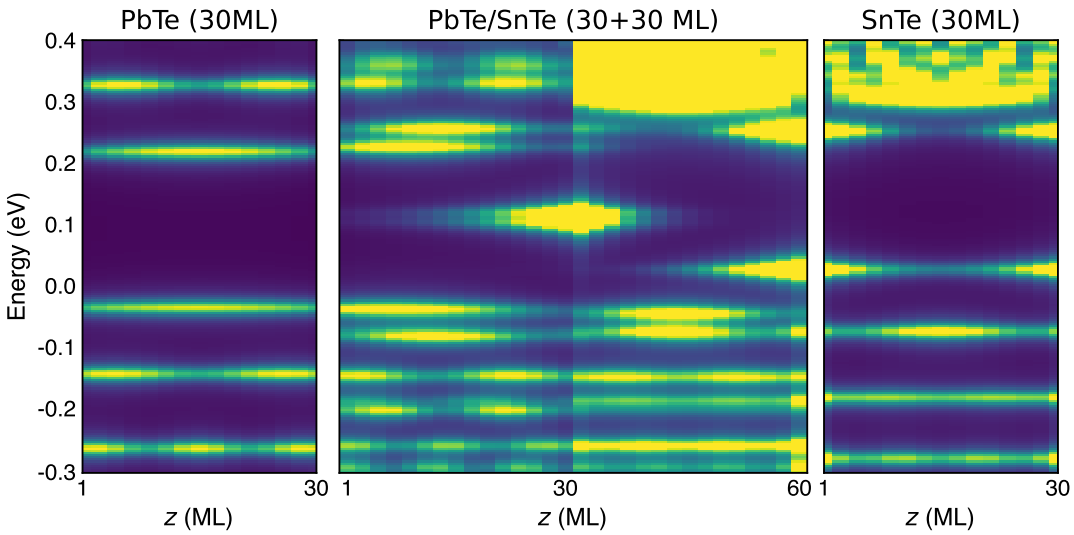

FIGURE 5.5
Comparison of the single-particle spectrum $A(\bar{\mathrm{M}}, z, \varepsilon)$ of the PbTe/SbTe heterojunction, free-standing PbTe, and SnTe 30ML. (a) free-standing PbTe for 30 ML thick slab, (b) PbTe/SnTe heterojunction for 30+30 ML thick slab, and (c) free-standing SnTe for 30 ML thick slab. (For the free-standing PbTe and SnTe, the magnitude of A is reduced by 1/2 because their thickness is half that of the PbTe/SnTe heterojunction.)

There is a difference between the Bi/$\mathrm{Bi}_{1-x}\mathrm{Sb}_x$ and the PbTe/SnTe heterojunctions. Figure 5.5 shows the band alignment of PbTe/SnTe heterojunction with 30+30 ML (approximetely 20+20 nm) film thickness, which is about the same size as the Bi/BiSb heterojunction for 50+50 BL (20+20 nm) film thickness. The PbTe/SnTe heterojunction does not have the superficial surface condition in the Bi/BiSb heterojunction. This is because the surface wavefunction does not reach the opposite surface. Figure 5.5 shows that the penetration length of the surface wavefunction is approximately 15 ML (10 nm) and does not extend to the opposite surface. On the other hand, the mutual penetration of the bulk wavefunction seen in the Bi/BiSb heterojunction is also present in PbTe/SnTe heterojunction. In addition, there is completely separation between the SnTe surface state and the PbTe/SnTe interface state. The situation is unlike the Bi/BiSb heterojunctions, where a single eigenvalue can be both the surface and interface state. Notice that PbTe without surface states is trivial, and SnTe with surface states is non-trivial. In the Bi/BiSb heterojunctions, Bi with surface states is trivial and BiSb without surface states at the $\bar{\mathrm{M}}$-point is non-trivial. Although the appearance of interface states is certainly due to topology, it is reasonable to assume that mutual permeation of wavefunctions occurs regardless of topology. The topological heterojunction makes an interface state in the gap. The $\bar{\mathrm{M}}$-points of the Bi and BiSb have minimal band gaps, so obtaining details in the gap requires increased resolution. Moreover, the Bi/BiSb heterojunction is complicated due to long-range penetrating wavefunctions. On the other hand, compared to the Bi/BiSb heterojunctions, the PbTe/SnTe heterojunctions are simpler systems because the band gap is relatively large and the penetration length of the wavefunction is not so long. In Fig. 5.5, there

is no band bending of the assumed surface states, but the bulk wavefunctions permeate each other. In Fig. 5.4, the mutual penetration of the bulk wavefunctions is also weaker. This weakened mutual penetration of the bulk wavefunction is similar to the situation observed in the Bi/BiSb heterojunction systems with an interface potential. For a "normal" topological heterojunction, where there is no long-range penetration of the wavefunction, and the band gap has enough size, the band alignment would be as shown in Fig. 5.4. The long-range penetration of the wavefunction makes the quantum size effect more prominent. The Bi/BiSb heterojunction system should be used rather than other materials (e.g., the PbTe/SnTe heterojunction) to study the effect of quantum size effects on topological heterojunctions.

5.3 Discussion

5.3.1 PbTe/SnTe heterojunctions

In the PbTe/SnTe heterojunction system, unlike the Bi/BiSb system, the surface state and the interface state are separated; the interface state does not exist as in the Bi/BiSb heterojunction. The asymmetry of the interface state directly reflects the penetration length of the wavefunction of PbTe and SnTe, which is reasonable since the penetration length of the wavefunction of the SnTe surface state is about 10 nm. The band calculation results show that an interface state appears in the gap, as expected. This interface state slightly opens the gap. The gap opening is thought to be due to the quantum size effect. Therefore, as the film thickness is increased, a gapless interface state is expected to appear. Such a weak quantum size effect is observed. On the other hand, the z-dependence of the single-particle spectra shows that there are no surface states on the SnTe surface that originate from the bulk PbTe wavefunction. The bulk wavefunction cannot reach the surface with sufficient strength. The bulk penetration loses strength the further away it is in space. The long-range interpenetration seen in the Bi/BiSb heterojunction is not possible in this system, and there are no strong quantum size effects that would cause unexpected surface states to appear as in the Bi/BiSb heterojunction system.

5.3.2 General topological heterojunctions

Topologically trivial/non-trivial insulator heterojunction systems create interface states at qualitatively specific wave numbers (band-inverted wave numbers). In Bi/BiSb systems, the wavefunctions are mutually permeable. In other trivial/non-trivial heterojunction systems, this mutual penetration is expected to occur similarly. However, the Bi/BiSb system has an extremely long wavefunction penetration length. This long-range mutual penetration of wavefunctions is impossible in other trivial/non-trivial heterojunction systems. If the mutual penetration of wavefunction were to exist in other trivial/non-trivial heterojunction systems, it would be an ultrathin film situation where the interfacial and surface states are mixed. If there is sufficient film thickness, there is no interference between the interface and the surface. Bi/BiSb systems are expected to behave the same way as other trivial/non-trivial heterojunctions if the film thickness is sufficient to eliminate the surface-interface interference effect.

5.3.3 Comparison of other topological heterojunctions

The electronic structures of pure Bi and BiSb ($x = 0.08$) are very close. The crucial difference between them is whether they are topologically trivial (pure Bi) or

non-trivial (BiSb). When $x = 0.00$, we can treat Bi/BiSb heterojunction as pure Bi. Since Bi (50 BL)/BiSb ($x < 0.02$, 50 BL) is a trivial/trivial heterojunction and Bi (50 BL)/BiSb ($x > 0.02$, 50 BL) is a trivial/non-trivial heterojunction, our calculation situation is not pure Bi(100 BL). However, Mutual penetration of wavefunctions occurs regardless of the topology differences between materials. In addition, the energy levels of pure Bi(50 BL) and BiSb ($x = 0.08$, 50 BL) differ. In other words, we recognize that one of our findings is that levels appear in regions where energy levels do not originally exist. Our scenario of quantum size effect would be applicable for heterojunctions with long wavelengths. The electrons at the $\bar{\text{M}}$-point of the Bi/BiSb heterojunction, which we studied, provide a good stage for this scenario. A similar system with a comparable long wavelength must provide another opportunity to observe the long-range permeation.

Here, we discuss two types of topological heterojunctions, $TlBiTe_2/InBiTe_2$ and Bi_2Te_3/Bi, briefly.

$TlBiTe_2/InBiTe_2$ heterojunctions

In the case of $TlBiTe_2/InBiTe_2$, $TlBiTe_2$ has Dirac-like electrons at the Γ-point(3D)[63, 64]. The situation is similar to the L-point(3D) of Bi. Therefore, the long-range permeation and superficial surface state may be observed even in $TlBiTe_2/InBiTe_2$. However, the quantum-size effect is expected to be less significant than Bi/BiSb because the wavelength of $TlBiTe_2$ is much shorter than that of Bi[63, 64, 93].

Bi_2Te_3/Bi heterojunctions

In the Bi_2Te_3/Bi topological heterojunction, there is a large band gap at the $\bar{\text{M}}$-point of Bi_2Te_3 [94]. Also, a long penetration length is not expected at the $\bar{\text{M}}$ point of Bi_2Te_3. Therefore, the Bi_2Te_3 wavefunction will not permeate into the Bi band gap. The superficial surface state at the Bi surface is not expected. On the other hand, according to our observation, the Bi electrons can permeate into the attached substance due to their long wavelength, even if there are no corresponding energy levels. The Bi wave function is expected to penetrate the bandgap of Bi_2Te_3 because of its long penetration length. At the $\bar{\Gamma}$-point, Bi_2Te_3 and Bi have the same scale energy levels. However, the penetration length of the Bi wavefunction at the $\bar{\Gamma}$-point is much shorter than that at the $\bar{\text{M}}$-point, which does not allow for long-range permeation. On the Bi_2Te_3 side, the wavefunction's penetration length is much shorter than that of $\bar{\text{M}}$-point of Bi due to the lack of steep band dispersion in the bulk band, which also prevents long penetration of the wavefunction. Therefore, the competition between the blocking of Bi_2Te_3 side and permeating of the Bi side occurs, which must be an interesting future problem.

Chapter 6

Summary

In this doctoral thesis, we investigated the quantum size effect in topological heterojunctions in the Bi/BiSb and PbSn/SnTe systems using the tight-binding model.

In Chapter 4, we calculated the energy bands, probability distribution, and single-particle spectrum. As a result, we found a different quantum size effect from the conventional one where the surface state is pinned to the energy level of the interface state due to the interference effect between the surface and interface states. Additionally, we confirmed the unconventional picture of the interface state, and observed the easily observable x-dependence of the Bi/BiSb system, which makes a variety of analyses possible. Through diverse analyses, we discovered the "superficial" surface state on the Bi surface, which originates from the bulk state of BiSb. In the Bi/BiSb heterojunctions, the appearance of the superficial surface state is due to the long-range penetration of the wavefunction. This "superficial" surface state appears only at the $\bar{\mathrm{M}}$-point, where the effective mass is very small. The quantum size effect must remain strong for the "superficial" surface state to appear. (Specifically, the thickness of the Bi film from the interface for the BiSb substrate is less than 40 nm.) This long-range penetration of the wavefunction at the $\bar{\mathrm{M}}$-point is a unique example. Surface-surface interference in the BiSb system occurs even when the system size is about 100 nm. The long-range penetration of the wavefunction is often less than 10 nm for common topological materials, such as Bi_2Se_3. Therefore, the calculation results confirm that the Bi/BiSb heterojunction is a good target for the quantum size effects to appear.

In Chapter 5, we calculated the PbTe/SnTe heterojunctions for comparison to the Bi/BiSb heterojunctions. We confirmed the mutual penetration of bulk wavefunctions that are close in distance but have no bulk state that behaves as a surface state like the Bi/BiSb surface state. The penetration length of the wavefunction in the PbSnTe system is much shorter than that in the BiSb system. In addition, the interface states are well separated from the surface states. There is no obvious surface-interface interference effect. The penetration of the interface wavefunction is asymmetric between the PbTe and SnTe sides, allowing us to distinguish between the penetration of electrons in PbTe and that in SnTe. This result does not rule out that the wavefunctions of topological and ordinary insulators can penetrate each other. Our calculations show that the mutual penetration of the Bi/BiSb topological heterojunction is correct.

Bibliography

[1] C. Kittel, *Introduction to solid state physics* (Wiley, 2005).

[2] T. Ihn, *Semiconductor nanostructures: quantum states and electronic transport* (OUP Oxford, 2010).

[3] G. Bastard, F. Carosella, and C. Ndebeka-bandou, *Quantum states and scattering in semiconductor nanostructures*, Advanced Textbooks In Physics (World Scientific Publishing Company, 2017).

[4] B. A. Volkov and O. A. Pankratov, "Two-dimensional massless electrons in an inverted contact", JETP Lett **42**, 178 (1985).

[5] E. Fradkin, E. Dagotto, and D. Boyanovsky, "Physical realization of the parity anomaly in condensed matter physics", Phys. Rev. Lett. **57**, 2967–2970 (1986).

[6] N. A. Cade, "Quantum well bound states of HgTe in CdTe", Journal of Physics C: Solid State Physics **18**, 5135–5141 (1985).

[7] Y.-C. Chang, J. N. Schulman, G. Bastard, Y. Guldner, and M. Voos, "Effects of quasi-interface states in HgTe-CdTe superlattices", Phys. Rev. B **31**, 2557–2560 (1985).

[8] Y. R. Lin-Liu and L. J. Sham, "Interface states and subbands in HgTe-CdTe heterostructures", Phys. Rev. B **32**, 5561–5563 (1985).

[9] O. Pankratov, S. Pakhomov, and B. Volkov, "Supersymmetry in heterojunctions: band-inverting contact on the basis of $Pb_{1-x}Snx$Te and $Hg_{1-x}Cd_x$Te", Solid State Communications **61**, 93–96 (1987).

[10] S.-Q. Shen, W.-Y. Shan, and H.-Z. Lu, "Topological insulator and the dirac equation", in Spin, Vol. 1, 01 (World Scientific, 2011), pp. 33–44.

[11] S.-Q. Shen, *Topological insulators* (Springer-Verlag Berlin Heidelberg, 2012).

[12] Y. Fuseya and H. Fukuyama, "Analytical solutions for the surface states of $Bi_{1-x}Sb_x$", J. Phys. Soc. Jpn. **87**, 044710 (2018).

[13] G. Wu, H. Chen, Y. Sun, X. Li, P. Cui, C. Franchini, J. Wang, X.-Q. Chen, and Z. Zhang, "Tuning the vertical location of helical surface states in topological insulator heterostructures via dual-proximity effects", Scientific Reports **3**, 1–7 (2013).

[14] T. Shoman, A. Takayama, T. Sato, S. Souma, T. Takahashi, T. Oguchi, K. Segawa, and Y. Ando, "Topological proximity effect in a topological insulator hybrid", Nature Communications **6**, 6547 (2015).

[15] A. A. Burkov and L. Balents, "Weyl semimetal in a topological insulator multilayer", Phys. Rev. Lett. **107**, 127205 (2011).

[16] A. A. Burkov, M. D. Hook, and L. Balents, "Topological nodal semimetals", Phys. Rev. B **84**, 235126 (2011).

[17] L. Fu and C. L. Kane, "Topological insulators with inversion symmetry", Phys. Rev. B **76**, 045302 (2007).

[18]J. C. Y. Teo, L. Fu, and C. L. Kane, "Surface states and topological invariants in three-dimensional topological insulators: application to $Bi_{1-x}Sb_x$", Phys. Rev. B **78**, 045426 (2008).

[19]Y. Fuseya, M. Ogata, and H. Fukuyama, "Transport properties and diamagnetism of Dirac electrons in bismuth", J. Phys. Soc. Jpn. **84**, 012001 (2015).

[20]Y. Liu and R. E. Allen, "Electronic structure of the semimetals Bi and Sb", Phys. Rev. B **52**, 1566–1577 (1995).

[21]K. Saito, H. Sawahata, T. Komine, and T. Aono, "Tight-binding theory of surface spin states on bismuth thin films", Phys. Rev. B **93**, 041301 (2016).

[22]W. Shockley, "The theory of p-n junctions in semiconductors and p-n junction transistors", Bell System Technical Journal **28**, 435–489 (1949).

[23]W. Shockley, "A unipolar "field-effect" transistor", Proceedings of the IRE **40**, 1365–1376 (1952).

[24]R. L. Anderson, "Germanium-gallium arsenide heterojunctions [letter to the editor]", IBM Journal of Research and Development **4**, 283–287 (1960).

[25]W. Shockley and H. J. Queisser, "Detailed balance limit of efficiency of p-n junction solar cells", Journal of applied physics **32**, 510–519 (1961).

[26]L. Esaki, "New phenomenon in narrow germanium $p - n$ junctions", Phys. Rev. **109**, 603–604 (1958).

[27]L. Vegard, "Die konstitution der mischkristalle und die raumfüllung der atome", Zeitschrift für Physik **5**, 17–26 (1921).

[28]A. R. Denton and N. W. Ashcroft, "Vegard's law", Phys. Rev. A **43**, 3161–3164 (1991).

[29]V. N. Lutskii, "Quantum size effect–-present state and perspectives of experimental investigations", physica status solidi (a) **1**, 199–220 (1970).

[30]N. Holonyak, R. Kolbas, R. Dupuis, and P. Dapkus, "Quantum-well heterostructure lasers", IEEE Journal of Quantum Electronics **16**, 170–186 (1980).

[31]N Holonyak Jr, R. Kolbas, W. Laidig, B. Vojak, K Hess, R. Dupuis, and P. Dapkus, "Phonon-assisted recombination and stimulated emission in quantum-well $Al_xGa_{1-x}As$-GaAs heterostructures", Journal of Applied Physics **51**, 1328–1337 (1980).

[32]R. Dingle, A. C. Gossard, and W. Wiegmann, "Direct observation of superlattice formation in a semiconductor heterostructure", Phys. Rev. Lett. **34**, 1327–1330 (1975).

[33]C. L. Kane and E. J. Mele, "Z_2 Topological order and the quantum spin hall effect", Phys. Rev. Lett. **95**, 146802 (2005).

[34]C. L. Kane and E. J. Mele, "Quantum spin hall effect in graphene", Phys. Rev. Lett. **95**, 226801 (2005).

[35]B. A. Bernevig and S.-C. Zhang, "Quantum spin hall effect", Phys. Rev. Lett. **96**, 106802 (2006).

[36]L. Fu, C. L. Kane, and E. J. Mele, "Topological insulators in three dimensions", Phys. Rev. Lett. **98**, 106803 (2007).

[37]R. Roy, "Topological phases and the quantum spin hall effect in three dimensions", Phys. Rev. B **79**, 195322 (2009).

[38]V. Volkov and V. Enaldiev, "Surface states of a system of dirac fermions: a minimal model", Journal of Experimental and Theoretical Physics **122**, 608–620 (2016).

[39]Y. Hatsugai, "Chern number and edge states in the integer quantum hall effect", Phys. Rev. Lett. **71**, 3697–3700 (1993).

[40]Y. Hatsugai, "Edge states in the integer quantum hall effect and the Riemann surface of the Bloch function", Phys. Rev. B **48**, 11851–11862 (1993).

[41]J. McIver, D. Hsieh, H. Steinberg, P. Jarillo-Herrero, and N. Gedik, "Control over topological insulator photocurrents with light polarization", Nature nanotechnology **7**, 96–100 (2012).

[42]Y. Shiomi, K. Nomura, Y. Kajiwara, K. Eto, M. Novak, K. Segawa, Y. Ando, and E. Saitoh, "Spin-electricity conversion induced by spin injection into topological insulators", Phys. Rev. Lett. **113**, 196601 (2014).

[43]C. H. Li, O. M. J. van 't Erve, J. T. Robinson, Y. Liu, L. Li, and B. T. Jonker, "Electrical detection of charge-current-induced spin polarization due to spin-momentum locking in Bi_2Se_3", Nature Nanotechnology **9**, 218–224 (2014).

[44]Y. Ando, T. Hamasaki, T. Kurokawa, K. Ichiba, F. Yang, M. Novak, S. Sasaki, K. Segawa, Y. Ando, and M. Shiraishi, "Electrical detection of the spin polarization due to charge flow in the surface state of the topological insulator $Bi_{1.5}Sb_{0.5}Te_{1.7}Se_{1.3}$", Nano letters **14**, 6226–6230 (2014).

[45]P. A. M. Dirac, "The quantum theory of the electron", Proc. Roy. Soc. Lond. A **117**, 610 (1928).

[46]W.-Y. Shan, H.-Z. Lu, and S.-Q. Shen, "Effective continuous model for surface states and thin films of three-dimensional topological insulators", New Journal of Physics **12**, 043048 (2010).

[47]J. Linder, T. Yokoyama, and A. Sudbø, "Anomalous finite size effects on surface states in the topological insulator Bi_2Se_3", Phys. Rev. B **80**, 205401 (2009).

[48]H.-Z. Lu, W.-Y. Shan, W. Yao, Q. Niu, and S.-Q. Shen, "Massive Dirac fermions and spin physics in an ultrathin film of topological insulator", Phys. Rev. B **81**, 115407 (2010).

[49]C.-X. Liu, H. Zhang, B. Yan, X.-L. Qi, T. Frauenheim, X. Dai, Z. Fang, and S.-C. Zhang, "Oscillatory crossover from two-dimensional to three-dimensional topological insulators", Phys. Rev. B **81**, 041307 (2010).

[50]M. Z. Hasan and C. L. Kane, "*Colloquium* : topological insulators", Rev. Mod. Phys. **82**, 3045–3067 (2010).

[51]G. Krizman, B. A. Assaf, M. Orlita, G. Bauer, G. Springholz, R. Ferreira, L. A. de Vaulchier, and Y. Guldner, "Interaction between interface and massive states in multivalley topological heterostructures", Phys. Rev. Research **4**, 013179 (2022).

[52]B. A. Bernevig, T. L. Hughes, and S.-C. Zhang, "Quantum spin hall effect and topological phase transition in HgTe quantum wells", Science **314**, 1757–1761 (2006).

[53]Y. Fuseya, M. Ogata, and H. Fukuyama, "Spin-hall effect and orbital magnetism of anisotropic Dirac electrons in solids", J. Phys. Soc. Jpn. **83**, 074702 (2014).

[54]I. Aguilera, H.-J. Kim, C. Friedrich, G. Bihlmayer, and S. Blügel, "Z_2 Topology of bismuth", Phys. Rev. Materials **5**, L091201 (2021).

[55]C. S. Lent, M. A. Bowen, J. D. Dow, R. S. Allgaier, O. F. Sankey, and E. S. Ho, "Relativistic empirical tight-binding theory of the energy bands of GeTe, SnTe, PbTe, PbSe, PbS, and their alloys", Superlattices and Microstructures **2**, 491–499 (1986).

[56]J. A. Van Vechten and T. K. Bergstresser, "Electronic structures of semiconductor alloys", Phys. Rev. B **1**, 3351–3358 (1970).

[57]S. Ito, B. Feng, M. Arita, A. Takayama, R.-Y. Liu, T. Someya, W.-C. Chen, T. Iimori, H. Namatame, M. Taniguchi, C.-M. Cheng, S.-J. Tang, F. Komori, K. Kobayashi, T.-C. Chiang, and I. Matsuda, "Proving nontrivial topology of pure bismuth by quantum confinement", Phys. Rev. Lett. **117**, 236402 (2016).

[58]D. Hsieh, D. Qian, L. Wray, Y. Xia, Y. S. Hor, R. J. Cava, and M. Z. Hasan, "A topological Dirac insulator in a quantum spin hall phase", Nature **452**, 970 (2008).

[59]Y. Ohtsubo, L. Perfetti, M. O. Goerbig, P. L. Fevre, F. Bertran, and A. Taleb-Ibrahimi, "Non-trivial surface-band dispersion on Bi(111)", New Journal of Physics **15**, 033041 (2013).

[60]Y. Ohtsubo and S. Kimura, "Topological phase transition of single-crystal Bi based on empirical tight-binding calculations", New Journal of Physics **18**, 123015 (2016).

[61]F. Wei, C.-W. Liu, D. Li, C.-Y. Wang, H.-R. Zhang, J.-R. Sun, X. P. A. Gao, S. Ma, and Z. Zhang, "Broken mirror symmetry tuned topological transport in PbTe/SnTe heterostructures", Phys. Rev. B **98**, 161301 (2018).

[62]Z. Zhu, B. Fauqué, Y. Fuseya, and K. Behnia, "Angle-resolved landau spectrum of electrons and holes in bismuth", Phys. Rev. B **84**, 115137 (2011).

[63]Y. L. Chen, Z. K. Liu, J. G. Analytis, J.-H. Chu, H. J. Zhang, B. H. Yan, S.-K. Mo, R. G. Moore, D. H. Lu, I. R. Fisher, S. C. Zhang, Z. Hussain, and Z.-X. Shen, "Single Dirac cone topological surface state and unusual thermoelectric property of compounds from a new topological insulator family", Phys. Rev. Lett. **105**, 266401 (2010).

[64]S. V. Eremeev, G. Bihlmayer, M. Vergniory, Y. M. Koroteev, T. V. Menshchikova, J. Henk, A. Ernst, and E. V. Chulkov, "Ab initio electronic structure of thallium-based topological insulators", Phys. Rev. B **83**, 205129 (2011).

[65]M. H. Cohen and E. I. Blount, Phil. Mag. **5**, 115 (1960).

[66]P. A. Wolff, J. Phys. Chem. Solids **25**, 1057 (1964).

[67]P. O. Löwdin, "A note on the quantum-mechanical perturbation theory", J. Chem. Phys. **19**, 1396–1401 (1951).

[68]R. Winkler, *Spin-orbit coupling effects in two-dimensional electron and hole systems* (Springer-Verlag, 2003).

[69]J. O. Dimmock, I. Melngailis, and A. J. Strauss, "Band structure and laser action in $Pb_xSn_{1-x}Te$", Phys. Rev. Lett. **16**, 1193–1196 (1966).

[70]G. A. Saunders, "Semimetals and narrow gap semiconductors", Contemporary Physics **14**, 149–166 (1973).

[71]K. Behnia, *Fundamentals of thermoelectricity* (OUP Oxford, 2015).

[72]H. Hayasaka and Y. Fuseya, "Crystalline spin–orbit interaction and the zeeman splitting in $Pb_{1-x}Sn_xTe$", Journal of Physics: Condensed Matter **28**, 31LT01 (2016).

[73]L. Fu, "Topological crystalline insulators", Phys. Rev. Lett. **106**, 106802 (2011).

[74]T. H. Hsieh, H. Lin, J. Liu, W. Duan, A. Bansil, and L. Fu, "Topological crystalline insulators in the SnTe material class", Nature Communications **3**, 982 (2012).

[75]S.-Y. Xu, C. Liu, N Alidoust, M Neupane, D Qian, I Belopolski, J. Denlinger, Y. Wang, H Lin, L. a. Wray, et al., "Observation of a topological crystalline insulator phase and topological phase transition in $Pb_{1-x}Sn_xTe$", Nature communications **3**, 1–11 (2012).

[76]P Dziawa, B. Kowalski, K Dybko, R Buczko, A Szczerbakow, M Szot, E Lusakowska, T Balasubramanian, B. M. Wojek, M. Berntsen, et al., "Topological crystalline insulator states in $Pb_{1-x}Sn_xSe$", Nature materials **11**, 1023–1027 (2012).

[77]M. Kriechbaum, K. E. Ambrosch, E. J. Fantner, H. Clemens, and G. Bauer, "Electronic structure of $\frac{PbTe}{Pb_{1-x}Sn_xTe}$ te superlattices", Phys. Rev. B **30**, 3394–3405 (1984).

[78]S. Golin, "Band structure of bismuth: pseudopotential approach", Phys. Rev. **166**, 643–651 (1968).

[79]L. M. Falicov and P. J. Lin, "Band structure and fermi surface of antimony: pseudopotential approach", Phys. Rev. **141**, 562–567 (1966).

[80]X. Gonze, J.-P. Michenaud, and J.-P. Vigneron, "First-principles study of As, Sb, and Bi electronic properties", Phys. Rev. B **41**, 11827–11836 (1990).

[81]C. R. Ast and H. Höchst, "Fermi surface of Bi(111) measured by photoemission spectroscopy", Phys. Rev. Lett. **87**, 177602 (2001).

[82]C. R. Ast and H. Höchst, "Electronic structure of a bismuth bilayer", Phys. Rev. B **67**, 113102 (2003).

[83]H. M. Benia, C. Straßer, K. Kern, and C. R. Ast, "Surface band structure of $Bi_{1-x}Sb_x(111)$", Phys. Rev. B **91**, 161406 (2015).

[84]T. Sato, K. Yamada, T. Kosaka, S. Souma, K. Yamauchi, K. Sugawara, T. Oguchi, and T. Takahashi, "Unusual temperature evolution of the band structure of Bi(111) studied by angle-resolved photoemission spectroscopy and density functional theory", Phys. Rev. B **102**, 085112 (2020).

[85]C. R. Ast and I. Gierz, "*sp*-band tight-binding model for the bychkov-rashba effect in a two-dimensional electron system including nearest-neighbor contributions from an electric field", Phys. Rev. B **86**, 085105 (2012).

[86]J. Ziman, *Elements of advanced quantum theory* (Cambridge University Press, 1969).

[87]A. Abrikosov, L. Gorkov, I. Dzyaloshinski, and R. Silverman, *Methods of quantum field theory in statistical physics*, Dover Books on Physics (Dover Publications, 2012).

[88]A. Zagoskin, *Quantum theory of many-body systems: techniques and applications*, 2nd (Springer Publishing Company, Incorporated, 2014).

[89]S. Datta, *Quantum transport: atom to transistor* (Cambridge University Press, 2005).

[90]T. Hirahara, S. V. Eremeev, T. Shirasawa, Y. Okuyama, T. Kubo, R. Nakanishi, R. Akiyama, A. Takayama, T. Hajiri, S.-i. Ideta, et al., "Large-gap magnetic topological heterostructure formed by subsurface incorporation of a ferromagnetic layer", Nano letters **17**, 3493–3500 (2017).

[91]S. V. Eremeev, V. N. Men'shov, V. V. Tugushev, P. M. Echenique, and E. V. Chulkov, "Magnetic proximity effect at the three-dimensional topological insulator/magnetic insulator interface", Phys. Rev. B **88**, 144430 (2013).

[92]Y. Zhang, K. He, C.-Z. Chang, C.-L. Song, L.-L. Wang, X. Chen, J.-F. Jia, Z. Fang, X. Dai, W.-Y. Shan, et al., "Crossover of the three-dimensional topological insulator Bi_2Se_3 to the two-dimensional limit", Nature Physics **6**, 584–588 (2010).

[93]K. M. Paraskevopoulos, "Electron effective mass dependence on carrier concentration in $TlBiTe_2$ monocrystals", physica status solidi (b) **127**, K45–K50 (1985).

[94]M. Michiardi, I. Aguilera, M. Bianchi, V. E. de Carvalho, L. O. Ladeira, N. G. Teixeira, E. A. Soares, C. Friedrich, S. Blügel, and P. Hofmann, "Bulk band structure of Bi_2Te_3", Phys. Rev. B **90**, 075105 (2014).

Acknowledgements

I would like to extend my sincere gratitude to all those who have supported and encouraged me throughout the process of writing this doctoral thesis.

First and foremost, I am deeply grateful to my advisor, Professor Yuki Fuseya, who has been an exceptional mentor throughout my journey in writing this thesis. Your wisdom, patience, and guidance have been invaluable, and I am thankful for the time and effort you put into mentoring me. I will always remember the day you approached me with the opportunity to work on a project that eventually became my thesis. Your belief in me and my abilities was a turning point, and I am grateful for that.

I would also like to express my appreciation to Professors Naruo Sasaki, Jun Nakamura, Kazuyuki Matsubayashi, and Nobuhito Kokubo for their time and effort in evaluating this thesis.

I am grateful to the University of Electro-Communications, Department of Engineering Science, for providing me with the resources and opportunities to pursue my research.

I am deeply appreciative of the discussions and debates with my colleagues in the laboratory, and I value their insights and suggestions. I would like to thank Dr. Mitsuaki Owada, Dr. Hiroshi Hayasaka, Dr. Yuki Izaki, Dr. Akiyoshi Yamada, Mr. Shogo Kawamura, Mr. Yudai Awashima, Mr. Yuki Mitani, and Mr. Tatsuki Kikuchi for their outstanding contributions. I appreciate Dr. Yamada's wisdom, Mr. Awashima's technical support, and Mr. Kikuchi's knowledge of previous research. I am grateful for the discussions with Mr. Reo Sato, Mr. Hideki Saito, Ms. Rikako Yaguchi, and Mr. Kazuki Koie, who have deepened my understanding of my research. I also have fond memories of drinking parties and watching the World Cup with my laboratory colleagues, including Mr. Takeshi Kawasaki, Mr. Sekito Hirota, Ms. Erika Hayashi, and Mr. Shuto Tago.

Most of all, I am grateful to my friends and family who have been there for me every step of the way. I would like to thank my father, Katsumi Asaka, my mother, Mariko Asaka, and my brother, Tomomi Asaka, for their constant support throughout this journey. Their encouragement and belief in me have been a source of strength and inspiration. I am also grateful to my friends, especially Mr. Kazuya Furuichi, Mr. Hiroyuki Takewa, Mr. Masaki Chiba, and Mr. Daiki Takada, for the lighthearted conversations and laughter we shared. Also, I would like to express my thanks to Ms. Rana Takahashi. Your genuine interest in my research have been a motivation.

I want to thank each and every one of you for being a part of this journey with me.

List of publication

Academic paper:

1. Yuya Asaka, Tatsuki Kikuchi, and Yuki Fuseya

"Long-range permeation of wave function and superficial surface state due to strong quantum size effects in topological Bi/BiSb heterojunctions"

Phys. Rev. B **106**, 245303 (2022).
DOI: 10.1103/PhysRevB.106.245303